

DEXPAND PROJECT RESEARCH REPORT WITH EXPANDER DESIGN, PERFORMANCE AND FEASIBILITY MAPPING

Project partners: CTU in Prague, NTNU, SINTEF, GT Progres

Project name: Optimised expanders for small-scale distributed energy systems

Authors: Václav Novotný, Jan Špale, Philipp Streit, Andreas P. Weiss, Václav Vodička, Zbyněk Zelený, Tomáš Vampola, Jakub J. Ochec (CTU)

Lars O. Nord, Lasse B. Anderson, Benjamin Mitterrutzner (NTNU)

Luca Riboldi, Donghoi Kim, Ruben M. Montañés (SINTEF)

Čeněk Vašák (GT Progres)

Contents

Contents	ii
List of Figures.....	iv
List of Tables	ix
Introduction.....	1
1. WP1 – System modelling and simulation	2
1.1 Definition of case studies.....	2
1.2 Methodology	3
1.3 Results of process optimization.....	5
1.4 Off-design cycle model.....	8
1.5 Testing (case study) on ORC CHP data.....	8
2 WP2 - Expander modelling, design and optimisation	12
2.1 Single stage axial turbines.....	12
2.1.1 CTU model.....	12
2.1.2 NTNU model	27
2.2 Non-orthodox turbines – Elektra turbine	29
2.2.1 Initial considerations.....	29
2.2.2 ORC – Elektra design.....	31
2.3 Rotary vane expander.....	39
3 WP3 - Expander Manufacturing, Assembly, Commisioning	46
3.1 Axial MM turbine mechanical design, manufacturing and assembly	46
3.1.1 Overall concept.....	46
3.1.2 Final v1 design.....	47
3.1.3 Design details & assembly	49
3.1.4 Axial MM turbine v2	50
3.2 Axial isobutane turbine mechanical design, manufacturing and assembly.....	52
3.3 Elektra turbine mechanical design, manufacturing and assembly.....	55
3.4 RVE mechanical design, manufacturing and assembly	57
3.5 Rotordynamics and stress analyses	63
3.5.1 Axial turbine	63

T A

Č R

3.5.2	Elektra turbine	73
3.6	Manufacturing details	75
3.7	Power output.....	76
3.8	Commissioning.....	80
3.8.1	Axial MM turbine.....	80
3.8.2	Axial isobutane turbine.....	82
3.8.3	Elektra turbine	83
3.8.4	Air RVE.....	86
4	WP4 – Experimental works.....	87
4.1	Air tests with 3D printed plastic turboexpnaders.....	87
4.2	Nozzle testing air rig.....	88
4.3	Oil-free RVE tests	91
4.3.1	Performance tests	91
4.3.2	RVE vanes durability tests.....	94
4.4	MM test rigs refurbishing	95
4.5	Elektra turbine tests	98
4.5.1	Air tests.....	98
4.5.2	MM ORC Elektra tests	103
4.6	Axial MM turbine tests.....	105
4.6.1	Air axial turbine tests	105
4.6.2	MM ORC axial turbine tests.....	106
4.6.3	MM turbine data analysis tool.....	109
4.7	Expand rig and axial isobutane turbine tests	110
5	WP5 – Assessment and feasibility mapping.....	113
6	Conclusions	118
	References	119

List of Figures

Figure 1. WP1 methods overview.....	3
Figure 2. Rankine Lab tool for Rankine cycle optimization.....	4
Figure 3. Temperature-enthalpy diagram of optimized solutions of Biogas Case study 1. (a) Design 1, (b) Design 1 with recuperator, (c) Design 2, (d) Design 2 with recuperator.....	5
Figure 4. Heat exchanger parameters for optimized Biogas Case Study 1. (a) Heat duty, (b) LMTD, (c) UA.....	6
Figure 5. Net power production of the optimized case studies.....	6
Figure 6. Cycle efficiency of the optimized case studies.....	7
Figure 7. Expander power output and pressure ratio in the optimized case studies.....	7
Figure 8. Preliminary diameter and rotating speed of the expander in the optimized case studies.....	7
Figure 9. Flowchart of the optimization framework.....	8
Figure 10. Hourly variation of the heat source (flue gas mass flow rate) over a year period at the Czech Technical University (CTU) campus.....	9
Figure 11. Energy efficiency and the accumulated power output of the MM based ORC system.....	10
Figure 12. Energy efficiency and accumulated power output for the original and optimized designs based on the reference case study.....	11
Figure 13. Computational model of the element of the single stage axial impulse turbine.....	14
Figure 14. Midspan contours of Mach number in stationary frame original and optimized geometry and full rotor in Numeca Fine Turbo.....	15
Figure 15. Difference in Mach number in the single stator convergent-divergent nozzle channel – comparison SU2/Ansys Fluent.....	15
Figure 16. Difference in Mach number in the single stator convergent-divergent nozzle channel – comparison Fluent RGP/Fluent PREOS.....	17
Figure 17. Schematic of the computational procedure for 1D design of the nozzle.....	19
Figure 18. Detailed description of the MoC ORC nozzle design procedure.....	19
Figure 19. Midspan contours of Mach number in stationary frame; CFD model of linearly divergent nozzles.....	20
Figure 20. Variation of the averaged components of the velocity vector along the span of the rotor blade at the leading edge and the trailing edge.....	21
Figure 21. Midspan Mach contours in stationary frame - effect of sharpened rotor edges contra easily manufacturable design.....	23

T A Č R

Figure 22. Turbine characteristics resulting from 1D model and CFD.....	24
Figure 23. Off-design performance map of the v1 axial MM turbine based on 3D high fidelity CFD	25
Figure 24. Mass flow rate vs. total-to-total pressure ratio at different rotational speeds.....	28
Figure 25. Sectional view of the Elektra turbine (Version 1).....	29
Figure 26. Elektra design comparison: (a) Version 1, 2a and 2b; (b) Version 3.....	30
Figure 27. Maximum efficiencies over pressure ratio for the different versions.....	30
Figure 28. Elektra turbine - comparison between a milled alloy rotor-wheel and a 3d printed MS-1 rotor-wheel.....	31
Figure 29. Curax turbine 3D model of the channels, blade wheel and first CFD investigations.....	31
Figure 30. Velocity triangles of the velocity compounded radial four-fold re-entry MM turbine (absolute velocity c, relative velocity w, circumferential velocity u, partial admission ϵ)	33
Figure 31. Turbine with the flow direction shown with white arrows and wheel passes (WP) with red arrows.....	34
Figure 32. Absolute Mach number plot of the Elektra turbine (V1).....	35
Figure 33. Absolute Mach number plot of the Elektra turbine (V2).....	36
Figure 34. Static pressure plot of the Elektra turbine (V4).....	37
Figure 35. Absolute Mach number plot of the Elektra turbine (V4 top) (V4_4_5 bottom).....	38
Figure 36. Isentropic efficiency of different Versions of the Elektra turbine.....	39
Figure 37. Off design modelled and measured characteristics of an MM RVE.....	40
Figure 38. Representations of the components of the RVE design model, from top right 1D overall model, dynamic vane model, flow path representation to the vane slot and model of the fluid flow between the chamber and vane slot.....	41
Figure 39. vane tip force and bending stress of the designed isobutane RVE.....	41
Figure 40. Sensitivity analysis of axial clearance on RVE performance.....	42
Figure 41. Sensitivity analysis of condensing pressure and temperature on RVE performance.....	43
Figure 42. Sensitivity analysis of L/D and inbuilt volumetric ratio of RVE performance.....	44
Figure 43. Preliminary mechanical design of the turbine assembly with magnetic coupling.....	46
Figure 44. Final mechanical design of the turbine assembly – detail.....	48
Figure 45. Final mechanical design of the turbine assembly with magnetic coupling and generator....	48
Figure 46. Axial high-speed turbine assembly – schematics of the detail of the shaft assembly v1.....	49
Figure 47. Final mechanical design of the turbine assembly with magnetic coupling and generator v1.	49

T A Č R

Figure 48. Cross-sectional view to the second version of the MM axial turbine assembly	51
Figure 49. CAD drawing of the casing of the ORC turbine.....	52
Figure 50. CAD drawings of the stator and rotor of the turbine. Left, the stator blades of the turbine. Right, the rotor blades.....	52
Figure 51. Manufactured and mounted rotor blades (impeller wheel).....	53
Figure 52. Photo of turbine mounted on the main skid.	53
Figure 53. Isobutane turbine interfaces.....	54
Figure 54. Meridional- (left) and blade to blade cut (right) of the Elektra Turbine.....	55
Figure 55. Assembly for air tests of the Elektra turbine.	56
Figure 56. Photos from the assembly of the Elektra turbine.	57
Figure 57. Assembly of upscaled RVE for 200 kWth system.....	58
Figure 58. p-V Diagram of a Rotary Vane Expander Cycle.....	60
Figure 59. Vane Reaction Force vs. Angular Displacement for a Rotary Vane Expander.....	61
Figure 60. Annotated Cross-Section of a Rotary Vane Expander Assembly.	62
Figure 61. Air RVE assembly before parts assembled together.....	62
Figure 62. Air RVE assembly after completion.	63
Figure 63. Two preliminarily investigated turbine shaft configurations, direct connection (left) and with magnetic coupling between working fluid region and generator (right).....	64
Figure 64. Two preliminarily investigated turbine shaft configurations, the finite elements models, direct connection (left) and with magnetic coupling between working fluid region and generator (right).	64
Figure 65. Geometric configuration of the system.	65
Figure 66. Bearing stiffness characteristics.	66
Figure 67. Circular oscillations.....	67
Figure 68. First natural frequency values for circular (blue) and bending (red) oscillations.....	69
Figure 69. Campbell diagram of the axial turbine, identifying the potentially critical speed for resonance operation, v1 MM turbine.....	71
Figure 70. Comparison of the basic dimensions for the v1 and v2 shaft assembly (CoG = centre of gravity).	72
Figure 71. Rotors of the axial MM turbine after dynamic balancing.....	72
Figure 72. Displacement and stresses for the Elektra turbine at 3000 rpm and 200 °C.	73
Figure 73. Modal analysis of the Elektra turbine.	74

T A Č R

Figure 74. Example of 3D printed models of the flow components.....	75
Figure 75. Manufactured components of the axial turbine.....	75
Figure 76. Manufactured components of the Elektra turbine.....	76
Figure 77. Electrical configuration with VFD and AFE.....	77
Figure 78. Schematic representation of a 2k+r planetary gearbox.....	77
Figure 79. Schematic representation of a Garrard friction gear.....	78
Figure 80. Electronic conceptual circuit diagram of the electrical connection with commercial PV (battery enabled) inverter and directly with PV inverter.....	79
Figure 81. Electronic conceptual circuit diagram of the individual electronic units in the micro turboexpander power measurement system.....	79
Figure 82. Experimental set-up in PDLT OTH Amberg-Weiden of the axial MM turbine to test the isentropic efficiency of the machine on various different pressure ratios and rotational speed with compressed air.....	80
Figure 83. Commissioning issues of the v1 assembly with vibrations resonating the shaft assembly causing extreme shaft runout and collision of the magnetic coupling rotor with a sealing cylinder	81
Figure 84. A close-up image of the axial supersonic turbine assembly mounted to the 50 kWth ORC test facility.....	82
Figure 85. Expander test facility at NTNU, Varmeteknisk lab with NTNU PhD candidate. The isobutane turbine is circled in red.....	83
Figure 86. Damaged compressor shaft and related compressor wheel.....	83
Figure 87. Elektra turbine in operation in the CTU UCEEB 120 kWth ORC test rig.....	84
Figure 88. Elektra turbine – comparison of the CFD flow separation and oil marks that indicate a good match in the simulation; + damage of the deflection channel wall by O-ring expansion.....	85
Figure 89. Part of the Czech-German-Norwegian project team after successful measurements of the Elektra turbine at CTU UCEEB.....	85
Figure 90. Experimental set-up of the RVE to test the isentropic efficiency of the machine on various different pressure ratios and rotational speed with compressed air.....	86
Figure 91. (left) Comparison of FDM and SLS (long chord) stator wheels and the effect of 3-D printing methods on the isentropic efficiency; both with SLS rotor; measured at three different PRs; (right) Effect of the partial admission on the ventilation loss correlation and turbine performance; both stator and rotor - selective laser sintered (SLS, long chord stator).....	87
Figure 92. Visualisation of the air rig to test additive manufactured nozzle elements and effects of postprocessing, respectively of the surface roughness.....	88
Figure 93. Air rig for measurements of additively manufactured turbine nozzle segments.....	88

T A Č R

Figure 94. 3D printed nozzle (ASA material) segment surface roughness measured using 3D optical measurement device.....	90
Figure 95. Correlated efficiency of the 3D printed nozzles to the measured surface roughness Ra.....	91
Figure 96. Schematic Diagram of a Rotary Vane Expander Test rig facility.....	92
Figure 97. Experimental performance characteristics of the RVE at varying pressure.....	93
Figure 98. Experimental performance characteristics of the RVE at nominal pressure.....	94
Figure 99. Experimental stand for long term vane durability testing.....	95
Figure 100. MM testrig after the incident and during refurbishments.....	96
Figure 101. New concept of the MM testrig heat exchangers.....	96
Figure 102. Wear of the RVE after long-term trials, wear of the rotation faces (left), of the vanes from original width 24 mm (right) and stator (bottom).....	98
Figure 103. A custom built test rig to measure mechanical design and expansion efficiency of the velocity compounded Elektra turbine.....	99
Figure 104. Mass flow rate of the pressurized air as a function of turbine inlet pressure based on 1DTDT, 3D CFD and measurements (choked flow condition in the nozzles).....	100
Figure 105. Experimentally determined total-to-static isentropic efficiency of the turbine as a function of rotational speed and turbine inlet pressure (outlet pressure kept constant at 1 bar).....	100
Figure 106. Comparison of the performance map of the Elektra turbine from CFD calculations and measurements for 6 bar inlet pressure and air as working fluid.....	101
Figure 107. Comparison of the streamwise static pressure distribution over the Elektra turbine from CFD calculations and measurements for 6 bar inlet pressure (WP = wheel pass).....	102
Figure 108. Experimental setup – biomass-fired 120 kWth CHP ORC unit equipped with ELEKTRA turbine.....	103
Figure 109. Results (Power Output) of the preliminary measurements of the functional sample of the Elektra turbine in the MM ORC test rig.....	104
Figure 110. Results of the preliminary measurements of the functional sample of the Elektra turbine in the MM ORC test rig compared to the compressed air operation measurements.....	104
Figure 111. Isentropic efficiency as a function of rotational speed for various pressure ratios measured with compressed air.....	105
Figure 112. Schematics of the placement of the supersonic axial turbine within the ORC cycle.....	106
Figure 113. A distance view onto the 50 kWth ORC test rig fitted with the axial supersonic turbine.....	107
Figure 114 Isentropic efficiency as a function of rpm for the v1 MM Axial turbine - experimental data from the CTU MM test rig.....	108

Figure 115 Experimental results of the MM Axial impulse turbine measured at CTU ORC test rig, second version assembly	108
Figure 116. An illustrative example of an automatically evaluated experimental dataset for the MM turbine, power and efficiency at different rotational speeds and turbine inlet pressures.....	110
Figure 117. Simplified P&ID of the EXPAND test rig. Maximum temperatures, pressures and mass flow rates are indicated in the plot. In red, the values with activated recuperator or re-compression mode. Valves are labelled, and transmitters are indicated. The turbine is labelled TB1.....	111
Figure 118. Results from one of the test runs. To the left, the turbine power output as a function of turbine inlet pressure and turbine inlet temperature. To the right, the resulting isentropic efficiency.	111
Figure 119. Energy efficiency and accumulated power output for the original and optimized designs based on the reference case study.	113
Figure 120. Efficiency mapping for considered expander types (assuming impulse turbines).....	114
Figure 121. Expander mapping regarding speed for considered expander types.	115
Figure 122. Performance maps of the experimentally explored expanders regarding the PR, power output and efficiency.	115
Figure 123. Performance maps of the experimentally explored expanders regarding the PR, nominal speed and efficiency.....	116
Figure 124. Parameter map of the experimentally explored expanders regarding the PR and rotor (or stator bore for RVE diameter).	116
Figure 125. Performance maps of the experimentally explored expanders regarding the PR, nominal speed and efficiency.....	117

List of Tables

Table 1. Overview of explored cases.....	4
Table 2. Main expander results from system modelling, design optimization for Case Study 1.....	6
Table 3. Output results of expander design based on the reference case study.	10
Table 4. Chosen input parameters and guesses; parameters denoted with * were later optimized – optimized values in brackets.....	13
Table 5. Comparison SU2/Fluent – nozzle throat and outlet.....	16
Table 6. Comparison PR EOS / RGP – nozzle throat and outlet.	17
Table 7. Comparison of 1D model, CFD with linear nozzles and CFD with MOC nozzles.....	22
Table 8. Optimized parameters of the designed axial turbine based on the CFD optimization.	24

T A Č R

Table 9. Comparison of parameters of the v1 and the v2 MM axial supersonic turbines.....	27
Table 10. The boundary design conditions for the Elektra turbine.....	32
Table 11. Isobutane RVE design parameters.....	41
Table 12. Summary of the previous and newly designed RVE parameters under nominal conditions..	42
Table 13. Technical specifications of the isobutane turbine	53
Table 14. Parameters of the RVE for the 200 kWth unit.....	58
Table 15. Boundary conditions for the oilless rotary vane expander final design	59
Table 16. Natural frequency of the system ain bending oscillations.....	66
Table 17. Natural frequency of the circular oscillations – intangible shaft.....	67
Table 18. Natural frequency of the circular oscillations – tangible shaft, bearing stiffness.....	67
Table 19. Natural frequency of the system according to Figure 68.....	68
Table 20. Deformation values of the unbalanced system.....	70
Table 21. Summary of 3D printed nozzle segment measurement – effect of surface roughness on resulting isentropic efficiency of the expansion; columns (CZ) left to right: additive manufacturing method, material, average thrust of the nozzle [N], average thrust of the nozzle [kg], air exit velocity [m/s], nozzle isentropic efficiency [%].....	89
Table 22. Comparison of the boundary conditions of the design point and the off design/medium CFD/Measurements of the Elektra Turbine.....	101

T A
Č R

Page intentionally left blank

Introduction

Efficient, reliable and cost-effective expanders are the key enabling components for many distributed energy systems, such as organic Rankine cycles (ORC) and other thermodynamic cycles for waste heat recovery (WHR), biomass-fired power generation, or low-temperature geothermal resources based on deep energy wells. ORCs are the unrivalled technical solution for generating electricity from low to medium temperature heat sources of limited capacity; therefore, this project aims specifically at the development of expansion machines for these technologies. Current expanders for small systems (1–50 kW electrical power output) are either not in the market, are too expensive, or don't provide satisfactory performance and most of the possible energy sources are not utilised. Cost-effective expanders could enable a significant market for this type of distributed energy systems and offer a large potential for overall CO₂ savings. This project focuses on the development and testing of cost-effective expanders for power generation in distributed energy systems, reporting expanders' data and mapping of the technologies over the power range 1–50 kW based on cost, application feasibility, and performance.

The report is further divided to chapters according to the work packages. The report is complemented by the data with models, resulting parameters, manufacturing documentation or experimental performance in the repository <https://github.com/janspale/DEXPAND>.

1. WP1 – System modelling and simulation

The DExpand project WP1 includes a methodology to translate process performances into expander design parameters through system modelling, simulation and optimization. The main objective of the first phase in WP1 is to design three different heat-to-power conversion cycles by means of system modelling, simulation and optimization. The optimization results and expander design analysis indicate the dimension and rotating speed of the turbomachinery is within the typical design range of such small gas expanders. Thus, the results from Phase 1 part of WP1 give input parameters to WP2 that could be used as first estimate boundary and operating conditions for detail expander design in other work packages.

The work included the following:

- Definition of case studies
- Definition of performance targets and KPIs
- Modelling and optimization of processes
- Results: Inputs available for expander design (WP2)

1.1 *Definition of case studies*

The work includes defining case studies and in detail specific boundary conditions and their operating range, for three different applications with expander power output in the range of 1–50 kW. The three case studies are based on:

- Case Study 1: Small scale ORCs for waste heat recovery from biogas internal combustion engine (ICE) for distributed Energy Systems
- Case Study 2: Low temperature geothermal ORC systems using deep energy wells
- Case Study 3: Micro-CHP biomass

Several case studies were proposed early in the project for further evaluation in DExpand as waste heat case, including industrial waste heat (aluminium production), ship engine jacket water and biogas combustion engine flue gas. There are efforts being held in several EU countries to develop micro scale biogas plants using farm biomass resources for energy production. Internal combustion engines ICEs can make use of generated biogas as fuel for heat and power production in ICEs. Small scale ORC can be installed to recover waste heat from flue gas of ICE and possible cooling water (jacket cooling water) to produce extra heat and power. Considering the impact and the number of existing and possible future installations, this application was chosen for the WHR ORC case study.

The heat demand will be however seasonally dependent, suggesting different utilization methods of the waste heat sources (flue gas and jacket water). In this work, the heat demand is assumed to be covered by the jacket water while the flue gas is used to produce electricity through an ORC system.

Geothermal energy is one of the promising renewable technologies of power generation. Due to the low heat source temperatures this energy provides, the use of Organic Rankine Cycles is a possibility to guarantee a good performance of the system. The working fluid iso-butane has been pre-selected in previous work, as it will be the one tested in the Expand rig.

Regarding the biomass micro-CHP system, the number of systems utilizing solid and lower quality fuels is very low, even though the supply of those fuels can be significant, reliable and their price may be low. Only a few units and projects for μCHP systems operating with solid fuels (biomass) and having power output < 30 kWe have been conducted in the world. The working fluid MM (hexamethyl disiloxane) has been pre-selected and the conditions simulated correspond to the CTU MM rig.

1.2 Methodology

Three case studies are defined for small scale heat-to-power ORC system design and optimization. The cases will define the boundary conditions for optimization, together with possible cycle configurations, inequality constraints and independent variables for the optimization. The general method is described in Figure 1.

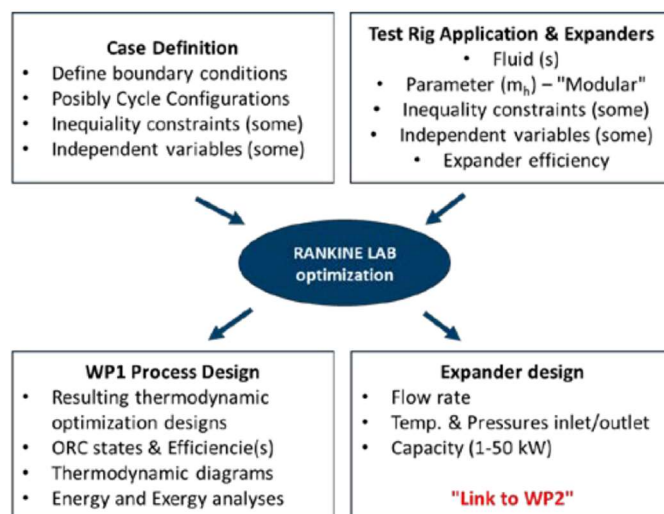


Figure 1. WP1 methods overview.

Following aspects were considered with main specifics summarized in Table 1:

- Process configuration: Simple process configurations preferred for small-scale distributed applications (techno-economic limitations). Simple and recuperated cycle are considered.
- Working fluids: For Case 2 and 3 the working fluids are predefined by the design and rig constraints. Case 1 will also use the same working fluid as Case 3 since they have similar operating conditions.
- Rigs: The rigs from NTNU and CTU define some boundary conditions.
- Expanders: The expanders are relevant as they will define a preliminary efficiency value to be set in optimizations.
- Thermodynamic boundary conditions: They depend on the case study. Two sets of constraints are considered – according to specific rig (variables that must be constrained to suit the test rigs specific characteristics, i.e., more limited) and “practical constraints” given by the utilization of state-of-the-art equipment, expected to be less stringent than the rig constraints.

Table 1. Overview of explored cases.

Case	Case 1: Biogas ICE WHR	Case 2: Low temperature geothermal	Case 3: Biomass micro-CHP
Process Configuration	Simple cycle with or without recuperator	Simple cycle with or without recuperator	Simple cycle with or without recuperator
Working fluid	MM	Isobutane	MM
Test Rig	assumed as CTU	Expand	CTU
Objective KPI	Net power output	Net power output	Net power output
Design basis	Design 1. Test rig constraints Design 2. Practical constraints	Design 1. Test rig constraints Design 2. Practical constraints	Design 1. Test rig constraints Design 2. Practical constraints
Expander type/efficiency	Design expander: Relevant to test rig (CTU)	Design expander: Relevant to test rig	Design expander: Relevant to test rig

The open source Rankine Lab¹ tool has been used as model basis for optimization (see Figure 2 for an illustration of the process flowsheet and of the optimization workflow). It is a MATLAB tool that can be used to analyse and optimize Rankine cycles. It utilizes a gradient based optimizer (SQP), and several cycle configurations are possible to analyse. In addition, several working fluids can be chosen, being linked to RefProp and CoolProp. For the optimization of the ORC systems, 7 decision variables and 9 inequality constraints are defined.

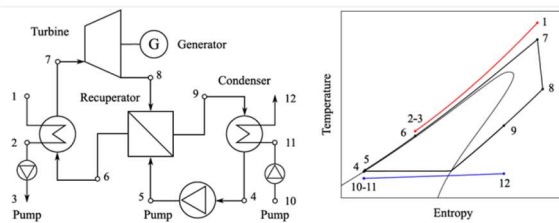


Figure 1: Process flowsheet (left) and T-s diagram of a recuperated Rankine cycle.

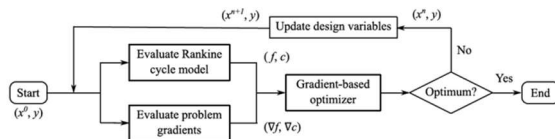


Figure 2. Rankine Lab tool for Rankine cycle optimization.

The objective function selected to identify the optimal solution was the net power output. This was deemed as the most appropriate metric for this kind of distributed application where effectiveness needs to be conjugated with ease of implementation and compactness. Other KPIs presented in results section are defined as plant efficiency, cycle efficiency, plant exergy efficiency, cycle exergy efficiency.

¹ For the open code and technical documentation, refer to <https://github.com/RoberAgro/RankineLab>

Optimizations were performed both for a cycle with and without recuperator, resulting in 12 cases (3 applications, with or w/o recuperator and rig or practical limits of design constraints).

In order to give preliminary indications of expander design, the speed and the diameter of the turbomachinery are also estimated by considering the specific speed (ω_s) and the specific diameter (d_s) [1].

1.3 Results of process optimization

Below is presented an example of the selected results of the biogas case (see Figure 3 to Figure 4 and Table 2) and then selected overall results summarizing all explored cases (see Figure 5 to Figure 8). The complete set of results available in the separate memo includes optimal values of design variables, values for the KPIs selected, generic turbo-expander preliminary results (input data to WP2), comparative analyses of the results and diagrams of the optimized cycles.

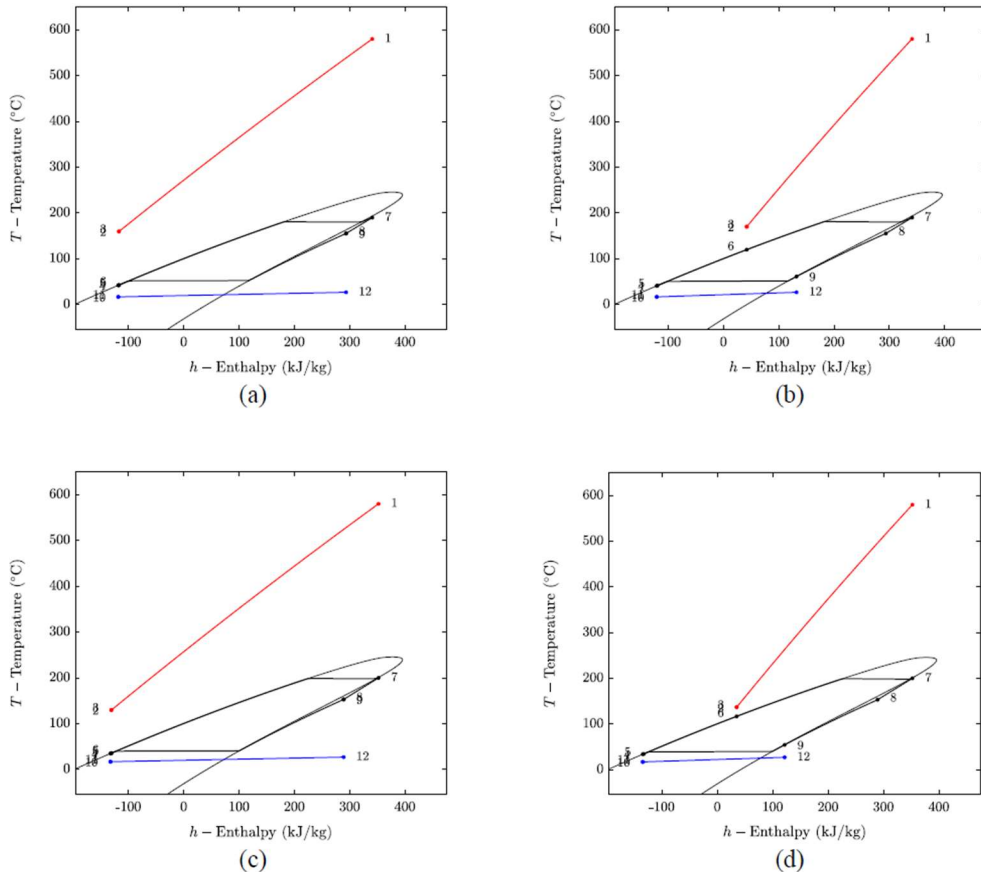


Figure 3. Temperature-enthalpy diagram of optimized solutions of Biogas Case study 1. (a) Design 1, (b) Design 1 with recuperator, (c) Design 2, (d) Design 2 with recuperator.

Table 2. Main expander results from system modelling, design optimization for Case Study 1.

	Design 1	Design 1 Rec.	Design 2	Design 2 Rec
W_{gross} [kW]	14,58	21,81	19,64	29,45
Ratio p_{in}/p_{out}	32,1	32,1	74,1	74,1
p_{in} [bar]	6,4	6,4	8,9	8,9
p_{out} [bar]	0,2	0,2	0,12	0,12
Mass flow rate m_{in} [kg/s]	0,3080	0,4609	0,3117	0,4673
Diameter [m]	0,1387	0,1696	0,1704	0,2086
Rotational speed [rpm]	37163	30379	33639	27471

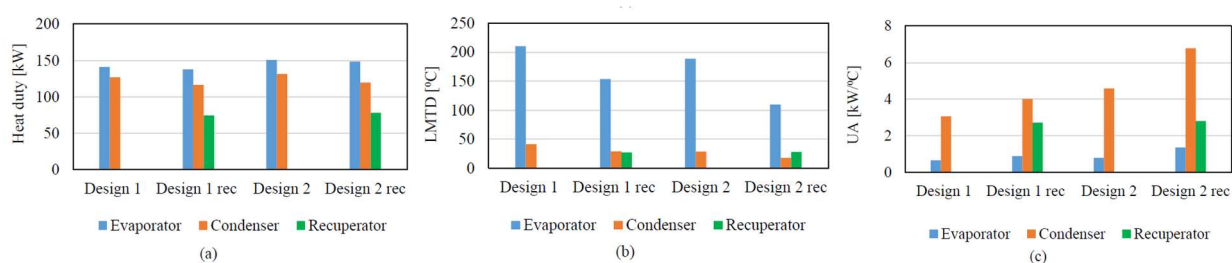


Figure 4. Heat exchanger parameters for optimized Biogas Case Study 1. (a) Heat duty, (b) LMTD, (c) UA.

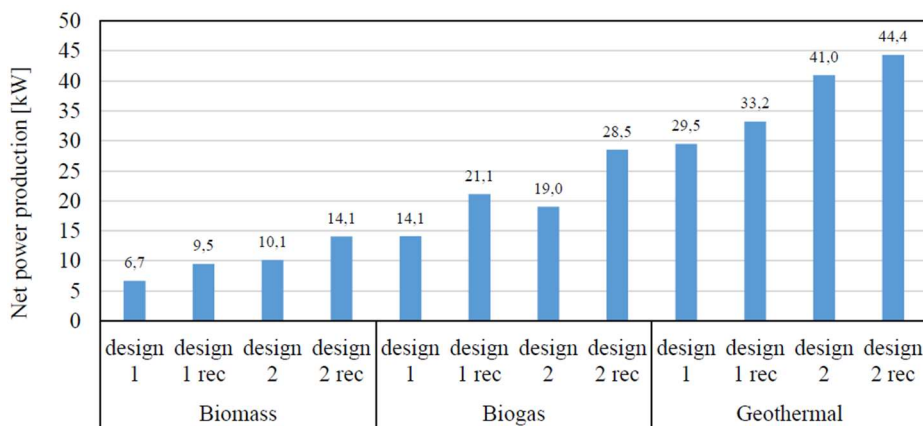


Figure 5. Net power production of the optimized case studies.

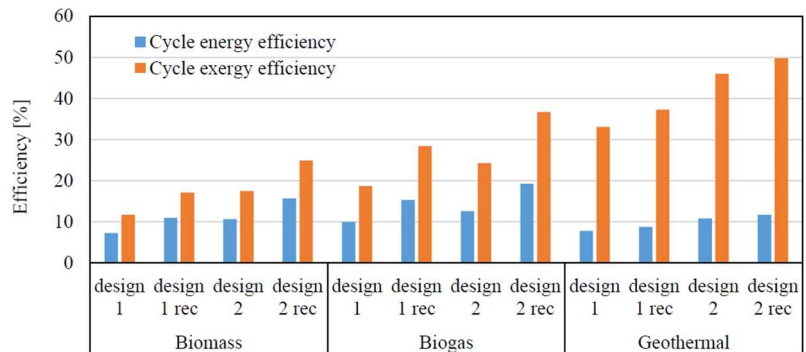


Figure 6. Cycle efficiency of the optimized case studies.

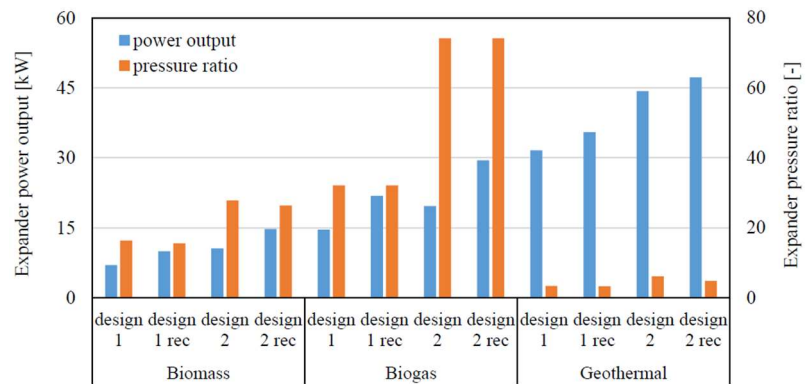


Figure 7. Expander power output and pressure ratio in the optimized case studies.

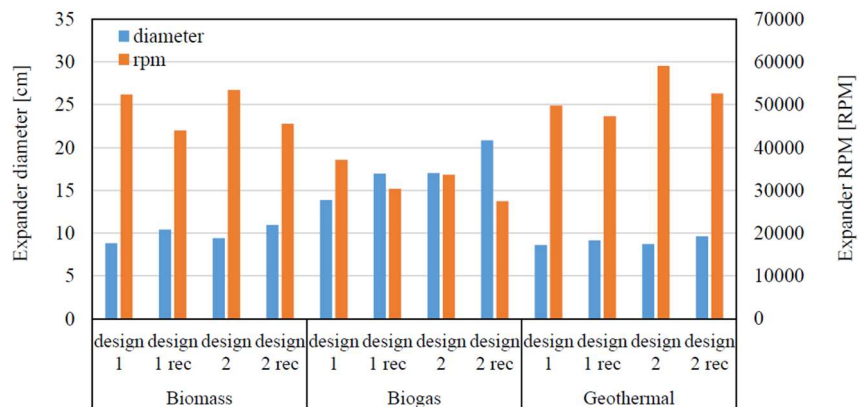


Figure 8. Preliminary diameter and rotating speed of the expander in the optimized case studies.

1.4 Off-design cycle model

In a second phase, a more thorough analysis is conducted in order to explore further the potential application and flexible operation of the resulting process from the case study applications by means of steady-state off-design modelling and simulation. The biomass case was selected not only to obtain new valuable modelling results but also for the possibility to directly test the predictions at the CTU rig, which can be operated to provide heat on demand of the building. A framework that consists of multi-scale optimization for the design of small-scale ORC systems considering seasonal and hourly heat source variations has been developed. The framework is developed as a flexible tool allowing to include fit-for-purpose models of key elements of the cycle, such as expander and heat exchanger, to suitably simulate off-design performance.

The off-design model was based on an in-house model, which was adapted to simulate an ORC system. The off-design performances of key elements of the ORC are described by models and correlations widely used in the literature.

The approach used for design optimization is depicted in Figure 9. A design is defined in terms of a set of selected independent variables. The simulation at such design point provides the process thermodynamic values of the cycle at design – in terms of mass flow rates, temperature and pressure levels and also sizes of the heat exchangers. That information is used for the off-design simulations that will be carried out for each operating conditions deemed relevant to describe the operation of the ORC. Each simulation returns the value of the objective function at the specific conditions. The overall objective function is the weighed sum of the specific values obtained from the off-design simulations.

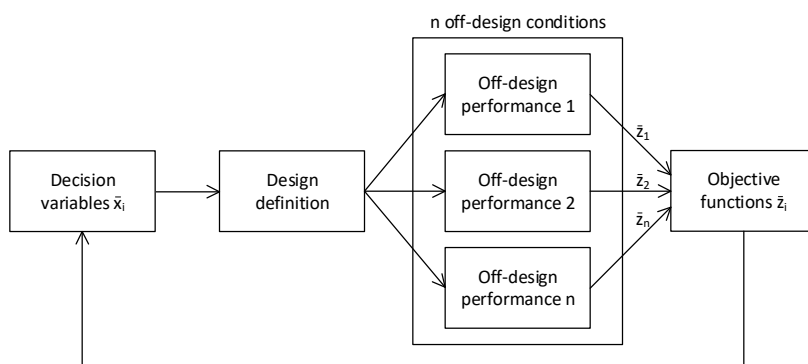


Figure 9. Flowchart of the optimization framework.

1.5 Testing (case study) on ORC CHP data

The developed methodology was tested against a reference case study: a biomass fired micro-cogeneration of heat and power considering ORC for WHR. The case study is representative of an existing unit operating at the Czech Technical University (CTU) in Prague for supplying heat (design 120 kWth) and electricity (design 6.2 kWel) to the university research center. The working fluid is MM (hexamethyldisiloxane), while the expander is a rotary vane expander. The unit is woodchips-fired. Actual operating data has been provided and used as the basis for the analysis. Figure 10 shows the variation of flue gas flow rate (i.e., the heat source for the ORC) over one year.

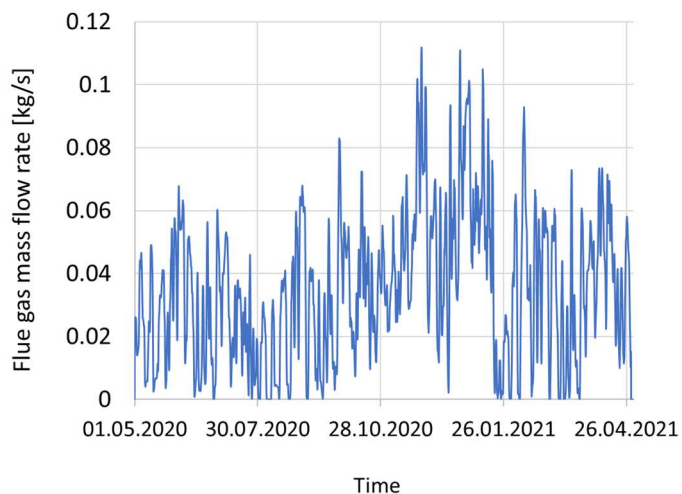


Figure 10. Hourly variation of the heat source (flue gas mass flow rate) over a year period at the Czech Technical University (CTU) campus.

Figure 11 presents the performance of two different designs of the MM based ORC system. One is the ORC system optimized for the design flue gas flow rate (referred to as design ORC). Based on the ORC design, the off-design performance is estimated to calculate the accumulated power production per year. The other is the ORC system optimized to maximize the accumulated power production throughout the year while varying the capacity (referred to as optimal ORC). The results indicate that the optimal ORC system has a 5 % larger accumulated power production throughout the year compared to the ORC system at the design. Therefore, the potential of the methodology was demonstrated.

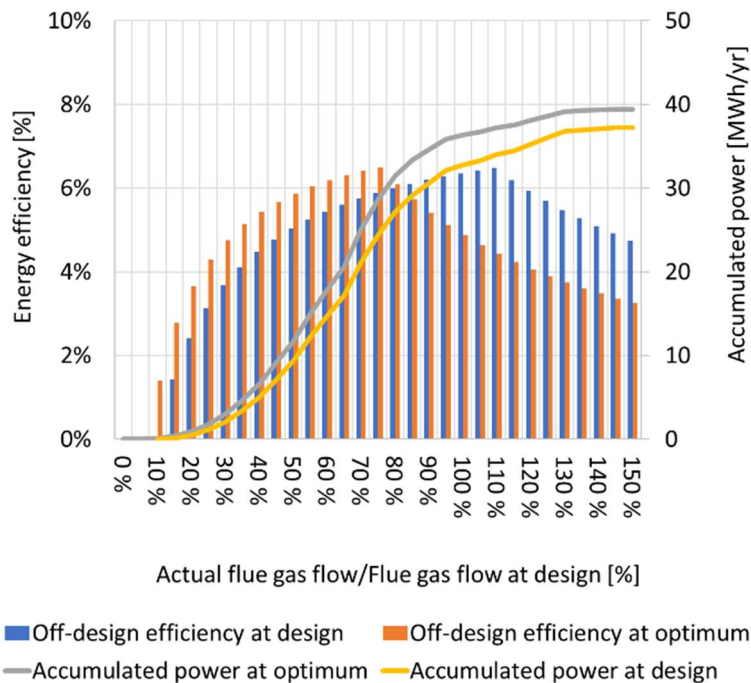


Figure 11. Energy efficiency and the accumulated power output of the MM based ORC system.

Next, a tailor-made design of the expander was obtained, which is reduced in the capacity to avoid any oversizing. Instead of the isentropic efficiency, the expander design derived from the optimization framework maximizes the power generation per unit mass of the working fluid to improve the system performance (see some output results in Table 3). Overall, the tool improved the ORC with a 10 % increase in accumulated power considering an actual heat source profile (see Figure 12).

Table 3. Output results of expander design based on the reference case study.

Parameter	Unit	Original design	Optimal design	Parameter	Unit	Original design	Optimal design
W _{accumulated}	MWh/yr	42.75	48.39	Revolutions	RPM	24353	29191
m _{flue_design}	kg/s	0.078	0.055	Diameter	cm	14.97	13.13
m _{MM}	kg/s	0.37	0.27	Flaring stator	deg	-8.6	-10.0 ¹
m _{CW}	kg/s	1.53	1.06	Flaring rotor	deg	10.0 ²	10.0 ²
W _{net}	kW	13.85	10.29	Stator exit metal angle	deg	78.1	76.6
W _{exp}	kW	14.18	10.63	Rotor exit metal angle	deg	-62.6	-55.0
n _{isentropic}	%	85.31	78.45	AR* stator	-	2.0 ²	2.0 ²
P _{r_{exp}}	-	7.78	10.89	AR* rotor	-	1.2	1.0 ¹
RPM	-	24353	29191	BS** stator	-	1.2	0.9 ¹
Diameter	m	0.15	0.13	BS** rotor	-	1.2	1.1

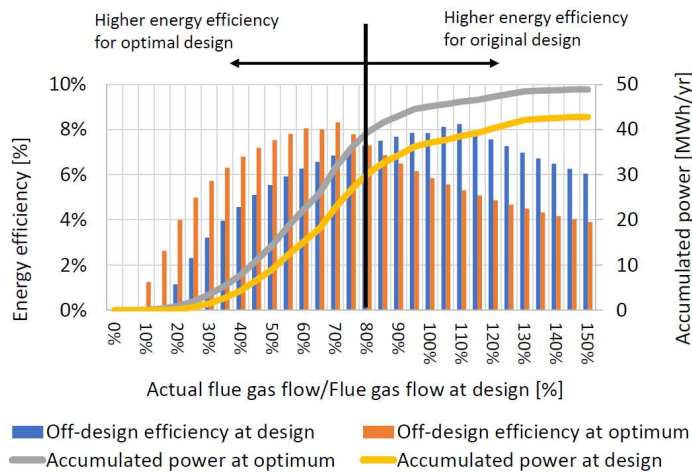


Figure 12. Energy efficiency and accumulated power output for the original and optimized designs based on the reference case study.

The WP1 finalized the multi-scale optimization tool by updating it with latest expander models. In particular, the design optimization tool was tested using the single-stage axial turbine model developed by NTNU. The model is based on a based on mean line method and incorporate an advanced loss model, critical to reflect incidence losses at off-design conditions. In additions, an off-design heat exchanger (HX) model was developed in-house to enhance the capability of the optimization tool to realistically capture off-design system performances. The HX model was developed to represent a generic counter-current HX estimating local heat transfer and pressure drop from end to end. Case studies were defined to examine ORC systems' flexibility with these expanders.

The project's findings will be documented in a journal article, with planned publication early within the sustainability phase of the project (late 2024/early 2025). Consistent with our commitment to open research, the tool will be made open source, broadening its impact in the energy field.

2 WP2 - Expander modelling, design and optimisation

Modelling and optimization includes dynamic types of the expanders applied for two different working fluids according to the test rigs at NTNU and CTU, i.e., axial single stage turbine and “non-orthodox” turbine and fluids isobutane and MM. Below are details of the performed works and results.

Modelling and optimization include dynamic types of the expanders applied for two different working fluids according to the test rigs at NTNU and CTU, and two turbine types, i.e. axial single stage turbine and a “non-orthodox” turbine. The target fluids are isobutane and MM. Volumetric RVE expander type represented by RVE model has been experimentally operated at the MM CTU rigs in the past and in this project was redesigned first for isobutane and then for a smaller air test system to primarily explore operation under “dry” (oil-free) working fluid condition. Due to the issues with the isobutane rig, the air RVE has been further tested as a substitute experiment instead of RVE for isobutane rig.

2.1 Single stage axial turbines

An axial impulse turbine is considered for the MM fluid and the CTU rig, while both impulse and reaction turbine are considered for the isobutane and NTNU rig as the pressure ratios are lower and the project covers larger range of turbine types. Note for future comparison, that the CTU model is based on velocity based loss correlation. Unlike the CTU approach, NTNU have adopted pressure loss correlations for simulation and preliminary design of primary reaction turbines. The purpose of the NTNU model is rather to develop a method for preliminary design based on a range of operating conditions rather than one design point.

2.1.1 CTU model

Design works

The boundary conditions to the turboexpander come from the test rig specifications, eventually optimization from the WP1. An axial impulse turbine is considered for the MM fluid and the CTU rig, while reaction turbine is preliminarily considered for the isobutene as the pressure ratios are lower and the project covers larger range of turbine types. The report summarizes here briefly as first the impulse MM turbine design while its details can be found in the conference paper, attached as one of the current project results.

The design pressure ratio for the turboexpander is around 12, and the inlet temperature of the superheated organic vapour is 190°C. For these inlet conditions, the speed of sound is 123 m/s, and it is quite obvious from this preliminary estimate that the fluid flow at the nozzle outlet for an isentropic enthalpy drop of around 50 kJ/kg will be highly supersonic. For ORC turbines with such high Mach numbers (above 1.4), it is necessary to design the nozzles as uniquely shaped convergent-divergent to respect the nature of the supersonic fluid flow. [2] Note that high molar mass and the molecular complexity of the organic fluid results in low volumetric flow rates and high volumetric ratios, low

enthalpy drops along the expansion line and very low speed of sound. The complex organic fluids show a very non-ideal behaviour especially in the region of the vapour single phase region. As the consequence, rather complicated real gas Equations of State (EoS) have to be utilized during the design phase. Siloxanes as members of so-called Bethe-Zel'dovich-Thompson (BZT) fluids family exhibit in the single vapour phase region a negative fundamental derivative in gas dynamics Γ - therefore all the thermodynamic properties show high sensitivity to its values and thus for precise enthalpy calculation, many experimental data and specific EoS are needed. [3]–[5] The implications of that are severe and of various character. On one hand, it helps to design very compact and little loaded machines resulting in rather cheap turbomachinery. On the other hand, low speed of sound means that the presence of a supersonic flow is inevitable, and the blade design is nonconventional with convergent-divergent nozzles. High volumetric ratios for very complex molecules lead to difficulties in processing the large difference in the volumetric flow rate in a single-stage machine which often has to be compensated by a significant change of the blade height along the streamline, partial admission and very high flow deflection angles. The variation of blade height comes with a penalty in the form of lower stage efficiency as it leads to an increased vorticity of the flow caused by the perpendicular velocity component and therefore increased secondary losses. The losses are furthermore increased by the high deflection blade shapes. High rotational speeds cannot be avoided for ORC turbines. Blade loading is usually very low due to much lower enthalpy drop and the temperature ranges in which the turboexpanders operate are also much lower compared to conventional steam turbines.

Preliminary thermodynamic and aerodynamic design of an axial impulse stage turbine for the given ORC CHP unit and boundary conditions is performed via a 1-D meanline design model. It considers a rather standard set of assumptions and is based largely on correlations [6] and [7]. For the initialization of the turboexpander design, some of the design variables had to be chosen with respect to the rotational speed, diameter of the machine and some other geometrical components. Another very important parameter to be estimated in the first step of the design is the isentropic efficiency of the turboexpander. These initial values and guesses are reported in Table 4. Some of these parameters were kept constant throughout the design phase and some were optimized, such as the rotational speed of the turbine and the blade height.

*Table 4. Chosen input parameters and guesses; parameters denoted with * were later optimized – optimized values in brackets.*

Parameter	Initial value (optimized)	Units
Rotational speed n*	24000 (28000)	rpm
Midspan diameter Dmid	100	mm
Nozzle outlet flow angle α_2	13	°
Isentropic efficiency guess	70	%
Partial admission guess e*	58.5 (97.5)	%
Blade height ratio*	0.1 (0.06)	-
Minimum blade height h_min	5	mm
Rotor blades aspect ratio AR	2	-

The stator is designed as a series of convergent-divergent de Laval nozzles. As the flow suffers sever real gas effects and is highly supersonic, the resulting nozzle geometry is very unconventional, cambered and unlike any stator blade geometries that could be found in an airfoil atlas. The rotor blades were

designed as constant channel width buckets with geometry derived from [8]. The shape of the buckets is again unconventional and highly cambered since it experiences large flow deflection.

Figure 13 shows the geometry of the computational model domain. The computational domains are connected using the Frozen rotor interface model. The rotating domain is set to a speed of 28000rpm. The SST k- ω turbulent model is used for the simulation. Since a very high Mach number is expected in the flow section of the turbine, a High-Speed Wall Heat Transfer Model is also used. The real gas properties MM are included in the CFD analysis, as it plays an important role in the quality and accuracy of the analysis. An automatic generator of RGPgen v2.0 (Real Gas Properties) for ANSYS CFX was used in this simulation. The networks of both computational domains are prepared in ANSYS ICEM with 24.4 million hexahedral cells.

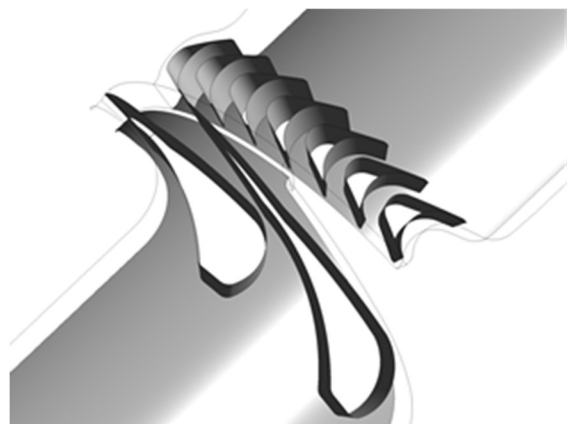


Figure 13. Computational model of the element of the single stage axial impulse turbine.

To describe the nature of the fluid flow through the turbine stage, contours of the Mach number in the stationary frame on midspan position are presented in Figure 14. Significant shockwave structures at the stator vanes trailing edge and leading edge of the rotor buckets result in secondary losses. Note the difference between the initial and optimized geometry, proving that straight divergent channels may have slightly worse efficiency, but provide robust solution, are not that sensitive to minor geometrical imprecisions and off design operation.

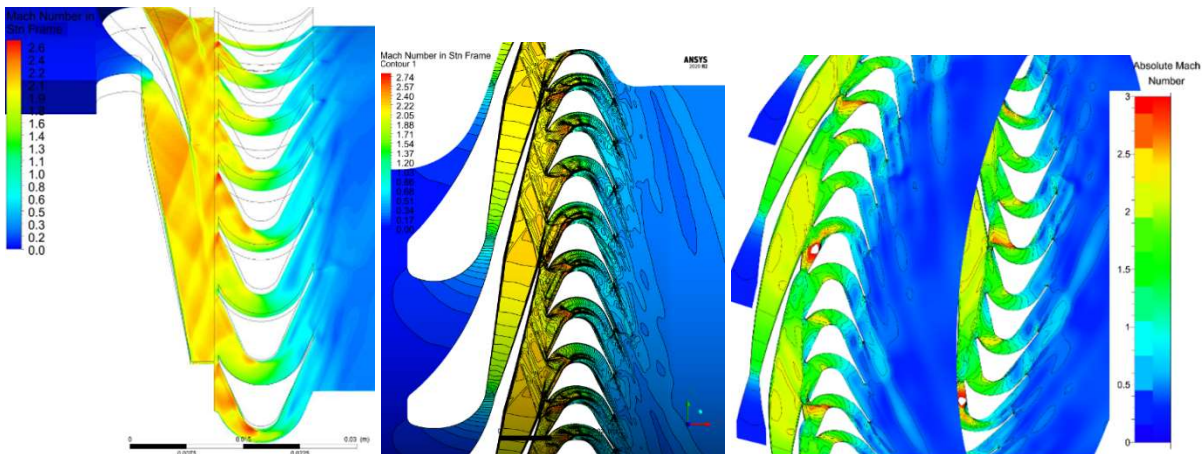


Figure 14. Midspan contours of Mach number in stationary frame original and optimized geometry and full rotor in Numeca Fine Turbo.

Additionally, there was investigated effect of the stator-rotor axial gap onto the turbine performance by the means of CFD. Also there is an ongoing comparison of different CFD SW (with the same mesh and settings) between ANSYS, SU2 and Numeca FineTurbo as well as impact of real gas fluid results from ideal or using relatively simple EoS as Peng Robinson.

The comparison analysis of various CFD software focused on the differences between an open-source SW named SU2 [9] and a commercial Ansys Fluent software for the problem of the axial single stage impulse turbine operating with MM modelled as Peng-Robinson EOS real gas was investigated. A measure to compare this two software was decided to use the Mach contours and the differences in Mach numbers. Below in Figure 15, there is plotted the difference in Mach number on the single stator convergent-divergent nozzle channel.

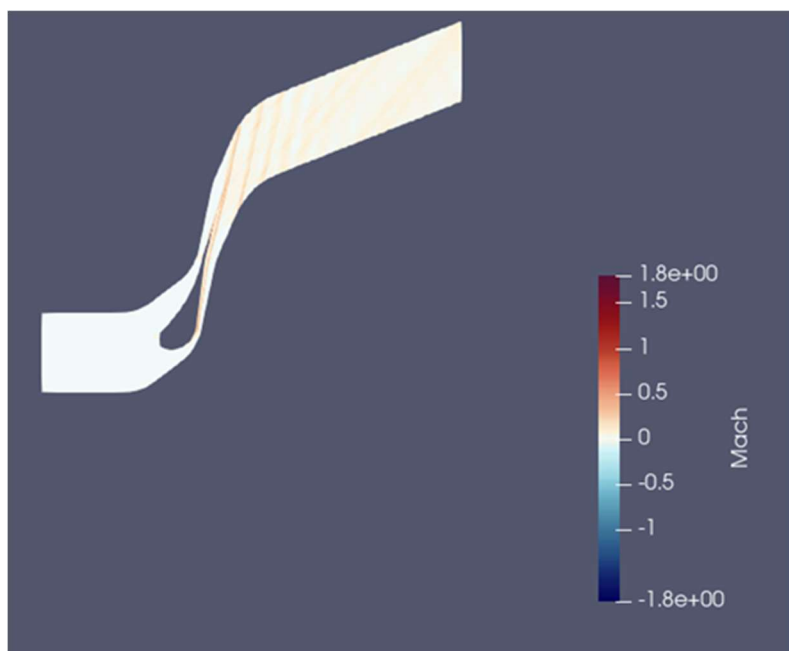


Figure 15. Difference in Mach number in the single stator convergent-divergent nozzle channel – comparison SU2/Ansys Fluent.

T A Č R

When comparing the results based on Mach numbers, Figure 15 shows that the results are not much different, with little difference occurring at the trailing edge of the blade and from the nozzle outlet onwards towards the outlet, there are noticeable differences in the region of the wake behind the blades. When evaluating the thermodynamic parameters in the throat and at the nozzle outlet, it can be seen that the results differ by a few percent (Fluent was taken as a reference). It can be seen that the results are similar in the main features: In the throat, the Mach number is approximately equal to one and both software show that although the design output Mach number is 2, there is overexpansion up to 2.175 (2.14). The difference in the throat and in the nozzle outlet is also summarized on the averaged values in Table 5.

Table 5. Comparison SU2/Fluent – nozzle throat and outlet.

	Mach [-]	Absolute pressure [Pa]
Fluent	1,038	390 563,704
SU2	1,004	385 073,220
diff	3,28%	1,41%

	Mach [-]	Absolute pressure [Pa]
Fluent	2,175	49 130,164
SU2	2,140	49 244,280
diff	1,63%	0,23%

The other comparison of the CFD simulation was between the real gas properties (RGP) and the Peng Robinson EOS (PREOS) model for real gas. The contours of the Mach number difference are plotted in the Figure 16 below.

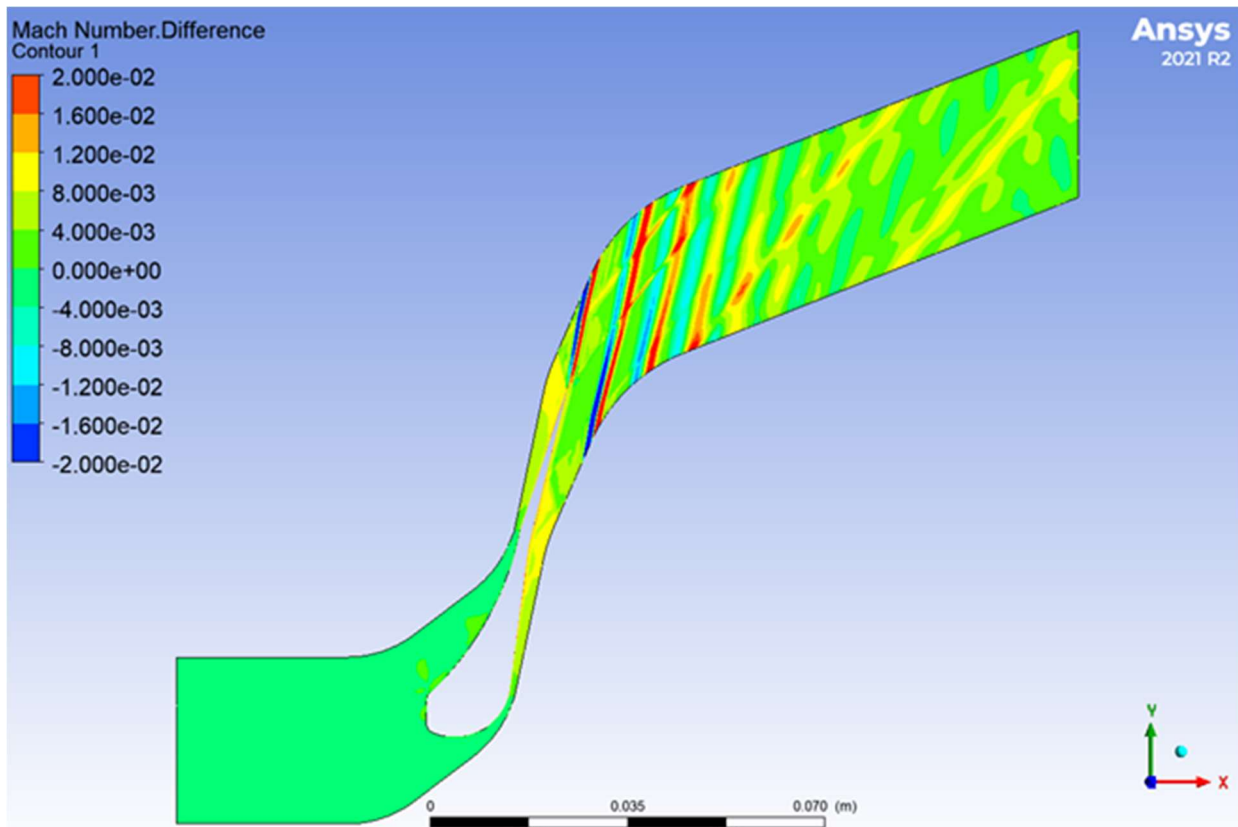


Figure 16. Difference in Mach number in the single stator convergent-divergent nozzle channel – comparison Fluent RGP/Fluent PREOS.

As we can see, the values differ mostly in the order of hundredths. Only somewhere after that there is a difference of a tenth, but this is only in a small area on the output edge of the blade. The following table again compares the thermodynamic parameters at the throat and at the nozzle outlet.

Table 6. Comparison PR EOS / RGP – nozzle throat and outlet.

	Mach [-]	Absolute pressure [Pa]
Fluent RGP	1,037	389767,265
Fluent PREOS	1,038	390563,704
DIFF	0,138%	0,204%

	Mach [-]	Absolute pressure [Pa]
Fluent RGP	2,185	48611,372
Fluent PREOS	2,175	49130,164
DIFF	0,42%	1,07%

If we focus on the question of what inaccuracy is introduced into the calculation by the use of the Peng-Robinson model for the working substance (here mm), this inaccuracy is minimal (at most in the order

of tenths of a percent). Compared to the fact that it is often difficult or at least expensive to obtain the real properties of some substances, the use of the Peng-Robinson model seems to be a suitable alternative that leads to relatively very accurate results.

Off-design model

For the CTU off-design model, loss correlations remain identical, but the velocity triangles are changing based on the off-design conditions. When the rotational speed changes, the relative velocity causes the only change and this model provides good results. When the pressure ratio changes, determination of the off-design parameters of the Laval nozzle is generally a highly complex task. Previous experimental results, however, show low sensitivity of supersonic turbine nozzles on operating pressure ratio, presumably due to a single-wall continuing behind the nozzle exit, creating a quasi flow-channel. This gives a possibility to use this off-design model also for varied pressure conditions, assuming ideal expansion between the pressure levels corrected by corresponding nozzle loss.

MOC nozzles design

For further design of supersonic nozzles was implemented a method of characteristics (MOC) design of the nozzle. MOC involves calculating a set of curves called "characteristics" that represent the flow of the gas through the nozzle. These characteristics are used to determine the shape of the nozzle that will produce the desired (optimal) flow conditions. The MOC can be used to design both convergent and divergent nozzles, and is particularly useful for supersonic flow because it can accurately predict the shock waves that are present in this type of flow.

The working fluid, fluid inlet pressure and nozzle outlet Mach number were given as input values for each simulation. The flow state at the throat yielding choked flow conditions ($Ma = 1$) were solved by searching the conditions along the expansion where the flow velocity and the speed of sound reach equal values. The nozzle outlet conditions were solved by searching the conditions along the expansion where the target Mach number was reached. The calculation of the nozzle outlet-to-throat width ratio was based on the continuity equation and on the assumption that the channel height is constant from the inlet to the outlet section. The fluid temperature, enthalpy, density, velocity, speed of sound, Mach number, compressibility factor, and the fundamental derivative of gas dynamics were solved along the expansion for each calculation node in the 2D midspan mesh of the divergent part of the nozzle. The calculation procedure is illustrated on a schematic Figure 17.

The throat width, outlet width, and outlet width to throat width ratio were calculated for each case. For each design, the nozzle length, the shape of the supersonic part of the nozzle, and the length to throat width ratio were solved by using the separate code that is based on the use of method of characteristics as formulated by Zucrow and Hoffman [10] and implemented by Guardone et al. [11] for non-ideal flows and in the open-source Python design code by Anand et al. [12]. An example of convergent-divergent nozzle is presented in Figure 18. The rotor blades for impulse stage remained designed as constant channel width buckets.

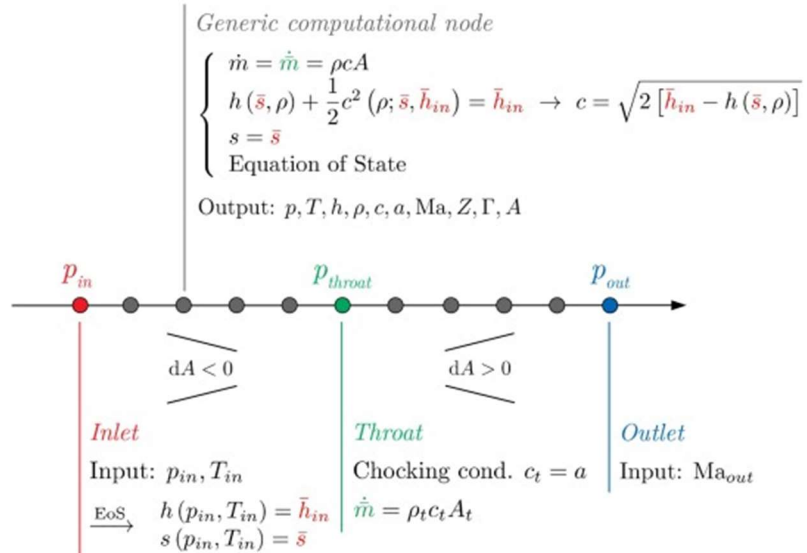


Figure 17. Schematic of the computational procedure for 1D design of the nozzle.

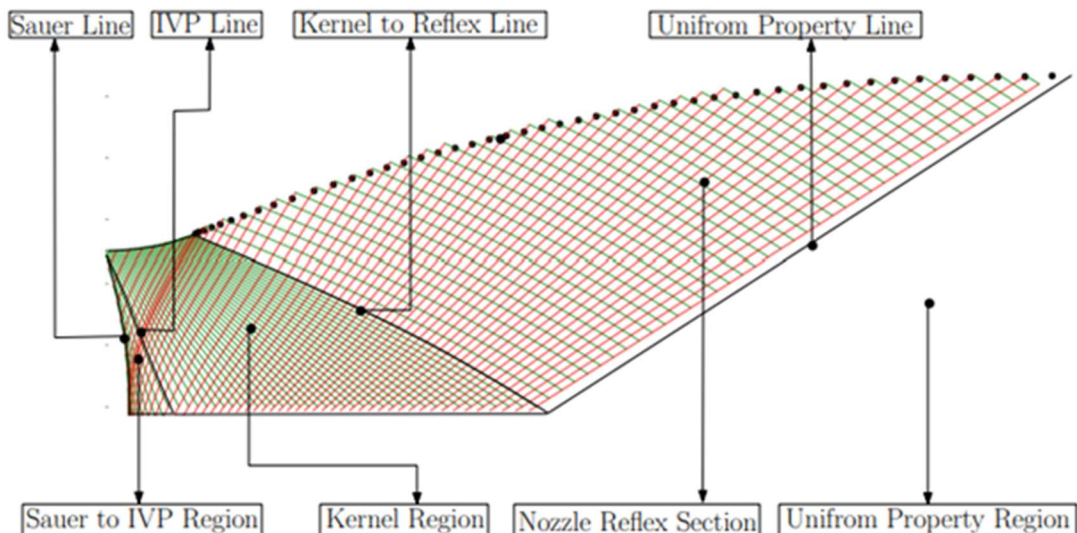


Figure 18. Detailed description of the MoC ORC nozzle design procedure.

The MOC method is however limited to planar axisymmetric application. This design for MM fluid has been therefore used in 2D CFD simulations similar to ones from previous year, but to obtain more detailed information, a full stage simulation was performed with a modelled axial gap between the stator nozzles and rotor wheel. First, the simulation was performed with stator nozzles with linearly diverging parts, next it was improved for MoC nozzles and the improvement was assessed.

To describe the nature of the fluid flow through the MM impulse turbine stage, contours of the Mach number in the stationary frame on midspan position (simulation with linearly divergent nozzles) are presented in Figure 19. Siloxane vapour at the admission pressure enters the stator nozzles, where in the convergent part of the nozzle increases its speed up to the speed of sound in the nozzle throat. Divergent part of the nozzle is designed as a linear segment increasing the nozzle area up to the designed

outlet nozzle area, achieving Mach 2 at the outlet. Significant shockwave structures at the stator vanes trailing edge are apparent. These shockwaves greatly determinate the fluid flow at the rotor inlet. There are again strong oblique shockwaves at the leading edge of the rotor buckets. These oblique shockwaves affect the fluid flow inside the channel – interaction of the shockwave with the boundary layer at the suction side of the bucket results in a flow separation, therefore secondary losses occur in the rotor wheel.

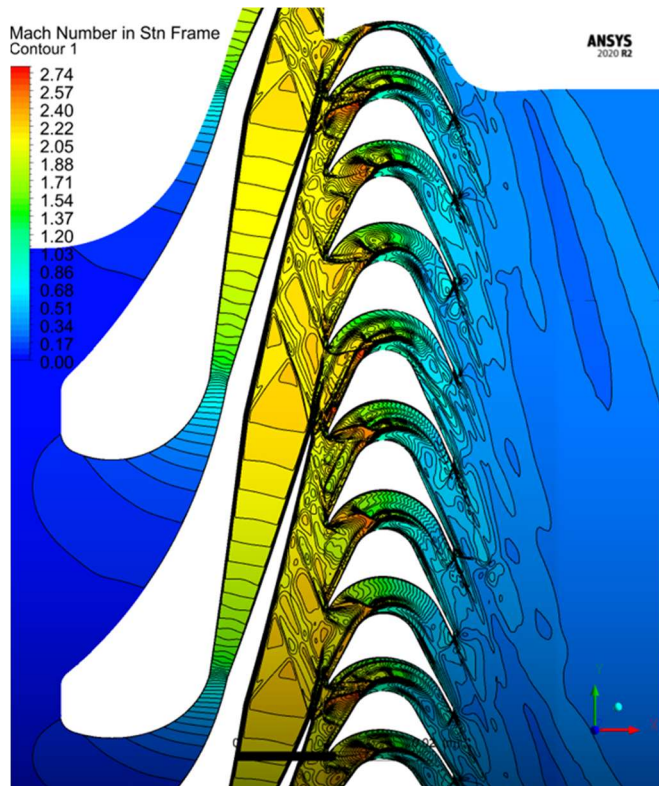


Figure 19. Midspan contours of Mach number in stationary frame; CFD model of linearly divergent nozzles.

To assess the fluid flow in the spanwise direction, components of the velocity vector along the blade span are plotted, as well as the velocity angles of the fluid flow in Figure 20 below. Thanks to the optimization of the rotor blade outlet flow angle, the effect of the flow separation at the suction side of the rotor blade was decreased, as can be observed on the rather monotonic and flat behaviour the courses of the velocity compounds exhibit along the span at the leading and especially the trailing edge.

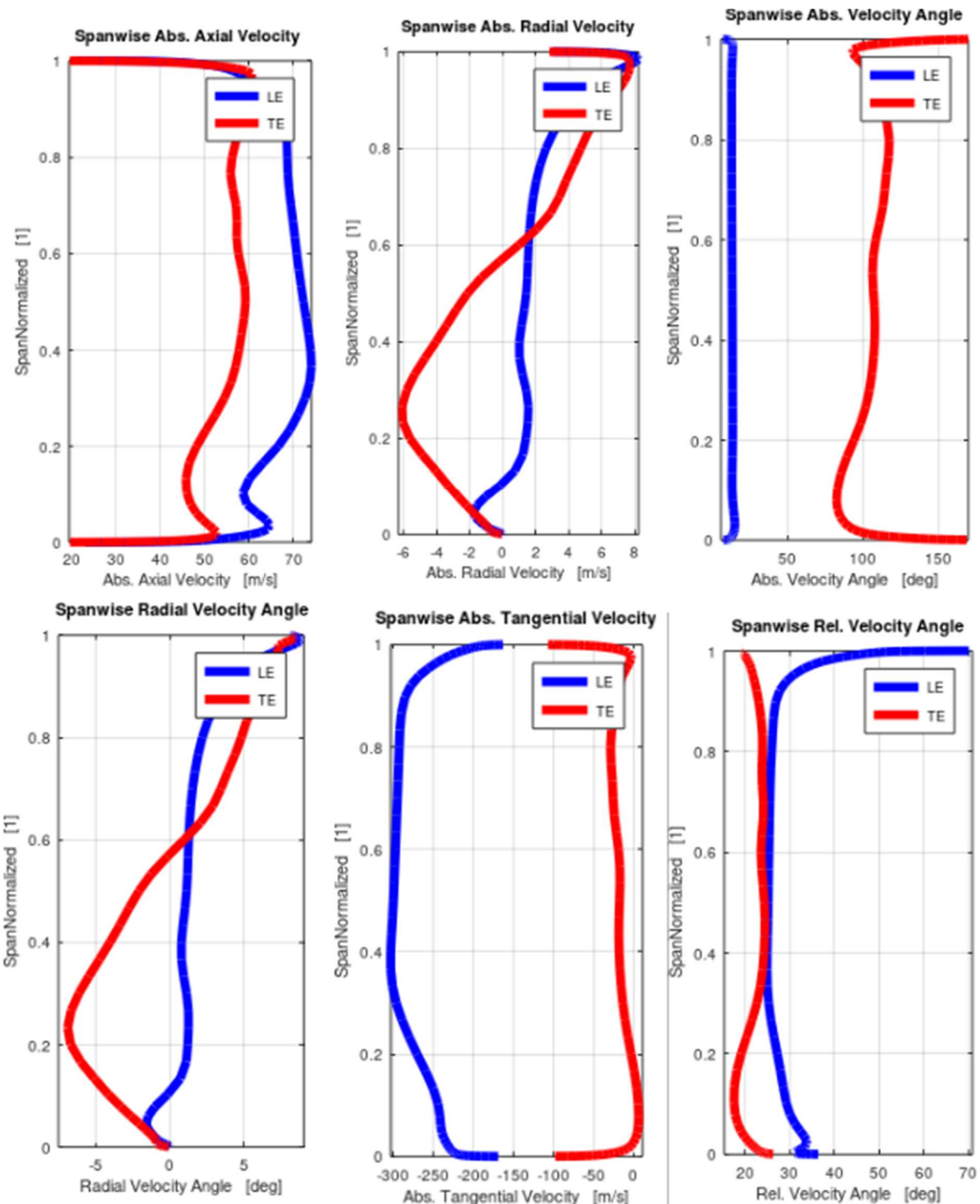


Figure 20. Variation of the averaged components of the velocity vector along the span of the rotor blade at the leading edge and the trailing edge.

The MoC nozzles stage simulation is in Figure 21 for two rotor blade options. On the left side is better manufacturable blade edge while on the right side side sharpened adges. When compared to the

T A

Č R

preliminary design with linearly divergent nozzles, it yielded a significant improvement in terms of both shockwave structures (less secondary losses) and finally isentropic efficiency. Results of the 3D CFD model with unoptimized nozzles were finally compared with the result of the optimized 1D model with loss correlations and with CFD results with optimized nozzles and with realistic trailing edge thickness of the flow components as obtained from the manufacturer. Some of the parameters are listed in Table 7 below.

Table 7. Comparison of 1D model, CFD with linear nozzles and CFD with MoC nozzles.

Parameter	1D	CFD	CFD opt	MoC	Units
Nozzle outlet/Rotor inlet					
Mach number	1.95	2.01	2.07	—	
Static pressure	55	64.3	58.7	kPa	
Static enthalpy	298.9	296.2	293.5	kJ/kg	
Rotor outlet					
Mach number	0.46	0.48	0.43	—	
Static pressure	55	54.9	54.4	kPa	
Static enthalpy	302.7	298.2	297	kJ/kg	
Isentropic efficiency nis	69.2	71.1	74.2	%	
Mechanical power output	10.8	11.2	11.5	kW	

Regarding the effect of manufacturability constraints onto the geometry and on flow structures - especially the effect of trailing edge thickness (cut-off design of stator trailing edge and rotor leading and trailing edge), following must be taken into account. 5-axis milling machines have constraints in the thickness of the edges of the blades. A challenging but reachable values of LE/TrE thickness is 0.5mm. Therefore, it was investigated in numerical analysis, whether sharpening the edges beyond the manufacturability limits would achieve any significant improvements of isentropic efficiency. The resulting flow field structures reported with Mach contours at midspan of the stage in Figure 9 conclude that despite sharpened rotor blades yield less shockwave structures in the fluid flow, still the major secondary loss source persists - a large separation bubble at the suction side of the blade. This was confirmed by the difference of isentropic efficiency of the turbine, which was only 0.5 p.p. higher for the fully sharpened blades which would be multiple times as expensive. Better manufacturability was then preferred.

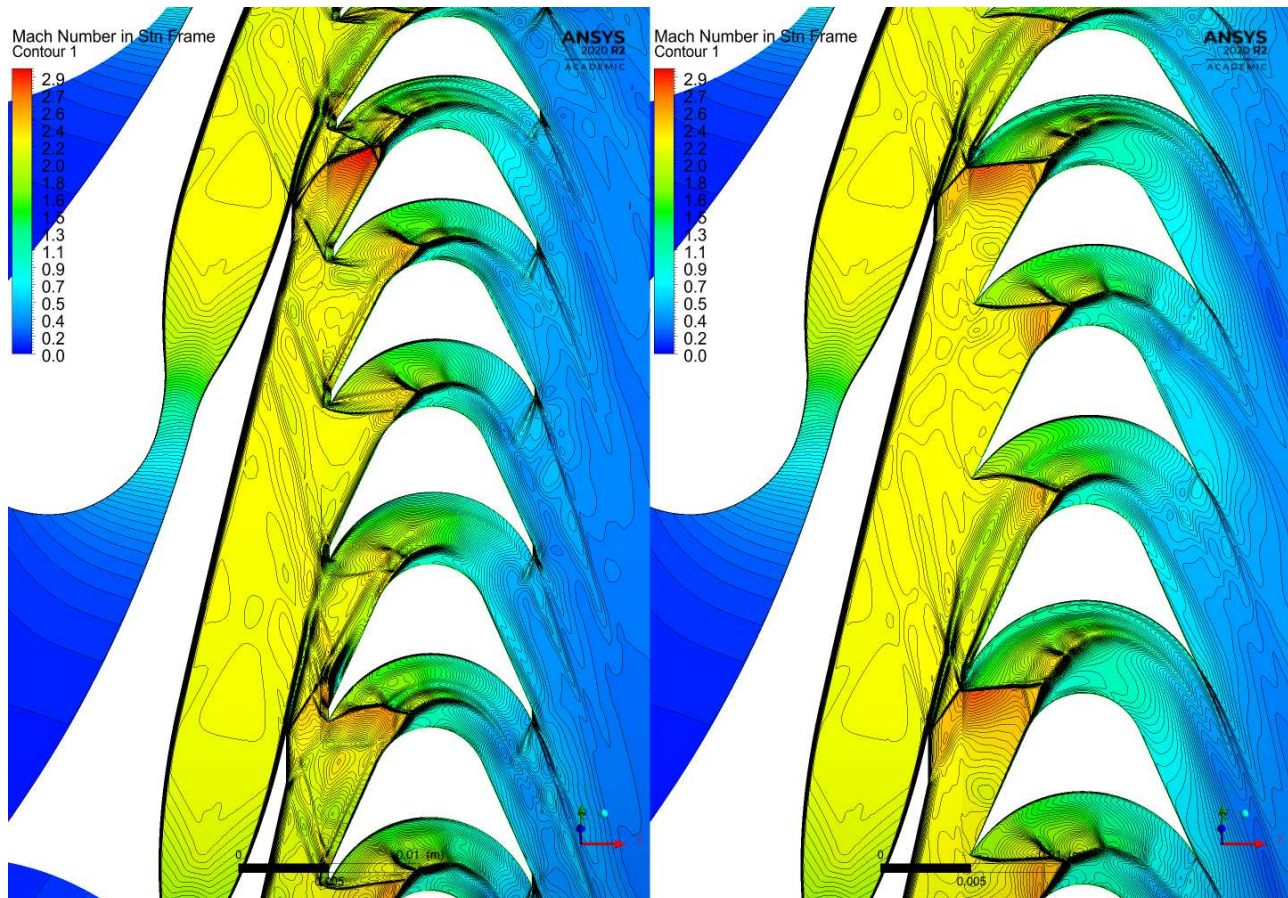


Figure 21. Midspan Mach contours in stationary frame - effect of sharpened rotor edges contra easily manufacturable design.

1D and 3D CFD comparison

A sensitivity analysis of the isentropic total-to-total efficiency with respect to the rotational speed was performed both in 3D CFD and using the 1D tool for off-design performance analysis. The results of this analysis is presented in Figure 22 below. On the contrary to the author's preliminary expectations, the operational curve is surprisingly flat and is rather insensitive to the effect of varying rotational speed at the constant pressure ratio, which indicates potentially beneficial operation with varying heat source.

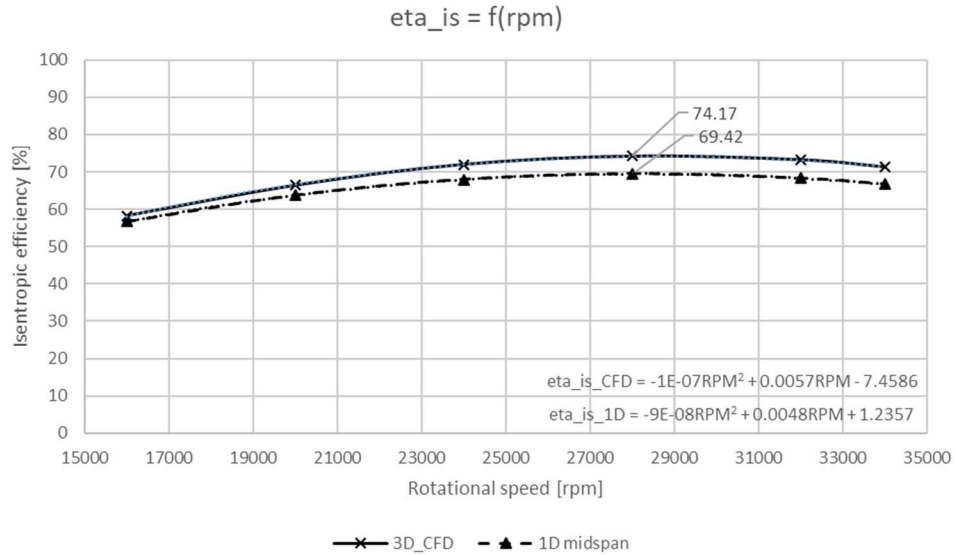


Figure 22. Turbine characteristics resulting from 1D model and CFD.

The differences in the results between the 1D model and 3D CFD model account to the loss correlations of the 1D model, which underestimate the efficiency in supersonic fluid flow exceeding Mach number of 2, since these loss models are originally derived from old turbopumps and corrected for smaller scale ORC turbines, they may underperform in the range of operation conditions varying strongly from the original verified region of validity. Another point is that the 1D model fails to predict the efficiency of the optimized nozzle designed by MoC. The CFD on the other hand well describes the detailed flow structures (shockwaves), verifies a well-designed MoC nozzle with uniform fluid flow at the outlet ant confirms a problematic region at the suction side of the rotor bucket where flow separation occurs due to large flow deflection angle together with intercepting shockwave from the rotor leading edge.

The next step for the numerical simulation track is a simulation of the whole turbine including inlet flow parts and outlet volute. Nevertheless, the final turbine design going for manufacturing has been fixed and the parameters are in Table 8.

Table 8. Optimized parameters of the designed axial turbine based on the CFD optimization.

Parameter	Value	Units
Rotational speed	28000	rpm
Partial admission	0.975	-
Stator outlet angle	13	°
Midspan diameter	100	mm
Blade height	5.5-7.2	mm
Turbine power output	11.44	kW

Isentropic total-total efficiency	74.23	%
-----------------------------------	-------	---

Off-design CFD analysis

Computational Fluid Dynamics simulation (Ansys CFX) was used to create an off-design performance map of the v1 machine. This map (Figure 23) contains information about the efficiency of the turbine in off-design turbine inlet pressure with varying rotational speed. The Pareto front (curve connecting maximum efficiency points for each rotational speed) of this off-design performance map is used as a control function for the rotational frequency (variable frequency drive of the generator) to maximize the seasonal yield of electricity production by the turbine. Significant increases in computational time for highly off-design inlet pressure of the hexamethyldisiloxane were observed, probably due to the strong shock formation in the exit of the supersonic nozzles and transonic conditions in the inlet of the rotor buckets inducing a bow shock on the leading edge of the blade. This high-fidelity simulation however besides know-how for control of the turbine brings fundamental understanding to the shockwave formation in dense fluids in off-design flow conditions.

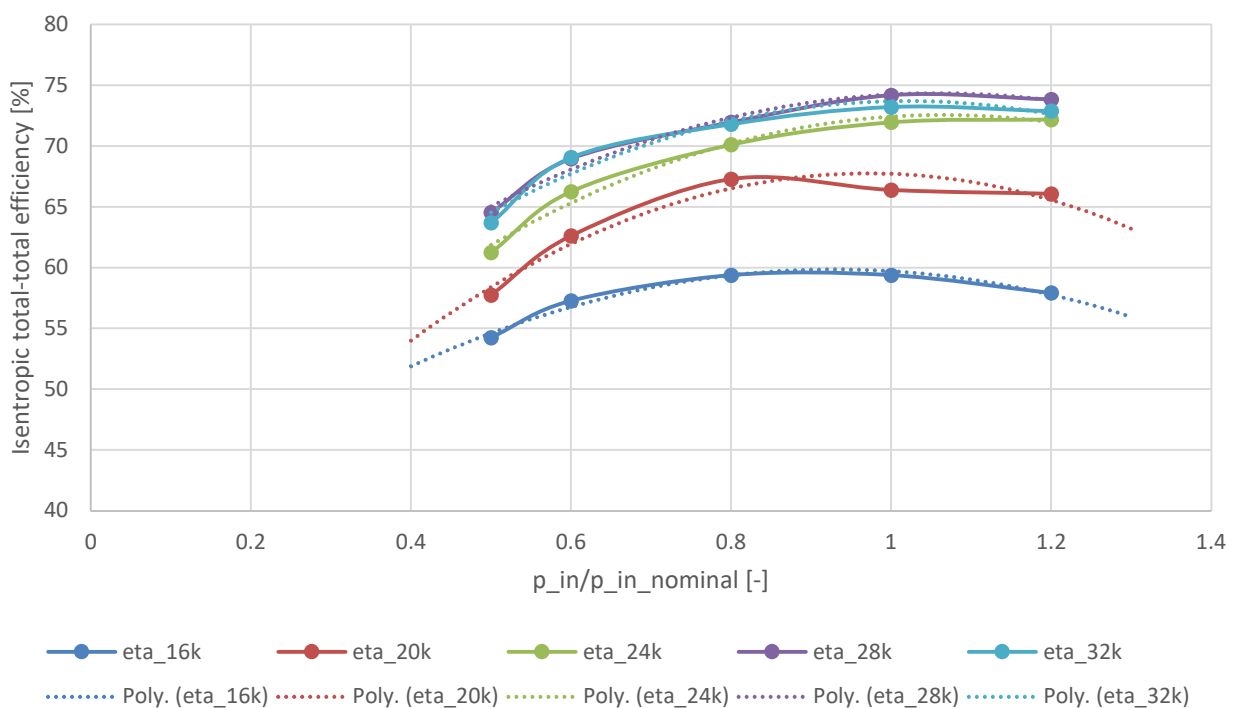


Figure 23. Off-design performance map of the v1 axial MM turbine based on 3D high fidelity CFD

MM turbine v2

Based on the operational experience from the axial supersonic turbine operating with MM, this turbine was re-modelled to better accommodate lower rotational speeds with higher efficiency. This measure aims at increasing safety of the operation of the turbine at higher rotational speeds, for which the

T A Č R

research team identified vibrations which exceeded safe operation. As any damage to the turbine when the ORC is in operation is highly dangerous it is a priority to avoid any possible leak of the working fluid that could result from a damaged turbine.

Thus version 2 turbine assembly was designed with a new concept of the shaft fit, new bearing design and turbine wheels which are more efficient at lower rotational speeds. This will not only increase the stability and dynamic behaviour of the whole machine, but also reduce the possibility of the damage. Also, thanks to the reduction in design rotational speed, the turbine can utilize larger shaft diameters (as the limiting factor of the rpm are bearings). Another aspect of the speed reduction is that the generator used to produce electricity would not overheat as much and its ceramic bearings won't operate on the very limit of its operational envelope. This whole stage redesign however comes with a drawback of lower peak efficiency. Comparison of parameters of the v1 MM axial supersonic turbine assembly and the v2 is shown in the Table 9 below.

Table 9. Comparison of parameters of the v1 and the v2 MM axial supersonic turbines.

Parameters	Unit	v1 turbine	v2 turbine
Turbine inlet pressure	kPa (a)	650	550
Turbine inlet temperature	°C	190	180
Mass flow rate	kg/s	0.303	0.25
Midspan diameter	mm	100	135
Design rotational speed	rpm	28 000	18 000
Design power output	kW	11.7	8
Isentropic t-t efficiency	%	74.2	72.9
Nozzle outlet Mach number	-	1.95	1.88
Rotor blade inlet flow angle	°	25.75	23.5
Rotor flow deflection angle	°	154.25	156.5

2.1.2 NTNU model

Model description

A mean-line methodology is developed to support performance prediction and design of axial turbines. The model is formulated with python programming language and is intended to be published as an open source software. The tool is constructed such that a wide range of axial turbine configurations are supported, and it offers the user control over modelling options such as loss correlation, deviation correlation and introduction of a blockage factor due to boundary layer development.

The NTNU model assesses the turbine at three stations for each cascade: inlet, throat and exit. In this way, choked flow conditions can be predicted. For analysis of turbine performance, turbine inlet stagnation state, working fluid, exit static pressure and rotational speed is given alongside with geometrical parameters. In addition, an initial guess of velocity at each station, exit cascade relative flow angle and static pressure at throats and between cascades must be provided. With these inputs, the model calculates mass flow rate, loss coefficients and Mach numbers at each state. However, for the flow to be consistent with mass conservation, principle of sonic flow and loss prediction (**Error! Reference source not found.**) an equation solver is adopted which adjust the set of initial guesses provided.

$$\begin{aligned}
 \dot{m}_{inlet} - \dot{m}_{throat} &= 0 \\
 \dot{m}_{inlet} - \dot{m}_{exit} &= 0 \\
 (Y_{definition} - Y_{loss\ model})_{throat} &= 0 \\
 (Y_{definition} - Y_{loss\ model})_{exit} &= 0 \\
 Ma_{thro} - \min(1, Ma_{exit}) &= 0
 \end{aligned}$$

Equation 1

In addition to the equations above, conservation of rothalpy and a thermodynamic library is needed for the analysis. For this model, CoolProp is used at first. Later the option of using Refprop is planned to be implemented.

For the preliminary design tool, the geometrical parameters, rotational speed, station velocity, cascade exit relative flow angle and static pressure at throats and between cascades are given as design variables. Physical flow is ensured by imposing the same set of equations solved by the equation solver as constraints.

The model is validated against experimental data with reasonable accuracy, with a deviation between predicted and actual efficiency of 1.1 to 4.5 % points. The model was validated with cases of both subsonic and supersonic turbines, and it was shown that the greatest deviation was observed for the supersonic cases. Strange behaviour was observed in the attempt to recreate mass flow rate vs. pressure ratio curves obtained by experimental data (Figure 24). The observed bump shows a weakness in the model and will receive attention for further work.

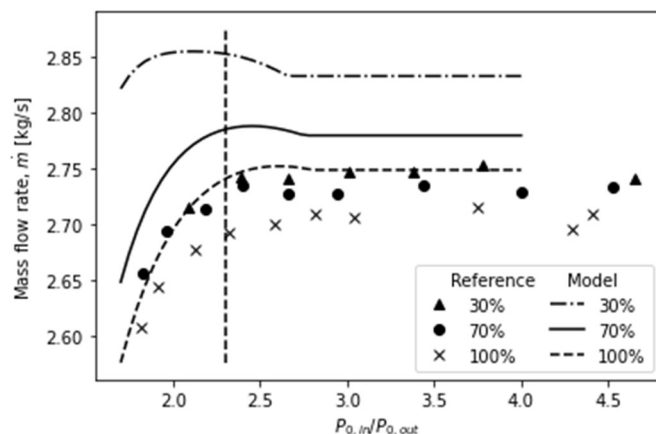


Figure 24. Mass flow rate vs. total-to-total pressure ratio at different rotational speeds.

The optimization method was also verified by comparing the output with a similar optimization tool. For same boundary conditions, the obtained geometry was similar, along with performance parameters.

Off-design model

The next step was to extend the design method to better account for off-design performance. This was conducted by formulating the objective function as a weighted average of isentropic efficiency at different operating points. Correlations within the loss model were included to make the model fit to predict performance at off-design conditions. Essential for this purpose is to implement correlation for incidence losses.

The model adopts a novel method to predict the critical state, and automatically detect which cascades that are choked or not. For this reason it is able to predict different combinations of choked stator/rotor. The model is validated against experimental results for two cases, one which chokes in the stator, and one which chokes in the rotor. The model correctly predicts the flow regime that occur, and predict the mass flow rate, torque and rotor exit flow angle for a wide range of pressure ratios and angular speed with an error within 5%. This makes the model suitable for robust preliminary design of axial turbines,

where the objective function is a weighted average of the efficiency at different operating points. The purpose of this is to design turbines that performs better over an annual perspective to increase the yearly power output and return of investment for ORC systems. The model was further improved in accuracy and robustness through a collaboration with the Technical University of Denmark (DTU).

2.2 Non-orthodox turbines - Elektra turbine

2.2.1 Initial considerations

Two non-traditional designs were preliminarily considered, namely Electra and Curax (Curtis radial-axial) turbines. Both are velocity compounded stages with a prospect of achieving significantly lower rotational speed in comparison to standard impulse stage, thus fitting for applications with rather extreme pressure ratios.

Elektra (velocity compounded radial re-entry turbine) turbine is first explored as a 5kW Air-Demonstrator (10 to 1 bar, 29.000 rpm), see Figure 25.

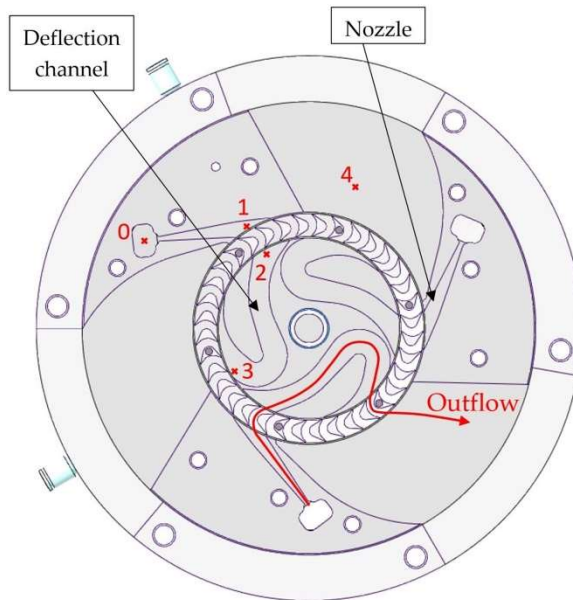


Figure 25. Sectional view of the Elektra turbine (Version 1).

Robust design, only one wheel for several wheel passes, ongoing work is to optimize the geometry of the turbine in CFD and to increase the overall efficiency (V1 about max. 34% total-to-static isentropic) and implement the most promising in the Demonstrator. First optimizations measures included cover between the deflection channel and the rotor and further optimizations include different shape of the deflection channels, splitter blades in the DC's, different nozzle shapes, etc. (see Figure 26)

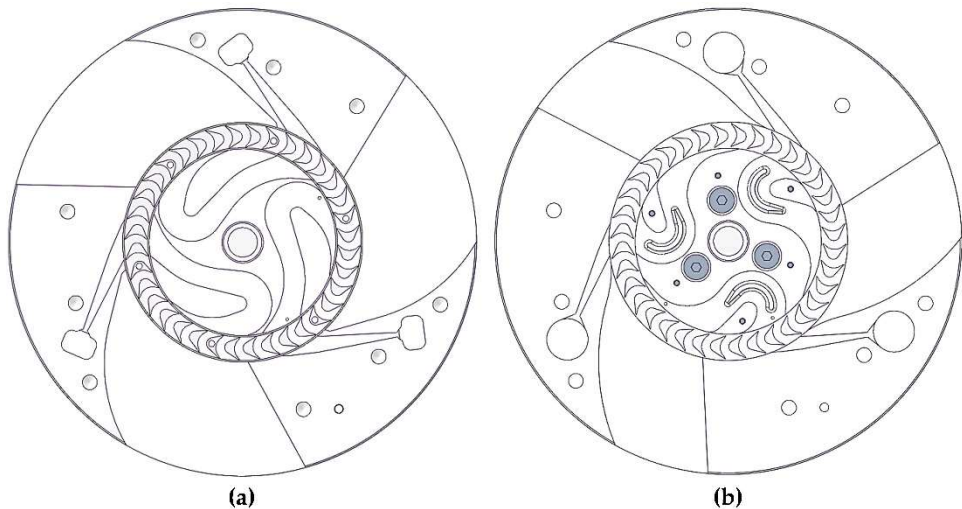


Figure 26. Elektra design comparison: (a) Version 1, 2a and 2b; (b) Version 3.

Due to these optimizations, the efficiency could be increased from about 34% max. (V1) to about 45% max. in (V3) (see Figure 27) with Versions with a 3D-printed wheel (2b) and the Basic design with cover (2a) in between.

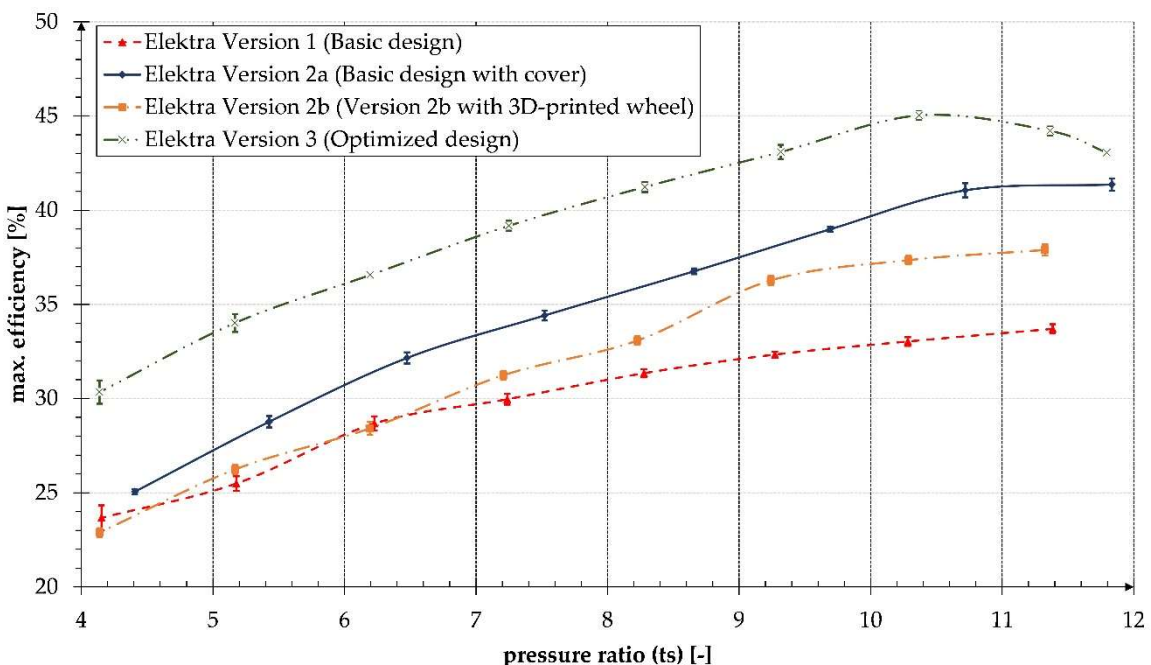


Figure 27. Maximum efficiencies over pressure ratio for the different versions.

In Figure 28 the 3d printed (left) and the milled alloy wheel (right) can be seen. The 3d printed wheel was postprocessed after the printing. In Figure 27 the efficiency drop of the printed wheel compared to the milled wheel can be seen. The efficiency of the 3d printed rotor in the whole efficiency range is about 1.5 to 4%-Points lower than the milled one. This drop in efficiency can be explained by the high surface-roughness of the printed wheel in the blade area.

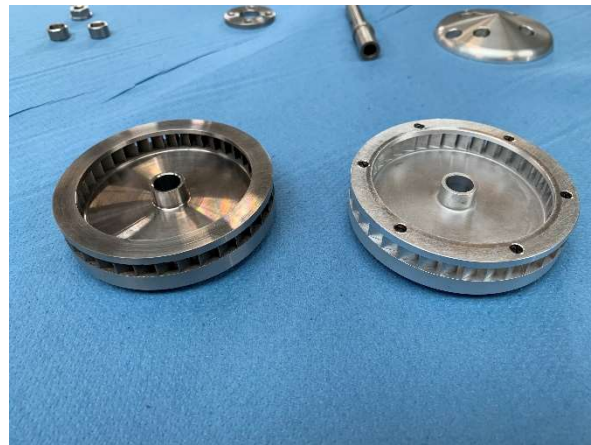


Figure 28. Elektra turbine - comparison between a milled alloy rotor-wheel and a 3d printed MS-1 rotor-wheel.

The Curax turbine was considered based on a small radial Curtis consideration, where at the outlet of the inner second bucket ring there is too little flow area. Therefore, a first pure radial stage (Laval nozzle + impulse buckets) is combined with zero-reaction radial guide vanes and a small reaction radial-axial impeller. The design ($d = 80\text{mm}$) has already been investigated by CFD with air considered for preliminary tests (Figure 29).

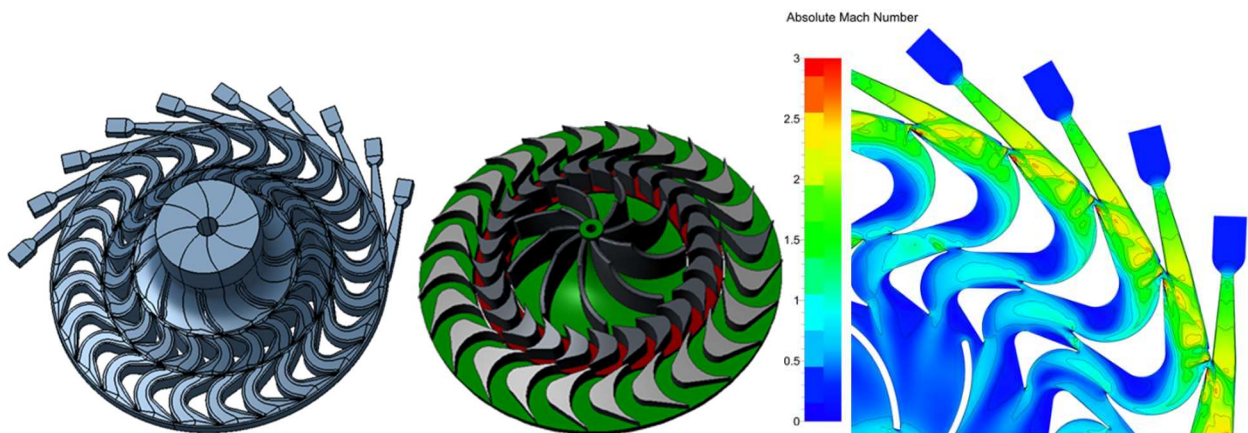


Figure 29. Curax turbine 3D model of the channels, blade wheel and first CFD investigations.

2.2.2 ORC – Elektra design

After initial investigation of the two non-traditional turbines - Electra and Curax (Curtis radial-axial), both velocity compounded stages with a prospect of achieving significantly lower rotational speed in comparison to standard impulse stage where air was considered as working fluid, the Elektra concept was chosen also for further investigations considering organic working fluid. Parameters of the CTU ORC system were chosen as it is a case with high pressure ratio where the benefits of this type of turbine can be more pronounced and as it is achievable within the project to perform experimental testing (isobutane rig is still not operational).

1D design

The tool used to design the Elektra turbine is an in-House Tool called “1DTDT” 1D Turbine Design Tool, which is able to generate the geometry data, power output and the turbine efficiency for axial impulse, two-wheel velocity compounded Curtis and radial cantilever quasi impulse turbines. The 1DTDT has been further developed, so that it can also be used to design velocity compounded radial re-entry turbines like the Elektra turbine for given boundary conditions. The geometry data out of the tool was used to design a first version of the turbine and afterwards, CFD calculations were carried out. The results of the simulations were analyzed, potential for optimization was worked out and new optimized versions then again have been calculated. Table 10 shows the boundary conditions and the basic design parameters of the turbine. Afterwards, the results of the CFD calculations of the Elektra turbine are described.

Table 10. The boundary design conditions for the Elektra turbine.

Parameters	Unit	Elektra Turbine
Working fluid	-	MM
Total inlet pressure	kPa	650
Total inlet temperature	°C	190
Required mass flow rate	kg/s	0.303
Static exit pressure	kPa	55
Wheel diameter, D_{out}	m	0.255
Wheel diameter ratio, D_{out}/D_{in}	-	0.90
Final wheel pass degree of admission	%	50
Rotational speed, n	rpm	3,000
Nominal design expansion efficiency	%	40.0

The velocity triangles in Figure 30 below illustrate the working principle of the velocity compounded radial four-fold re-entry MM Elektra turbine from a basic fluid dynamic for turbomachinery theory perspective. Thanks to the four-stage velocity compounding, a rotational speed of only 3000 rpm is feasible what enables the application of a cost-effective “out-of-the-shelf” generator. A simple impulse type turbine with the same wheel diameter would require 12,000 rpm, a reaction type turbine approximately 17,000 rpm. Both turbines need therefore an expensive high-speed generator.

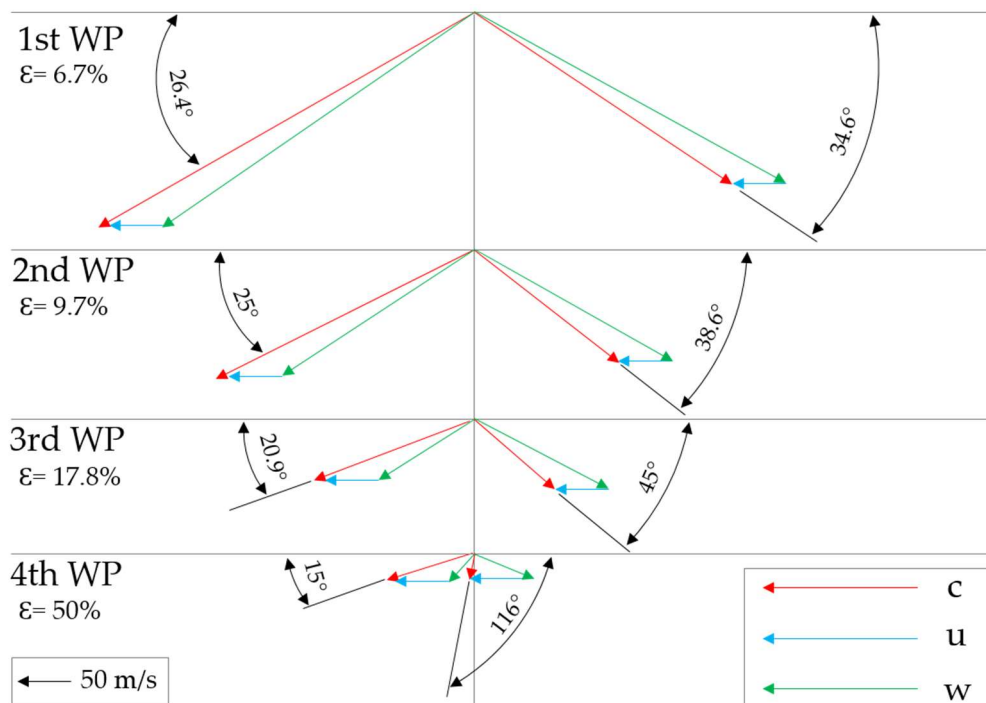


Figure 30. Velocity triangles of the velocity compounded radial four-fold re-entry MM turbine (absolute velocity c , relative velocity w , circumferential velocity u , partial admission ϵ)

Another important feature of the Elektra turbine is the re-entry concept. A classical axial Curtis turbine [13], which is the ancestor of all velocity compounded turbines, would need four bucket wheels and a long shaft with extra bearings. As shown in Figure 31, the Elektra architecture uses a big diameter wheel four times thanks to re-directing the flow three times back to the wheel. Thus, the single bucket wheel can be directly mounted on the generator shaft. No additional bearings, no coupling is required.

As an important aspect for allowing to validate the model with experimental data, a submodel compensating for liquid content in the working was added to the 1D model. Even though the expanding MM is always in superheated state due the shape of the saturated vapour line, the MM test rig circulates an oil alongside the MM for ensuring proper operation of pumps and RVE, when installed.

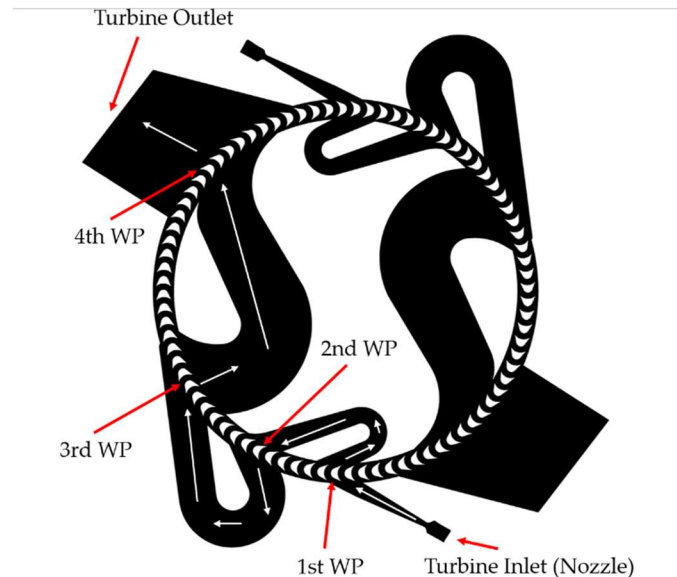


Figure 31. Turbine with the flow direction shown with white arrows and wheel passes (WP) with red arrows.

CFD design and investigation

Figure 11 shows the absolute Mach number distribution of the first version of the Elektra turbine (V1). The total-to-static isentropic efficiency of the CFD calculation (V1) was 44.45 % compared to about 70 % in the 1D-Tool. This high deviation can be explained by the tools simple loss model, which for more than one blade pass, strongly underestimates the losses. The Mach number distribution in Figure 32 also showed a lot of potential to increase the overall efficiency of the turbine as can be seen by the flow separations in all of the deflection channels of the turbine. Also, the Laval nozzle does not work as designed and seems to overexpand the fluid with a shock at the end of the divergent part.

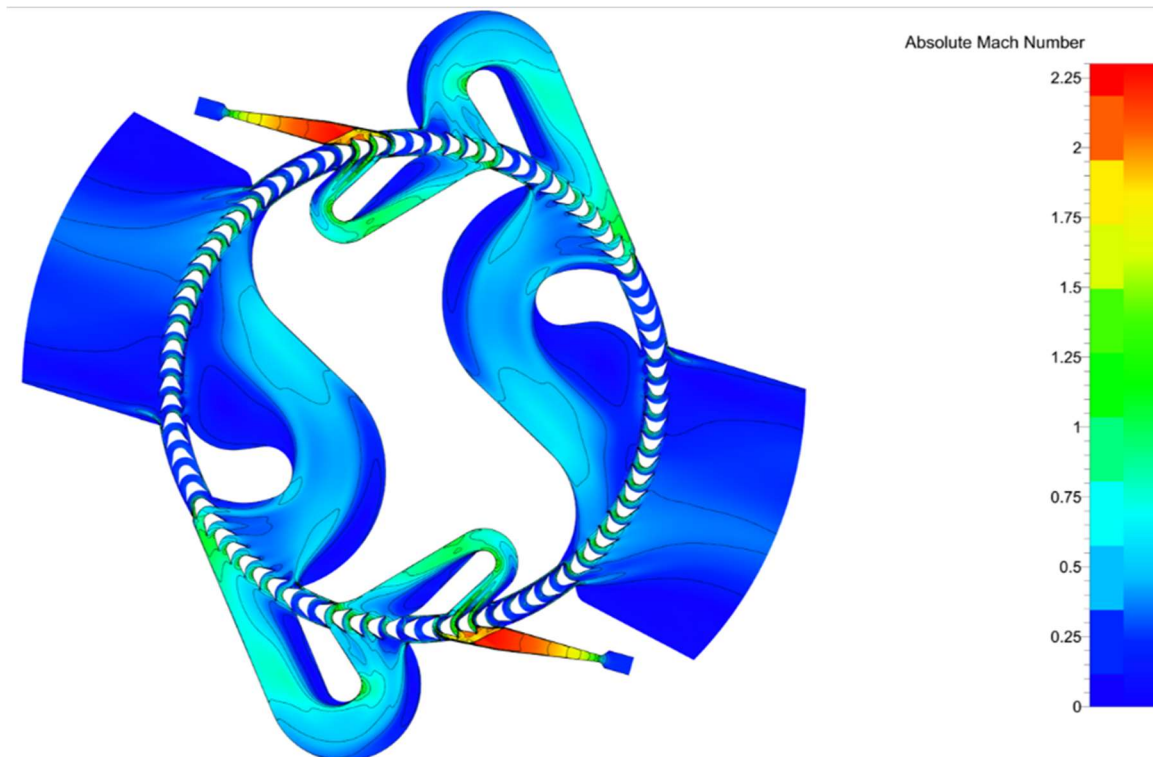


Figure 32. Absolute Mach number plot of the Elektra turbine (V1).

In Figure 33 the absolute Mach number distribution of the second version of the Elektra (V2) is shown. All of the changes compared to Version 1 are shown in red circles. First, the outlet area of the nozzle has been decreased, to reduce the shock at the outlet of the nozzle. Second, the width of the first deflection channel has been decreased to reduce flow separation and third, the third deflection channel area has improved flow guidance and the outlet area has been reduced. By these changes, the efficiency could be increased from 44.45 % to about 46 %.

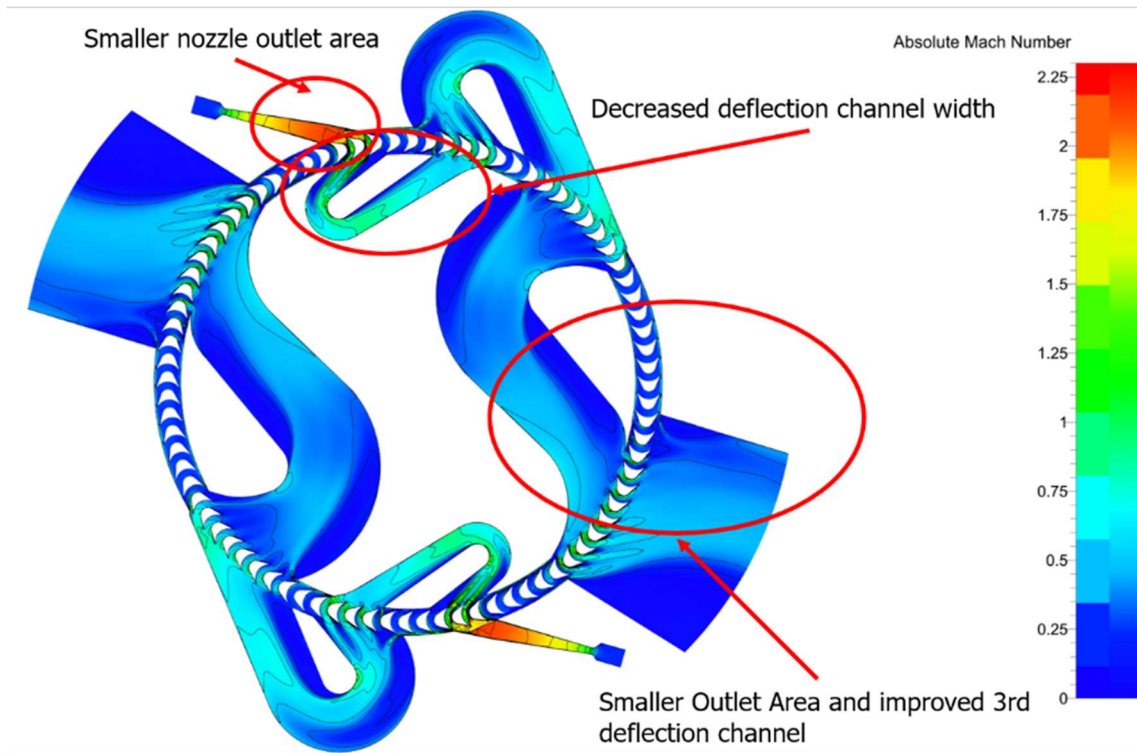


Figure 33. Absolute Mach number plot of the Elektra turbine (V2).

In Figure 34 the static pressure distribution through the whole turbine in the state of Version 4 can be seen. As designed by the 1D-Tool, the static pressure through the turbine should be constant (velocity compounded). For two of the three deflection channels, this pressure distribution is achieved. The first deflection channel static pressure is about 60,000 Pa higher as can be seen by the orange and dark red areas. This pressure distribution seems to build up, as the flow in the second wheel pass is choked, which also explains the sudden pressure increase.

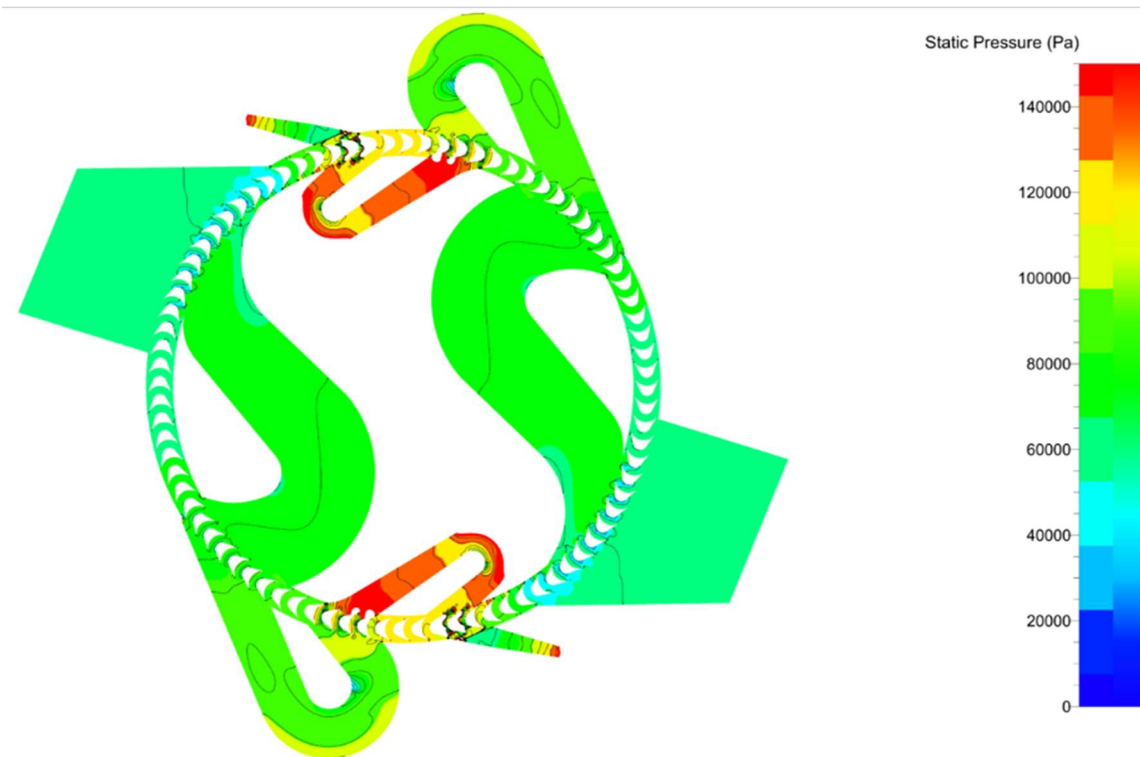


Figure 34. Static pressure plot of the Elektra turbine (V4).

To cope with the problem of the static pressure distribution mentioned above, different blade channel widths have been investigated. Figure 35 shows the absolute Mach number distribution of the Version 4 (above) and Version 4_4_5 (below). The 4_5 stands for 4.5 mm blade channel width. As comparison, the designed blade channel width for Version 4 is 3.5 mm. By this change of the channel width from 3.5 mm to 4.5 mm, the static pressure in the first deflection channel could be decreased by approx. 20.000 Pa. But this change also influenced the flow between the blades, as the shock system is more pronounced in Version 4_4_5 compared to Version 4.

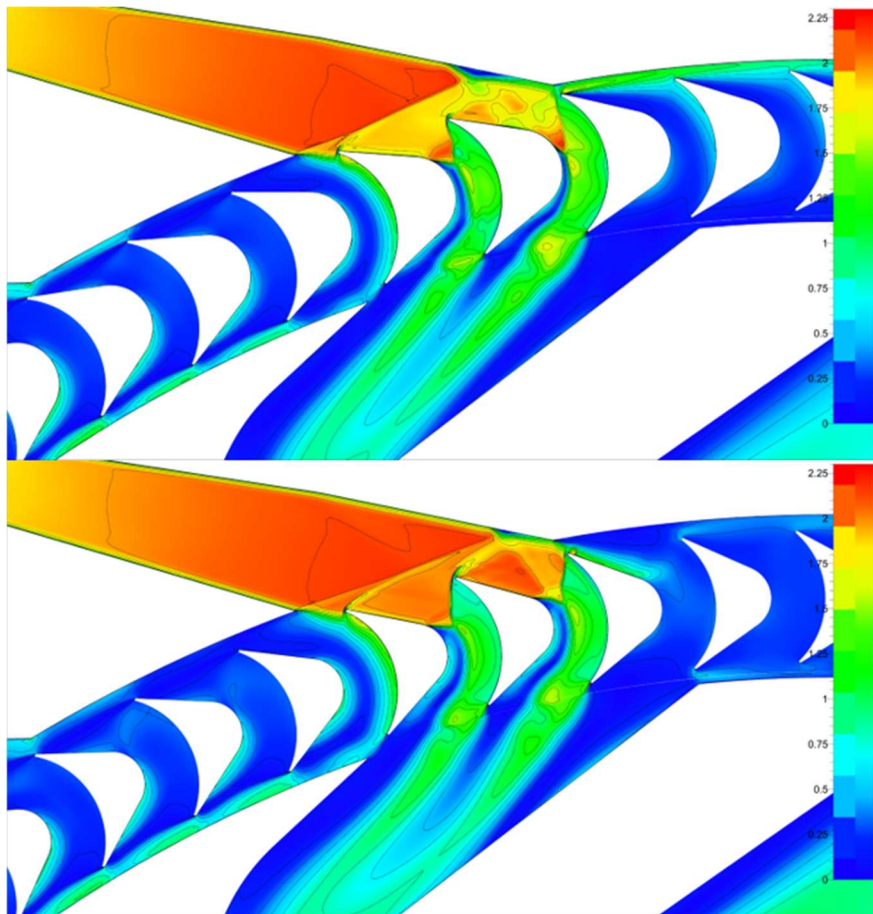


Figure 35. Absolute Mach number plot of the Elektra turbine (V4 top) (V4_4_5 bottom).

By the approach of changing the geometry of the nozzle, deflection channels and blades, 16 different Version of the Elektra turbine have been simulated and investigated. Figure 36 shows the total to static isentropic efficiency of all the different versions. All of the blade channel width changes have been performed with Version 4, as this Version was the best out of the first 9 Versions. As can be seen, none of the modified Version 4 calculations managed to achieve a higher efficiency than the basic one. This can be explained by the change in flow through the blade channels mentioned above. After this, an unsteady simulation of Version 4 has been carried out. The results showed, that there is just a slight drop in efficiency due to transient behavior. This small drop can be explained by the relative position between the nozzle, blades and the deflection channel in the non-transient calculations. If the positioning in the steady-state simulation provides a strong shock system, the overall efficiency can be lower than in other relative positions. In this way, the efficiency drop from the steady state to the unsteady simulation does not occur to strong. For further designing of the Elektra turbine, the nozzle, deflection channel and blade geometry of the Version 4 have been used.

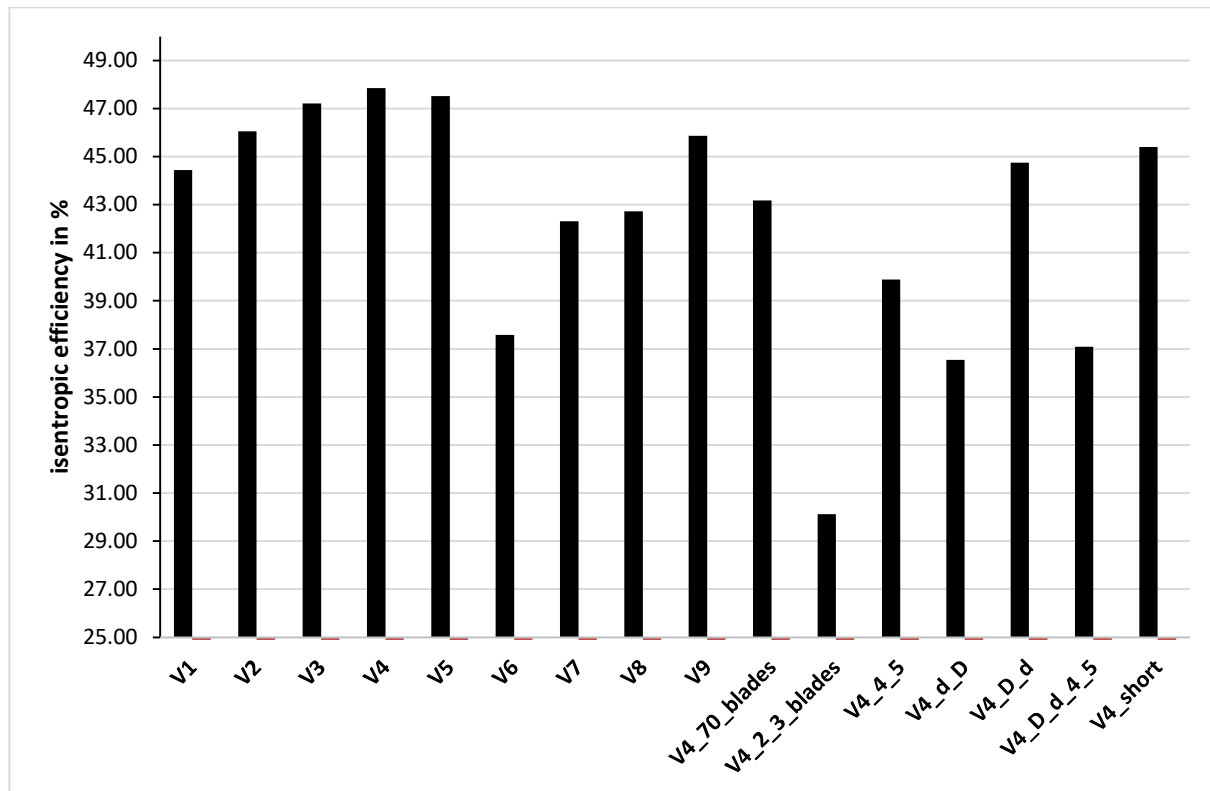


Figure 36. Isentropic efficiency of different Versions of the Elektra turbine.

2.3 Rotary vane expander

In order to improve the reliability of models and operation prediction of the RVE, there were performed long term tests of the reliability of the 8 kWe expander in our MM test rig (prior to redesign for isobutane and air). Out of the data for several thousand hours of operation was obtained part load performance and checked with the existing model. Figure 37 shows the results of this analysis with rather flat efficiency curve for this technology and relatively small departure from the predicted performance.

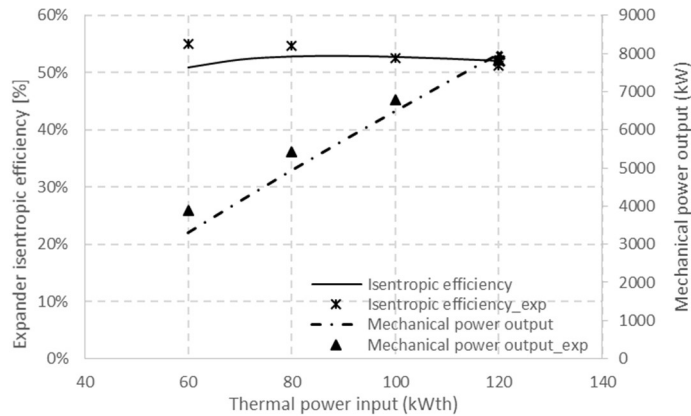
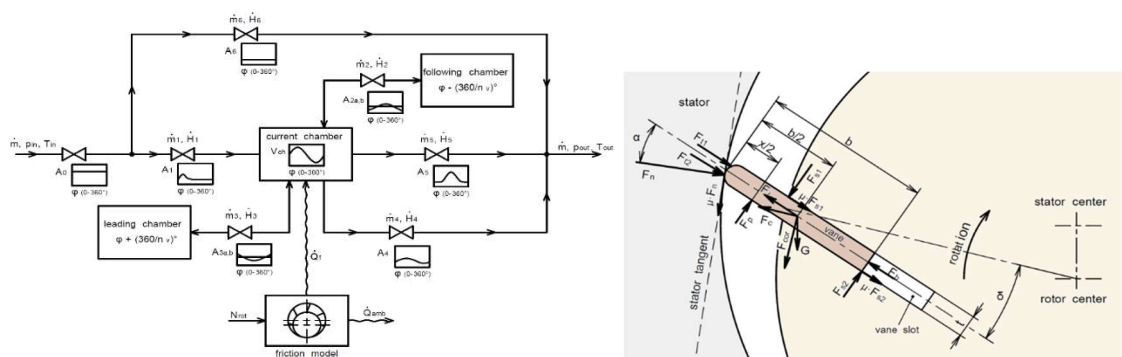


Figure 37. Off design modelled and measured characteristics of an MM RVE.

The model has been redesigned to allow the use of also alternative working fluids. It was also redesigned in order to increase calculation speed, especially regarding the pressure in the working chamber and pressure under vane. The final design model with implemented the isobutane working fluid instead of MM (remodelled to be able to choose nearly any fluid from the REFPROP database) is composed as a 1D model of various flow constrictions representing the working fluid flow combined with a friction model of the vanes and heat transfer between the expander and the surroundings (figure below, upper left). In order to get all the data accurately, dynamic model of the vane is included (forces described in Figure below, upper right) where the force acting on the blade is also related to the pressure in the slot under the vane, for which is included additional model (Figure 38 bellow, left and right). From the output are the important parameters vane tip force (friction loss, loss of contact), Hertzian contact stress (vane/stator) and bending stress on the vanes.



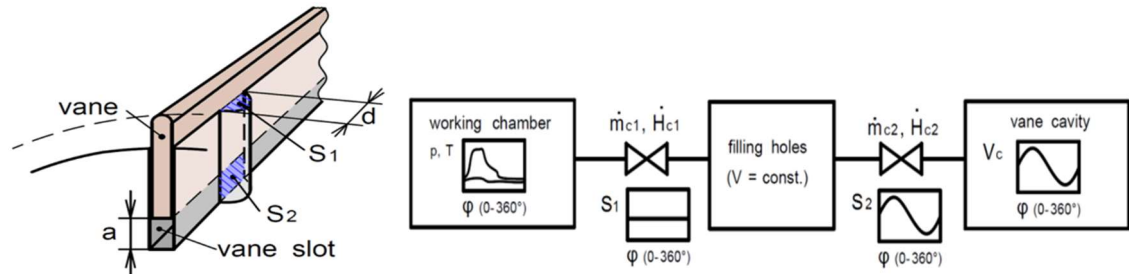


Figure 38. Representations of the components of the RVE design model, from top right 1D overall model, dynamic vane model, flow path representation to the vane slot and model of the fluid flow between the chamber and vane slot.

First are provided parameters for the isobutane design. Parameters of the EXPAND rig near maximum pressure (1210 kPa inlet pressure) were used to in the model along with a genetic algorithm optimization to obtain the RVE design. There is no single optimum as there exist several tradeoffs regarding maximum efficiency, moderate loading of the bearings, bending stress of vanes, loss of contact (vane/stator), range of RPM etc. One example can be shown in vane number increase from 6 to 8 which worsens efficiency but lowers pressure difference between chambers, thus provides better resistance to loss of contact between vane and stator. The results of the modelling after selection of specific case are presented in Table 11. Example of the overall vane tip force and bending stress are then in Figure 39.

Table 11. Isobutane RVE design parameters.

Stator diameter (mm)	90 ÷ 100
Length/diameter ratio (-)	~ 2
Number of vanes (-)	6
Expansion ratio (-)	~ 2.5
Mechanical power output (kW)	15 ÷ 17
Mass flow rate (kg s⁻¹)	~ 0.4
Isentropic efficiency (-)	0.65 ÷ 0.7

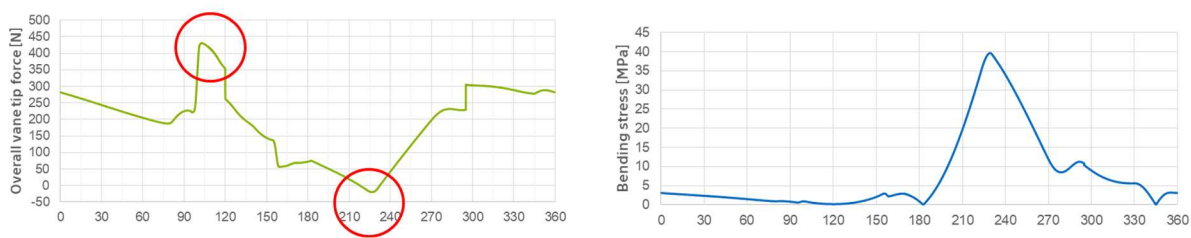


Figure 39. vane tip force and bending stress of the designed isobutane RVE.

One of the objectives of the project is to assess the feasibility of the expanders in various applications and sizes. Therefore, the RVE design model, developed before, has been applied for a different scale

system, specifically for about 12 kWe output fitting for a cogeneration system scaled-up to thermal output 200 kWth. The expected parameters of the scaled-up expander along with the previous expanders under nominal conditions are presented in Table 12. Note, that the parameters are a result of an optimization for maximal power output of the cogeneration cycle. Plan for future are including also assessment of a domestic microcogeneration size, i.e. about 1 kW.

Table 12. Summary of the previous and newly designed RVE parameters under nominal conditions.

	Units	50 kWth unit	120 kWth unit	200 kWth unit
Expander design power output (mech.)	W	3400	8607	13150
Expander design isentropic efficiency	%	60.6	51.9	51.8
Measured power output (mechanical)	W	3370	8223	13.5
Measured expander efficiency	%	61	56	57.6
Cycle net efficiency of power production	%	4.0	5.2	4.7

The 1D model developed for the RVE was used for a sensitivity analysis of the new upscaled RVE. The analysis is calculated for a thermal power output of 205 kW and condensate subcooling of 18.5 K, taking into account the impact of emission pressure on the entire cycle. In the context of rotary vane expanders, one important parameter to consider is the axial clearance, which refers to the gap between the vanes and the stator cylinder (Figure 40). Currently, the level of axial clearance being used is around 0.1, with a realistic range of 0.05 to 0.15 depending on the specific design and manufacturing tolerances. This parameter is crucial for the construction of the expander as it affects the efficiency and lifetime of the vanes. Too much clearance can result in a phenomenon called vane chatter, where the working chamber is not properly formed leading to excessive leaks of the working fluid and reduced efficiency.

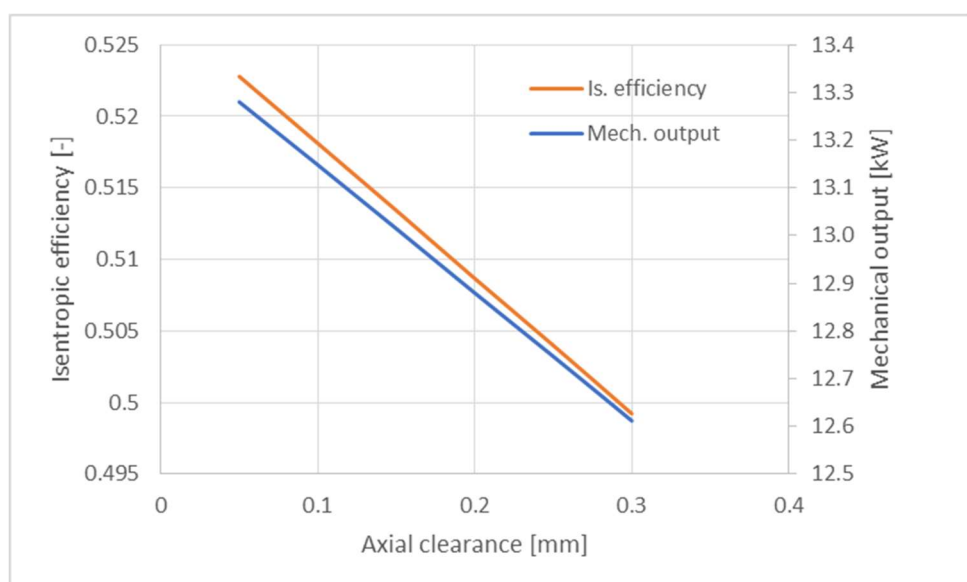


Figure 40. Sensitivity analysis of axial clearance on RVE performance.

Figure 16: Sensitivity analysis of axial clearance on RVE performance

The Figure 41 represents the performance of a Rotary Vane Expander (RVE) as a function of condensing pressure, respectively the effect of varying the condensing temperature. As can be seen, the efficiency of the RVE increases with an increase in condensing pressure. The expander in the corresponding cycle operation power has an optimum around 70 kPa. A low outlet pressure means a colder condensate and thus a lower temperature and pressure at the admission, which results in a lower cycle efficiency.

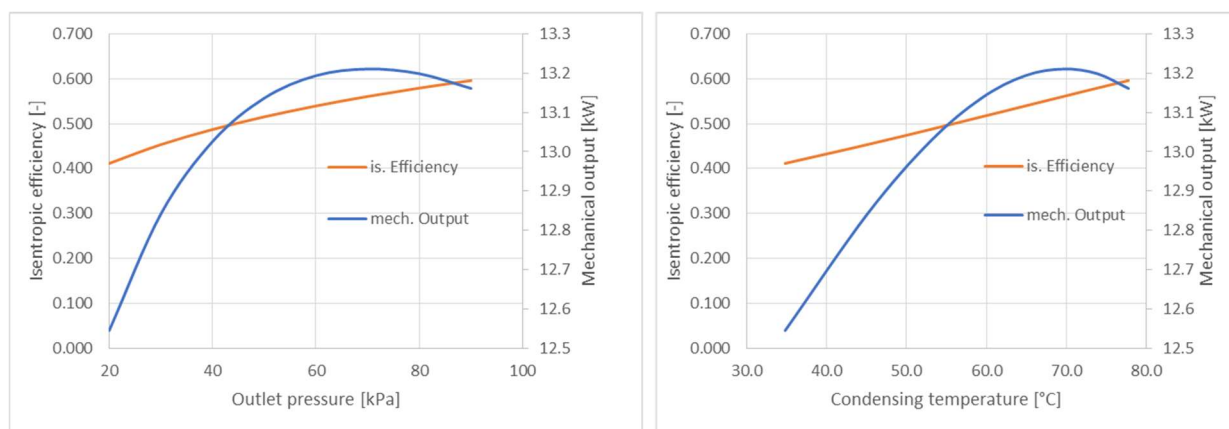


Figure 41. Sensitivity analysis of condensing pressure and temperature on RVE performance.

Figure 42 represents a sensitivity analysis on the dimensions of the rotary vane expander (RVE), specifically the length to diameter (L/D) ratio. The analysis shows how the L/D, and corresponding expansion ratio increasing with the diameter, affects the efficiency and power. As can be seen from the figure, the efficiency increases with an increasing diameter and expansion ratio. However, it is important to note that as the diameter increases, the weight and cost of machining the expander also increases. Therefore, the optimal diameter was fixed at 91mm to balance efficiency and cost.

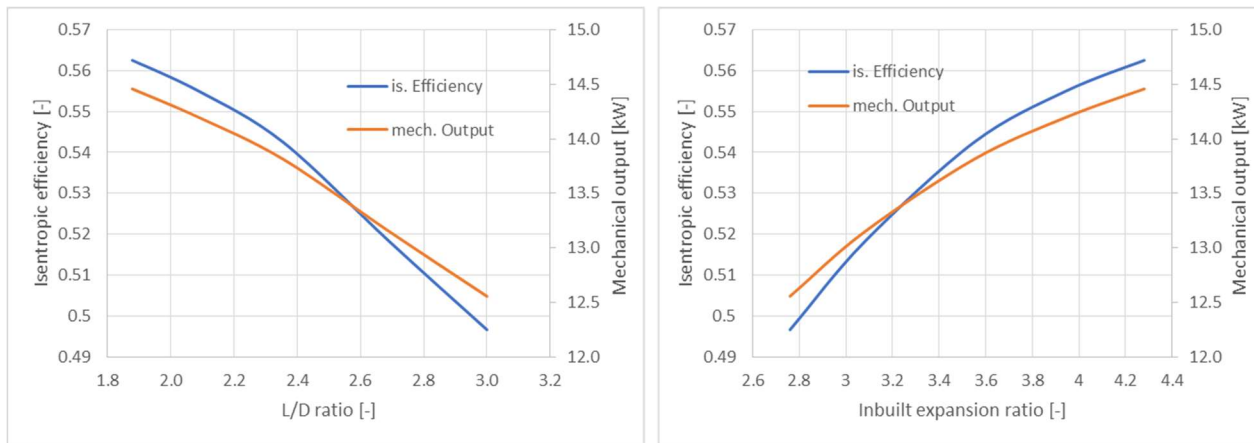


Figure 42. Sensitivity analysis of L/D and inbuilt volumetric ratio of RVE performance.

After the project change was negotiated as the isobutane tests were no longer an option due to rig issues, a scaled down relatively small testing RVE for dry operation has been modelled for operation with air test rig. For practical applications, this size of about 1 kW corresponds to domestic microcogeneration application field of ORCs.

It is a laboratory-tested rotary vane expander - which, unlike competing machines, is capable of oil-free operation thanks to the unique tribological pair in the vane-stator contact. The functional sample of the rotary vane expander is designed for operation with compressed air in the pressure range of 6-10 bar(a), however its hermetic design also allows operation with innovative low GWP and zero ODP refrigerants such as R1233zdE, R1336mzz(Z) or R1234yf, as well as natural refrigerants (hydrocarbons or CO₂). The design power of the machine is in the higher hundreds of watts. Its future application is, for example, in systems for the conversion of low-temperature waste heat recovery ORCs, or for the replacement of expansion valves as an expansion machine for saving throttled energy (heat pumps, piping systems). The use of resistant sliding coatings on the surface of the vane, which is in sliding contact with the surface of the stator, enables operation without lubricating oil, which results in significant savings in investment and operating costs, which are further enhanced in the case of heat circuits with oil circulation during operation, which also increases the efficiency of waste heat to electricity conversion.

The sliding coatings are based on DLC (diamond-like carbon) technology, which is plasma vapour deposited on the machined and polished surface of the vanes and stator. This coating is extremely hard and protects the surface of the vane and stator, but also under load, the diamond-like surface dehybridizes to carbon and thus lubricates the friction surface. Therefore, the machine can operate without an additional lubrication oil loop or oil being dissolved in the expanding working fluid.

The RVE is designed using an in-house developed tool [14] by the key member of this research project. The major difference is in the absence of lubricating oil and thus dry operation of the machine, which brings severe challenges to the mechanical design.

Expander speed is selected with respect to a possibility of direct coupling with asynchronous generator. The number of vanes influences the expansion ratio of the RVE, friction loss and also bending stress of

T A Č R

the vanes. The accurate prediction of internal leakage losses is a key issue to ensure nominal operation of the expander in the real operating conditions. Incorrect design of the expander can considerably affect the pressure in the evaporator, which can decrease the efficiency of a whole system. The main dimensions of the expander are given by the recommended geometric ratios. The dimensions also influence the leakages, friction loss and of course production costs. The position of the inlet affects mostly the expansion ratio and inlet pressure loss. Therefore, the final design of the expander is a result of a multi-parametric optimization.

3 WP3 - Expander Manufacturing, Assembly, Commissioning

3.1 Axial MM turbine mechanical design, manufacturing and assembly

3.1.1 Overall concept

Mechanical design works started with several preliminary concepts for the turbine of which one is shown in Figure 43 – a mechanical concept of a magnetic coupling, rolling ball bearings and a high speed permanent magnet generator outside of the turboexpander assembly and the whole turbine is hermetically sealed to eliminate leakages.

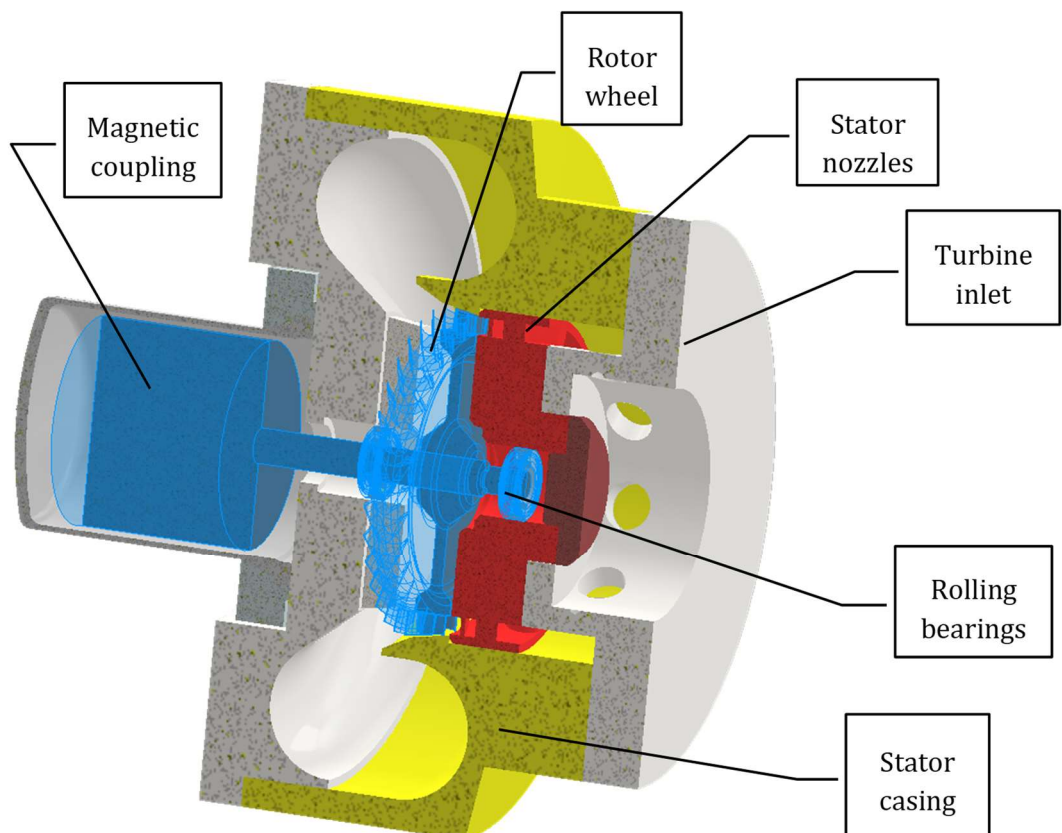


Figure 43. Preliminary mechanical design of the turbine assembly with magnetic coupling.

Additionally, were in overall mechanical design concept explored possibilities of utilizing a planetary gearbox for subsequent operation with a standard asynchronous generator or several concepts of the whole turbine package assembly regarding electrical power output and generator. High speed generator has resulted as the most feasible option. Larger discussion of selection of this aspect for the mechanical design is in the expander assembly consideration.

3.1.2 Final v1 design

The design including magnetic coupling, rolling ball bearings and a high-speed permanent magnet generator however prevailed, while it was found that the generator can be adopted from spindle motors available for machining applications. Since the generator is outside of the turboexpander assembly, the whole turbine is hermetically sealed to eliminate leakages.

The turbine is designed to be fitted onto the frame together with other ORC components located in the container of a biomass fired micro CHP unit, replacing the rotary vane expander for which has the rig been originally designed. To keep the amount of necessary changes as low as possible, the turbine is to be placed at the same position - between the evaporator and condenser with superheated vapour inlet and outlet located in the same positions.

A description of the auxiliary components of the turbine follows, together with the visual representation are in Figure 16. The vapour at the inlet passes through a fitting into a distributor, which redirects the high-pressure vapour into the stator nozzles. This parts and also others are sealed using FPM O-rings. Stator nozzles are press-fitted with an interference fit into the casing, thus eliminating tip leakage. Stator wheel also serves as a housing for the rotor shaft bearings. An axial gap of 0.75mm is designed between the stator and rotor wheel. The rotor wheel is a shrouded wheel with constant tip diameter cylindrical blades, increasing in blade height by reducing hub diameter. The rotor is secured on the shaft with feather keys, thus transferring torque onto the shaft. A 0.75mm gap is also designed between the rotor shroud and the casing. The shaft at the designed speed of 28krpm is mounted into sealed bearings with high temperature lubricant, which should be able to withstand the high temperatures and rotational speed. The secure operation of bearings is still not sure and will be experimentally tested with air, eventually to be replaced for a different model. The shaft then uses a magnetic coupling to transfer mechanical power out of the hermetically sealed space of the turbine casing. The coupling at the outer side spins the shaft of the high speed generator (originally a CNC milling machine spindle is used for that purpose). The vapour at the outlet from the rotor blades enters a volute which collects the working fluid and redirects it tangentially towards the outlet tube connected to the brazed plate condenser, where the vapour condenses and transmits heat into the hot water heating system of the connected building. The turbine casing is fitted with in total four pressure taps measuring static pressure at the inlet to the stator nozzles, at the outlet of the supersonic nozzles, at the outlet of the rotor blades and at the outlet tube.

The design of the turbine is shown in detail with component description in Figure 44 and when complemented with the generator in Figure 45.

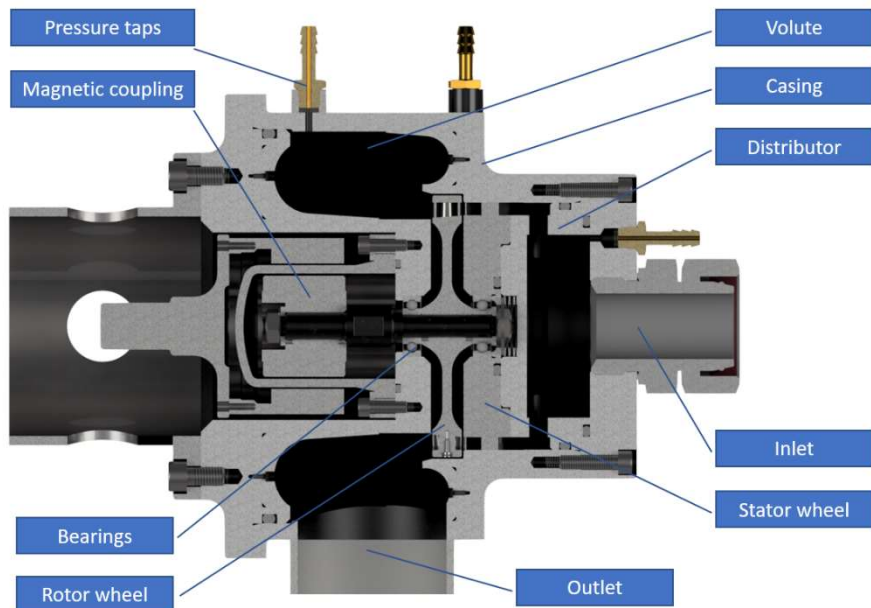


Figure 44. Final mechanical design of the turbine assembly – detail.



Figure 45. Final mechanical design of the turbine assembly with magnetic coupling and generator.

In order to perform first tests at lower power rating, two components with stator blades were designed, one (optimized) with full admission and one with the same geometry, but partial admission, to operate at air testrigs and smaller ORC test stands.

3.1.3 Design details & assembly

Finalised design of the version 1 MM axial supersonic turbine assembly is illustrated in Figure 46 and Figure 47. During assembly several improvement points were identified, which were adjusted in the following design version (v2) for easier and more error-prone assembly of the turbine.

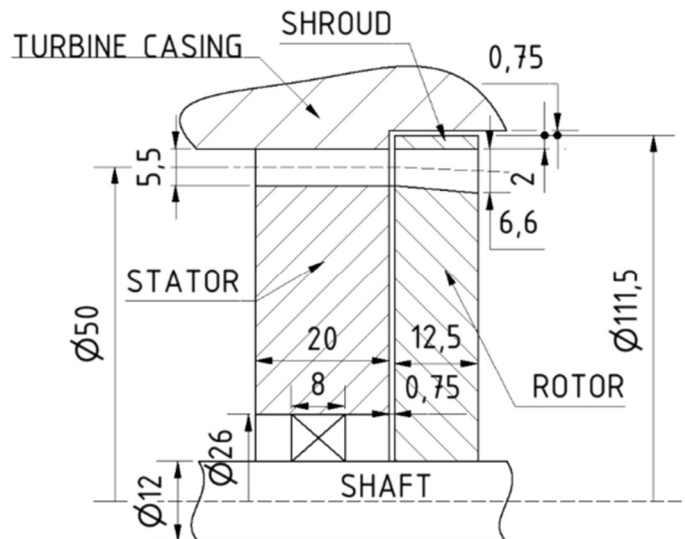


Figure 46. Axial high-speed turbine assembly – schematics of the detail of the shaft assembly v1.

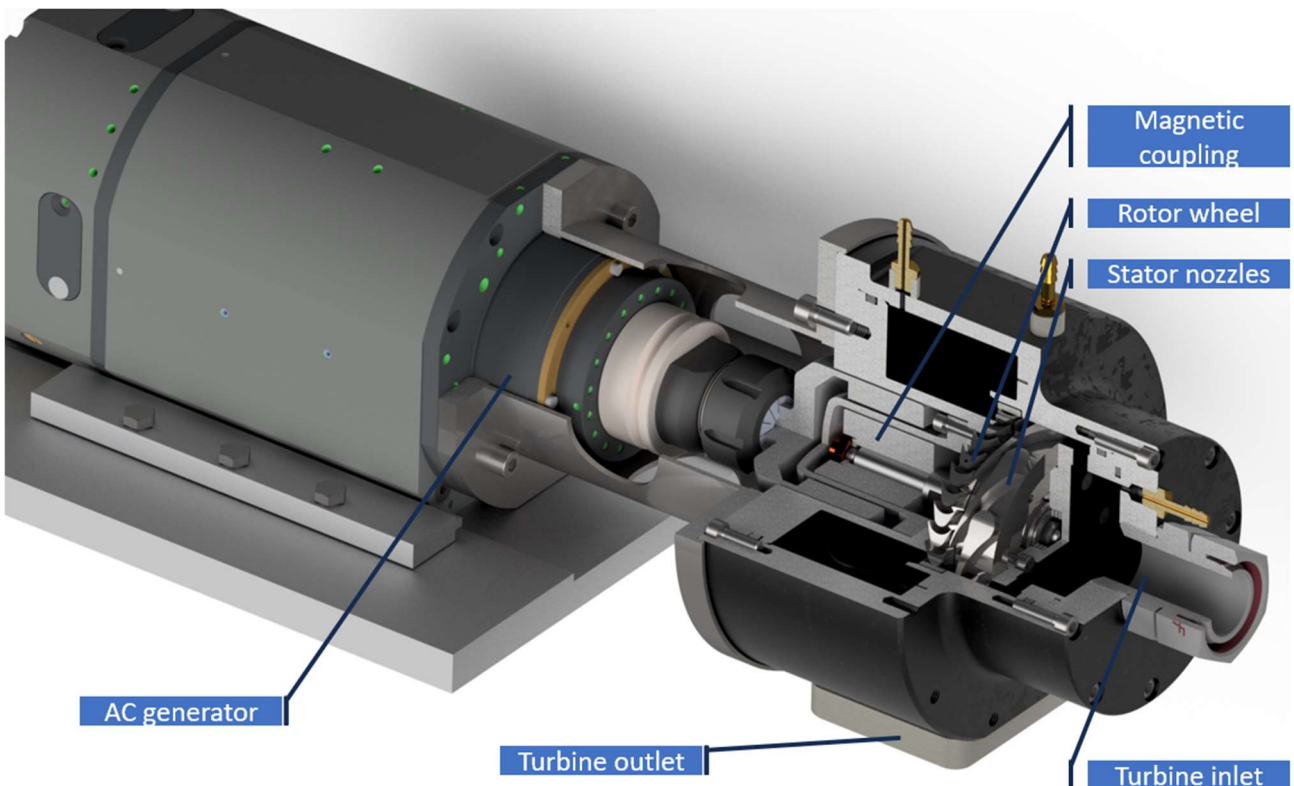


Figure 47. Final mechanical design of the turbine assembly with magnetic coupling and generator v1.

Direct hot-pressing of the stator wheel to the turbine casing needs to be changed to an easier way of locking it in position, as the assembly process could very easily end with damaging the whole turbine. The learning point there for v2 is that only a shroud ring will be hot pressed onto the turbine stator nozzles and this shroud ring will be screwed in position to the turbine casing.

Rotor shroud was radially locked in place by hot pressing it and screwing the shroud to the rotor blades using screw should secure it against axial displacement. However, at higher rotational speeds, the head of the screws snapped, and the shroud axially shifted. Luckily this did not cause any accident but had to be fixed by welding in the screws between the shroud and rotor blades, which proved to be efficient and not too time demanding, so this procedure will be used also for assembly of v2.

Moreover, the connection between the turbine casing and the generator was not sufficiently stiff and cantered, for this reason a second version of the assembly will address this problem. In the axial direction, the whole shaft assembly was significantly shorter than any other axial single stage turbine ever designed for similar boundary condition. This however came with a cost of the magnetic coupling being very hard to reach during assembly and alignment with the generator, which caused several hours of tedious work and a collision before aligning it precisely. The second version will utilize a different approach with a shaft being longer (also to position the centre of gravity of the shaft assembly more to the centre between the bearings), more easily to be dynamically balanced and also with a much easier access to the inner rotor of the magnetic coupling and the sealing canister.

To transfer the torque from the turbine rotor wheel, and transfer the torque to the magnetic coupling, instead of using difficultly balanced feather keys, tapered clamp joints will be used.

3.1.4 Axial MM turbine v2

Finalized modification to the turbine (v2) are presented in Figure 48. Manufacturing of the turbine wheels needs to be done on a 5-axis milling machine, all the other components are either standardised parts or components that can be turned and milled on a standard lathe and a 3-axis milling machine.

Using the FPM O-rings that seal the working environment radially has proved to be functional, but very difficult to (dis)assembly. Therefore an approach with axially sealing O-rings will be used in the future.

Organic vapour inlet to the turbine in the v1 version of the assembly was not optimized with regard to the flow path aerodynamics. This was due to very low speed of the vapour in the high pressure inlet. However despite the low speed in the order of magnitude of 10 m/s, a new approach with more aerodynamically shaped inlet divertor was taken in the version 2 inlet design. The major reason for that is to eliminate any flow separation or recirculation bubble in the root section of the stator nozzle which may result in inducing vortices and secondary losses throughout the operation of the supersonic convergent-divergent nozzle.

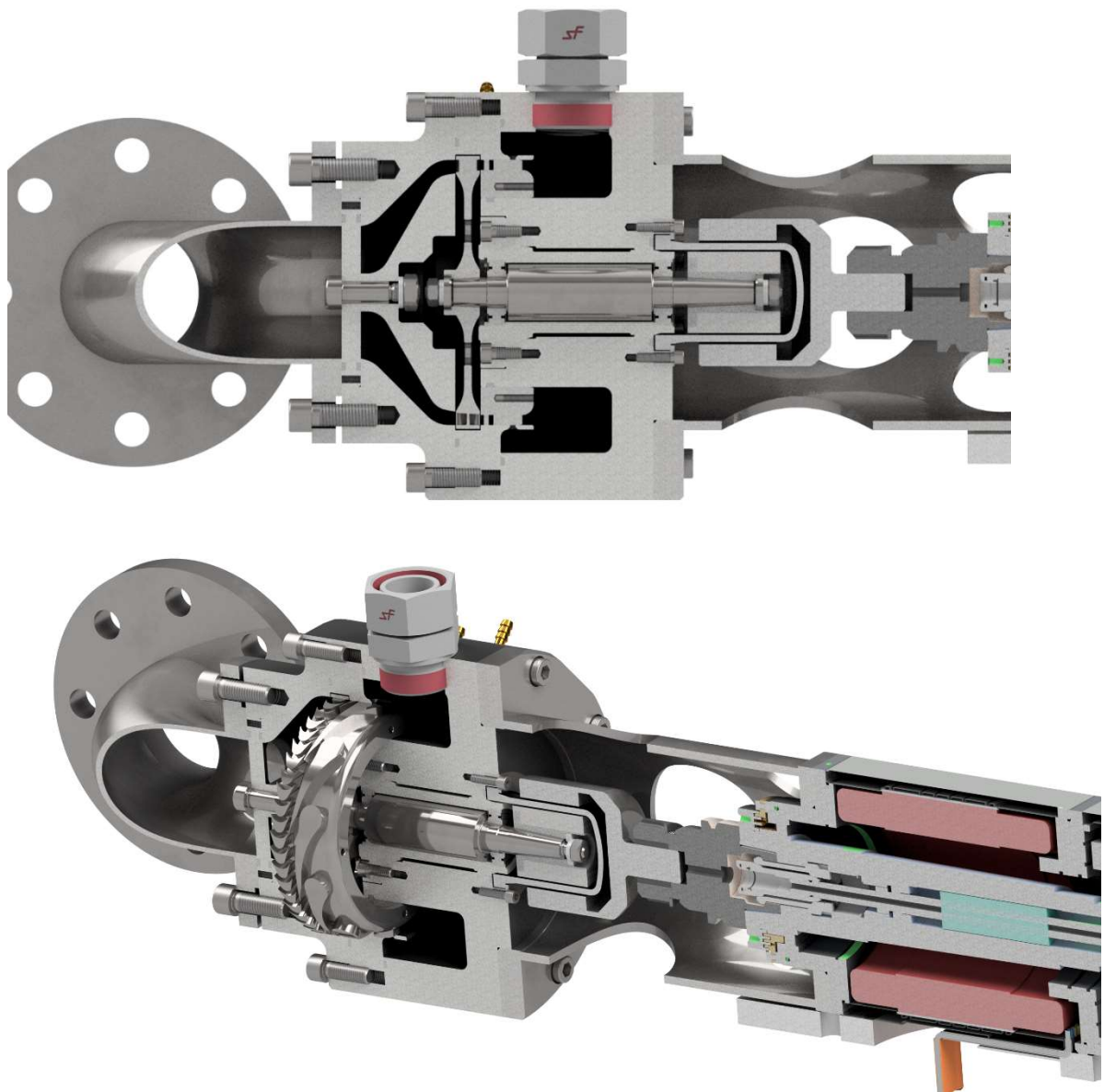


Figure 48. Cross-sectional view to the second version of the MM axial turbine assembly

3.2 Axial isobutane turbine mechanical design, manufacturing and assembly

Figures Figure 49 - Figure 53 illustrate the ORC isobutane turbine followed by technical specifications, turbine interfaces, mechanical and electrical data. The turbine has undergone initial testing with promising results as detailed in the presented and supporting data.

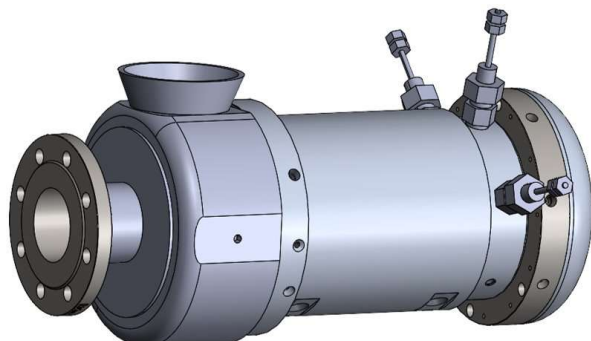


Figure 49. CAD drawing of the casing of the ORC turbine.

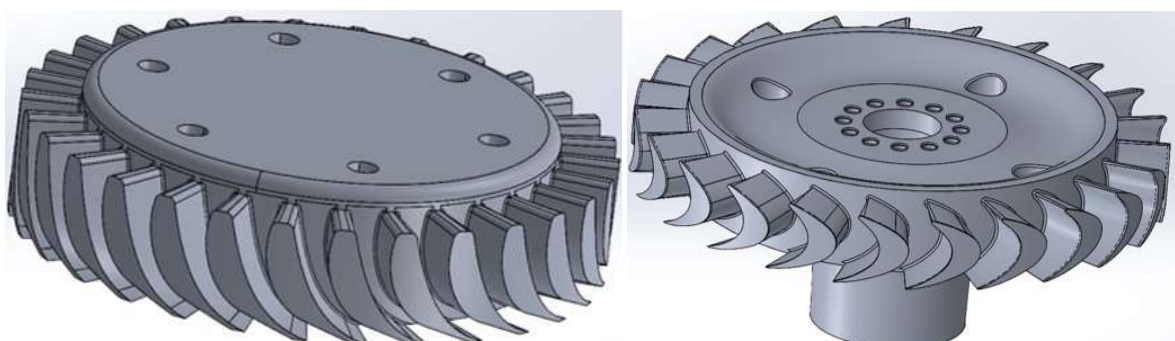


Figure 50. CAD drawings of the stator and rotor of the turbine. Left, the stator blades of the turbine. Right, the rotor blades.



Figure 51. Manufactured and mounted rotor blades (impeller wheel).



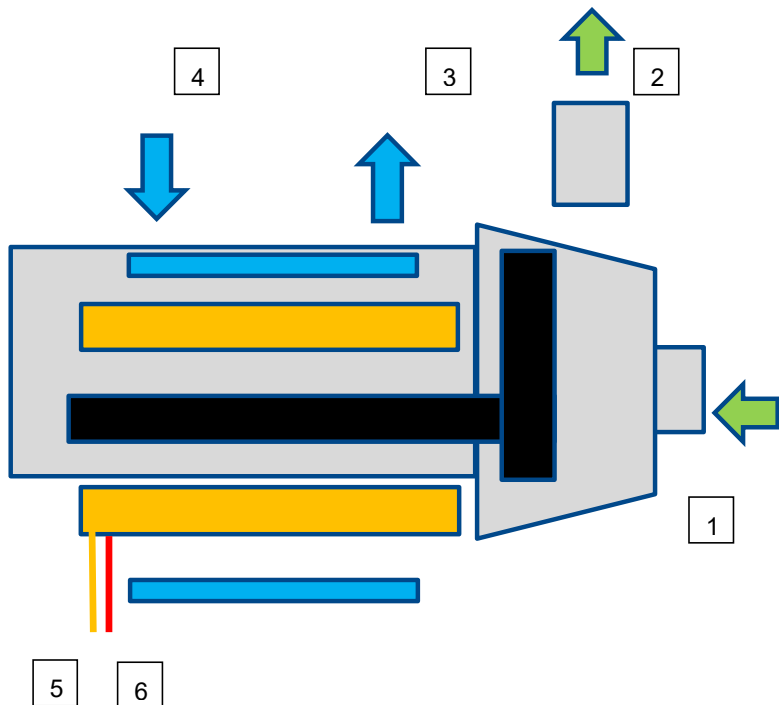
Figure 52. Photo of turbine mounted on the main skid.

Table 13. Technical specifications of the isobutane turbine

Criterion	Values
Input Pressure	4 bara
Output pressure	2 bara
Input temperature	125°C
Rotational speed	17 000 rpm
Lubrication	Grease
Cooling	10°C < Tcooling water < 40°C
Piping connections	DN80 flange input DN125 flange output

T A

Č R



N°	Component
1	Input working fluid (DN80 flange)
2	Output working fluid (DN125 flange)
3	Input cooling fluid (BSPP)
4	Output cooling fluid (BSPP)
5	Power supply cables x 3
6	PT1000 temperature sensors x 2

Figure 53. Isobutane turbine interfaces

Mechanical data

- Maximum dimensions (L x W x H) : 630 x 350 x 265 mm
- Total maximum weight: 80 kg
- Nominal performances: 48 kW, 17 000 rpm, DP = 2 bar, 1.6 kg/s
- Material casing and main components: inox 316L
- Isobutane R600a compatibility: OK
- Pressure range allowed in operation: 2 to 4 bara
- Temperature range allowed in operation: +15 to +125°C
- Flow rate range allowed in operation: 0 to 1,6 kg/s
- Nominal speed: 17 000 rpm

T A

Č R

- Speed variation allowed: YES.
- Speed range allowed in operation: 0-17 000 rpm
- Nominal mechanical power: 48 kW
- Mechanical power range allowed: 0-48 kW

Electrical data

- Voltage range allowed: 0 to 240 VAC
- Nominal voltage: 240 VAC
- Nominal current: <133 A
- Maximum current: 220 A
- Frequency range allowed: 0 to 284Hz (drive 0 to 500Hz)
- Frequency nominal: 284 Hz
- Drive for speed variation: YASKAWA (ref: CIMR-AC4B0208AAA-0064)

3.3 Elektra turbine mechanical design, manufacturing and assembly

The mechanical design of the Elektra turbine uses the nozzles, deflection channels and blades of Version 4. Because of the overall size of the Rotor (outer diameter 255 mm) and the length of the nozzles, the overall outer diameter of the housing is 435 mm. Because of this size, aluminium was used for most of the parts of the turbine, to decrease the overall weight.

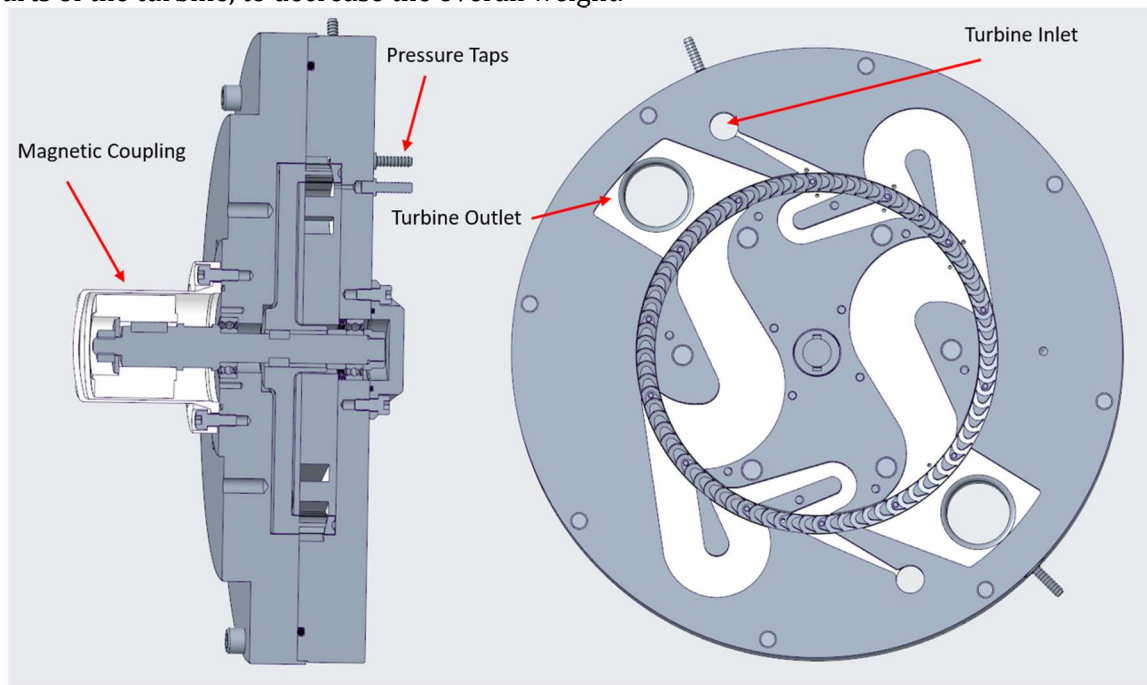


Figure 54. Meridional- (left) and blade to blade cut (right) of the Elektra Turbine.

The inlet and outlet areas of the turbine can be seen in Figure 54 in the blade to blade cut on the right. The inner deflection channels can also be changed to different versions, as the inner disc is interchangeable. The shaft is designed, so that it can directly be connected to the magnetic coupling, as

can be seen in Figure 54 left. The turbine is also designed with 9 different pressure taps, so that the pressure distribution through the turbine can be tracked and compared to the CFD simulations.

First measurements of the Elektra turbine is carried out with pressurized air instead of MM. For these tests, an assembly of the turbine, magnetic coupling, torque measuring shaft and generator were prepared. The assembly of all the parts is shown in Figure 55. These tests should ensure the tightness and the basic functionality of the turbine before it will be installed into the MM test facility.

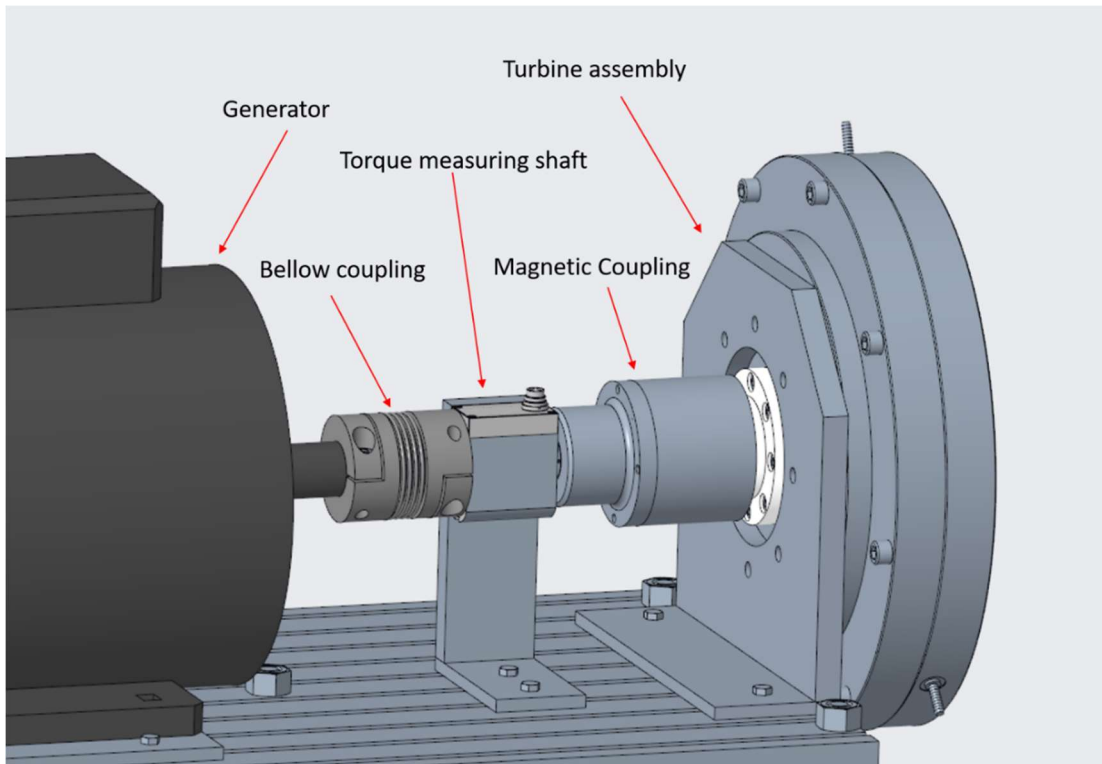


Figure 55. Assembly for air tests of the Elektra turbine.

Aluminium choice of main material has proven to be suitable given the size and weight of the components and the final turbine. Downside is the material softness, making the components prone to scratches and dents. Special attention needed to be paid to co-centricity and alignment, however no suggestion for future improvement of these issues was figured at this point for the Elektra turbine. The turbine was assembled and prepared for air tests and subsequent ORC testing. Figure 56 documents the turbine during its assembly process. The inner Deflection Channels are shown in the top right corner already mounted on one of the two plates of the turbine. On the lower left side of the figure, the outer deflection channels and the two nozzles of the turbine are shown. The lower right part shows the rotor wheel mounted on the shaft. Several recommendations for follow-up designs are then documented in the Commissioning section.



Figure 56. Photos from the assembly of the Elektra turbine.

3.4 RVE mechanical design, manufacturing and assembly

Regarding RVE, the design is largely derived from the existing design for MM fluid with several relatively small, though important aspects. These include mostly the changed operating conditions as pressure, working fluid and dry operation instead of lubricant being present in the working fluid. Therefore, different vane thickness needs to be applied when the pressures are higher. Isobutane and subsequently air working fluids have specific requirements regarding sealing (o rings). And dry operation requires different approach to bearings, where sealed variants need to be employed and long term tests will show if additional lubrication would be needed.

As part of initial works towards intended scale-up, new design of the expander was performed for future manufacturing and testing. The parameters of this expander are in Table 14 and the design is shown in Figure 57.

T A

Č R

Table 14. Parameters of the RVE for the 200 kW_{th} unit.

Stator bore	[mm]	91
Eccentricity	[mm]	6.4
Rotor diameter	[mm]	78
Stator length	[mm]	245
Vanes thickness	[mm]	1.5
Vanes height	[mm]	24.5
Number of chambers	[‐]	8
Expansion ratio	[‐]	3.1
Initial chamber volume	[cm ³]	34.5
Mechanical power output	[kW]	13.15
Expander isentropic efficiency	[‐]	0.518
Vane mass	[g]	70
Nominal rotational speed	[rpm]	3030

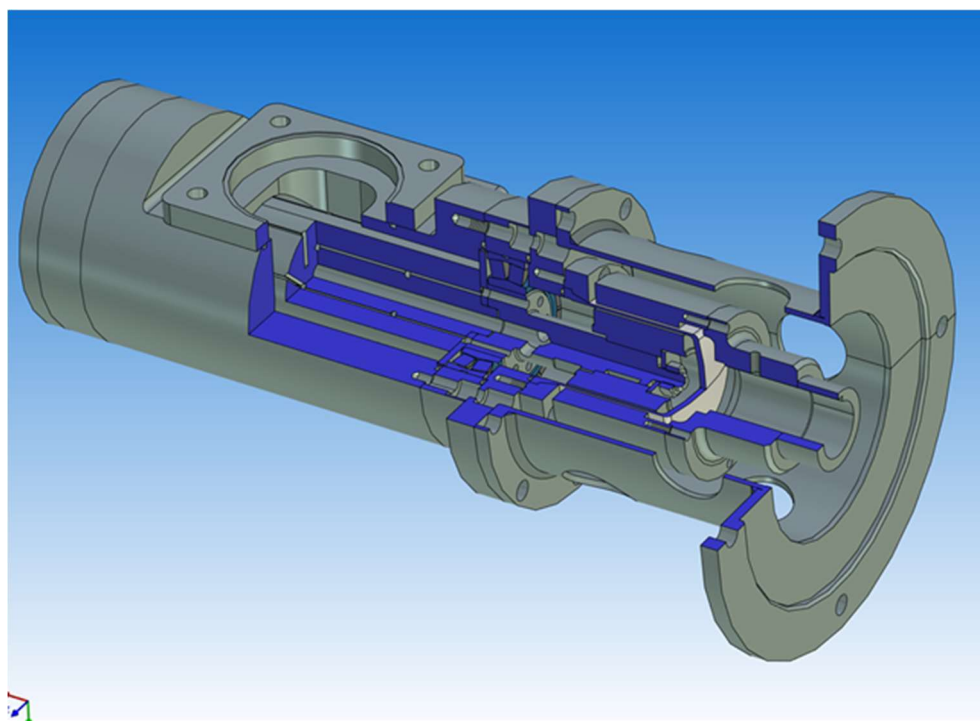


Figure 57. Assembly of upscaled RVE for 200 kW_{th} system.

After finalizing the working fluid of the expander as air and smaller scale, the boundary conditions for which the oilless rotary vane expander is designed are shown in the table Table 15. Owing to the characteristic working principle of positive displacement expansion machines, the expander has a very wide operating range and can also easily operate with other working fluids, as long as certain conditions are met. In contradiction to the previous designs for MM and then isobutane, the system

was re-designed to different boundary conditions and application to meet the changed project objective within the work package concerning RVE design with the goal to test the dry oilless operation of the RVE which enables operation with natural hydrocarbons as working fluids.

Table 15. Boundary conditions for the oilless rotary vane expander final design.

Parameters	Unit	Oilless RVE
Working fluid	-	dry air
Total inlet pressure	bar(a)	10
Total inlet temperature	°C	50
Design volumetric flow rate	l/s	0.82
Static exit pressure	bar(a)	1
Stator diameter	mm	64
Rotor diameter	mm	55
Rotor length	mm	25
Rotational speed, n	rpm	3030
Nominal design expansion efficiency	%	48.2
Nominal design power output	W	900

The Figure 58 below is a pressure-volume (p-V) diagram of the rotary vane expander. It plots pressure in kilopascals (kPa) on the y-axis against volume in cubic millimeters (mm^3) on the x-axis. The curve starts at a high-pressure point, remaining relatively constant as volume decreases marginally, indicative of the filling phase. Then, as the chamber closes, the volume expands and the pressure decreases significantly, showing the expansion phase typical of an RVE. The curve then loops back toward the origin, suggesting the return to the initial state in the cycle. This diagram follows the pressure in a single working chamber, the rotary vane expander totally consists of 6 chambers and 6 sliding vanes. This p-V diagram describes the operation of the machine and helps the engineer better to understand how the machine behaves in each angular displacement of the vane.

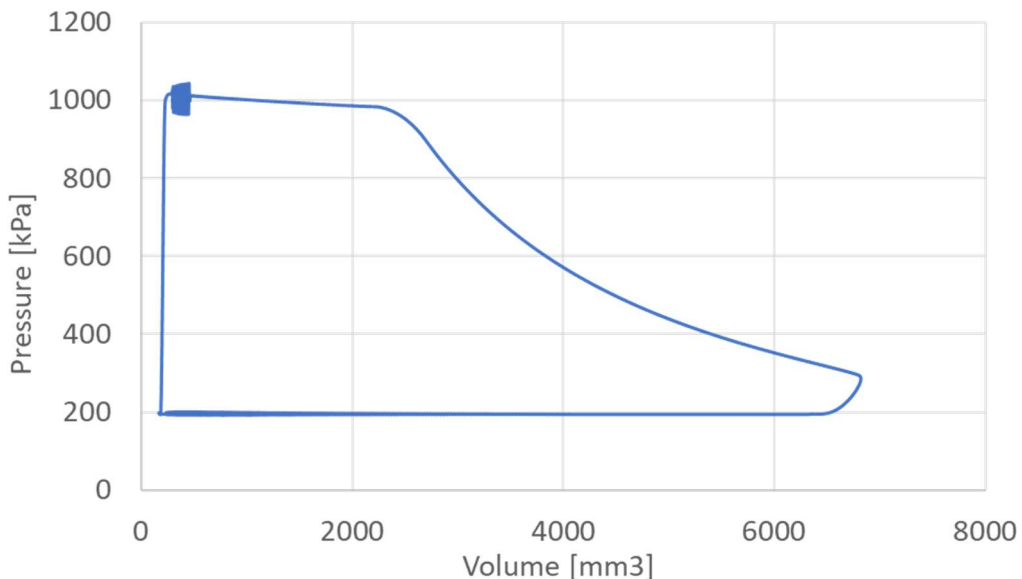


Figure 58. *p-V Diagram of a Rotary Vane Expander Cycle.*

The next Figure 59 depicts the vane reaction force in Newtons (N) as a function of angular displacement in degrees ($^{\circ}$) for a rotary vane expander. The graph features a fluctuating line that peaks and troughs, reflecting the dynamic changes in the force exerted by the vanes during rotation. The force rises to a peak around 45 degrees (after filling of the chamber). It decreases again and shows smaller variations before the cycle repeats. This behaviour is characteristic of the forces experienced by the vanes as they move through different positions during the expander's operation. In displacement around 225° , the vane fully loses reaction force, which is a critical point, because it indicates that a radial leakage along the tip of the vane may occur. The reaction force on the vane exhibits a very dynamic behaviour and thus the coating of the surface must be both very hard and also have low frictional coefficient to be able to operate without lubrication with small friction loss and no surface damage.

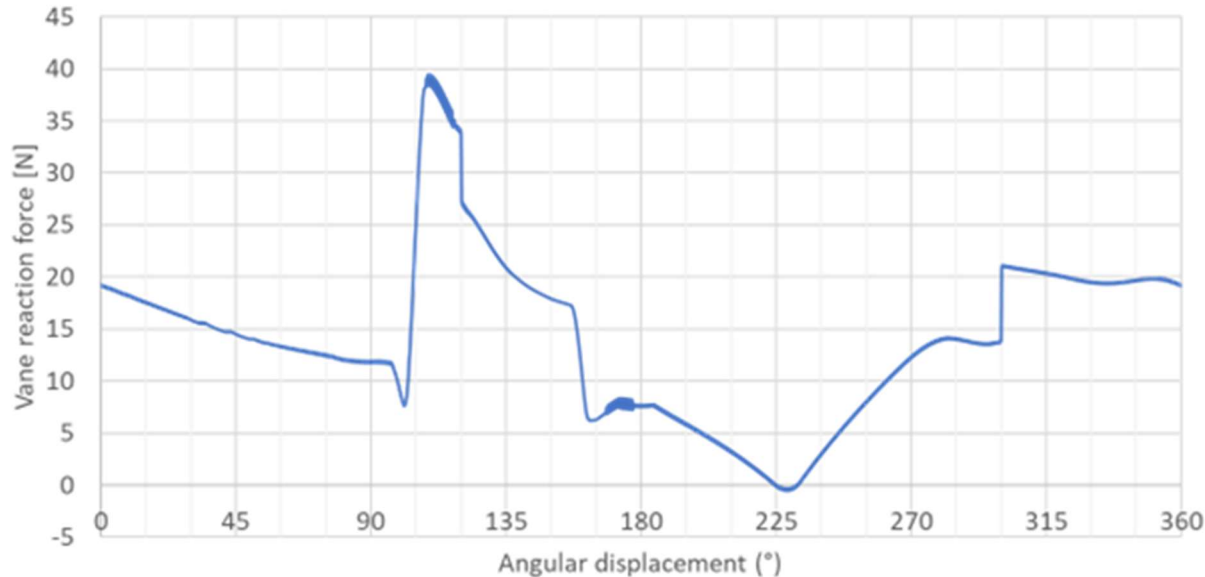


Figure 59. Vane Reaction Force vs. Angular Displacement for a Rotary Vane Expander.

The proposed rotary vane expander is shown in final design in Figure 60, manufactured components are in Figure 61 and final assembly is in Figure 62. It distinguishes itself through its capacity to maintain operational efficiency across a diverse range of conditions without reliance on active lubrication. The integration of specialized sliding coatings on the vane surfaces negates the need for a dedicated lubrication circuit, which streamlines the expander's design and reduces both the initial investment and the ongoing maintenance costs. This also eliminates contamination risks associated with lubricant leakage, which is especially beneficial in applications where purity of the working fluid is critical.

From an engineering perspective, the exclusion of a lubrication system reduces the complexity of the expander, and if proven to function as intended, may enhance reliability and decreasing the likelihood of mechanical failure. The sliding coatings are selected for their low friction and wear-resistant properties, contributing to the longevity of the expander and consistent performance over time.

The incorporation of a magnetic coupling is a strategic choice, allowing the expander to function safely with flammable or environmentally sensitive working fluids. This coupling method provides a hermetic seal, which prevents any leakages and potential exposure of the working fluid to the environment, ensuring compliance with health, safety, and environmental regulations. This feature is particularly advantageous when the expander is used in sensitive environments where leakage could have severe consequences.

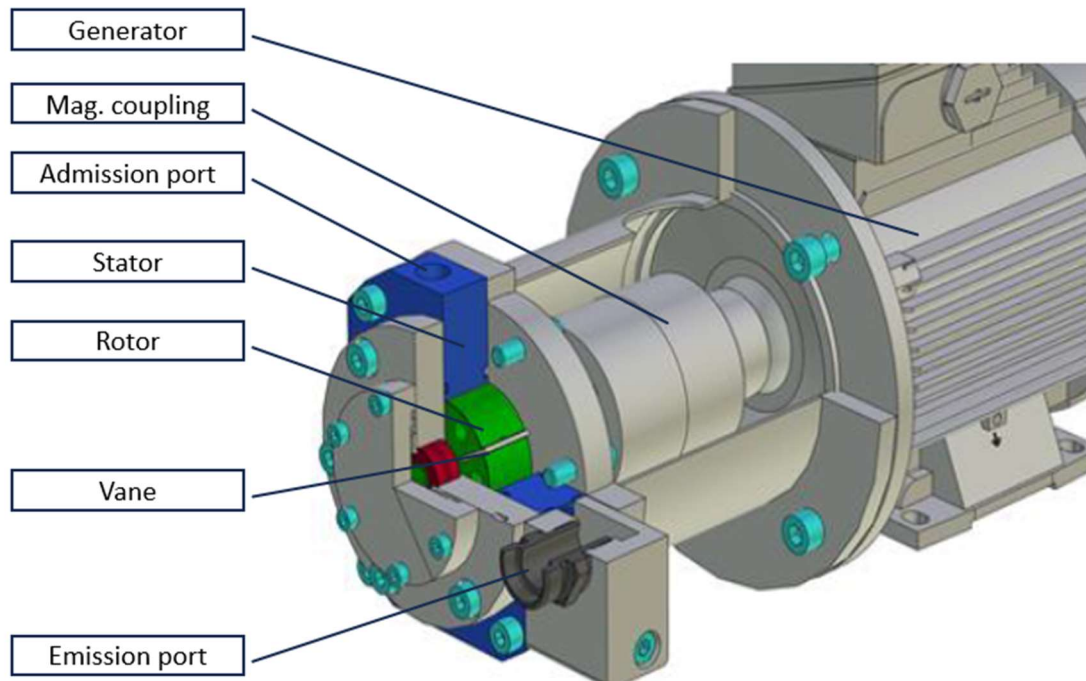


Figure 60. Annotated Cross-Section of a Rotary Vane Expander Assembly.



Figure 61. Air RVE assembly before parts assembled together.



Figure 62. Air RVE assembly after completion.

3.5 Rotordynamics and stress analyses

3.5.1 Axial turbine

These works started with preparation works and a sensitivity analysis of various shaft-bearings-rotor-generator (or magnetic coupling) configurations to later minimize the risk of resonance frequency issues. Within these works were performed initial studies of two shaft configurations (Figure 63), one with single shaft two bearing configuration and overhanging turbine wheel, where generator is basically in the working fluid hermetic area and one with magnetic coupling between working fluid region and generator, where the magnetic coupling allows a hermetic separation of generator shaft and turbine wheel shaft while ensuring torque transfer. Finite elements methods was used to analyse the natural frequencies and natural oscillation of the shafts, see. Figure 64 for the version with generator inside the turbine assembly and with the magnetic coupling and generator outside. The overall results are to be finalized yet, but the preliminary results so far indicate, that the natural frequencies are well below or above the nominal rotational speed of the machine, so the risk of the torsion oscillation is minimal.

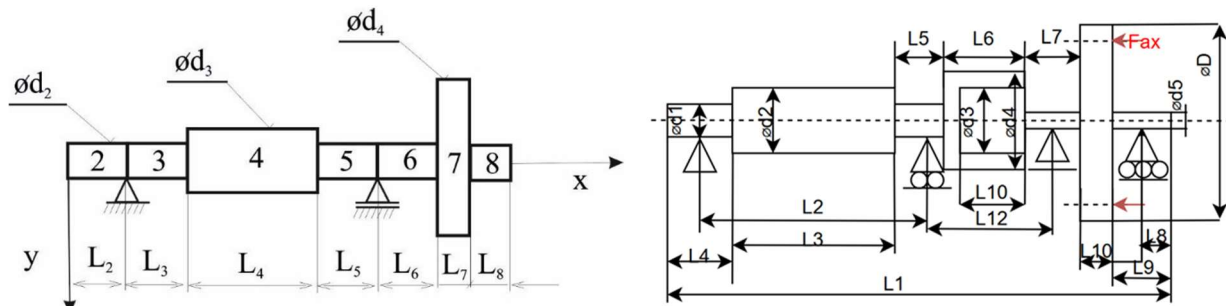


Figure 63. Two preliminarily investigated turbine shaft configurations, direct connection (left) and with magnetic coupling between working fluid region and generator (right).

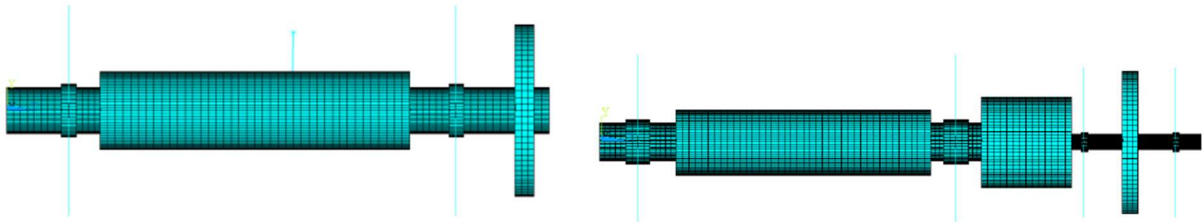


Figure 64. Two preliminarily investigated turbine shaft configurations, the finite elements models, direct connection (left) and with magnetic coupling between working fluid region and generator (right).

Following the finalization of the mechanical design, the aim was to investigate the basic dynamic characteristics of the final modification of the turboexpander assembly for ORC unit. An essential prerequisite for achieving this goal is to build suitable simplified mathematical models describing the analysed system so that it is possible to efficiently evaluate the modal properties of the system without the need for geometric reconfiguration of the system in computational tools based on the FEM method. With respect to the required operating range of the rotor system ($n = 2000 - 40000 \text{ min}^{-1}$), the primary objective of the analysis is to determine the resonance bands of the system and then to evaluate the achieved values of the system deflections at a defined degree of unbalance. Summary of the investigations is below.

The geometrical configuration of the analysed system with the generator mounted on the turbine shaft is shown in Figure 65.

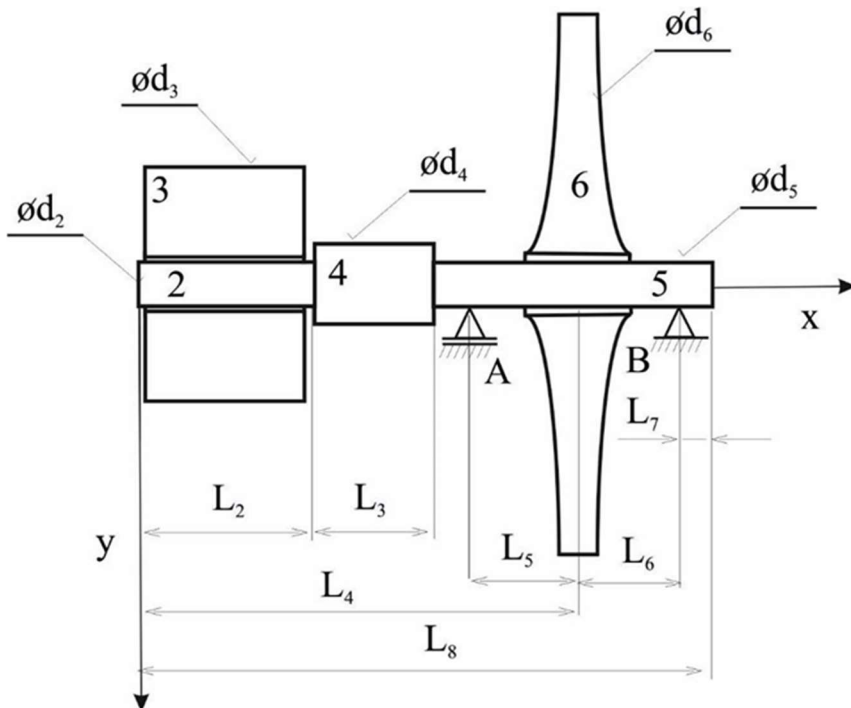


Figure 65. Geometric configuration of the system.

The following calculation modes are considered for the system according to Figure 65:

- Determination of the natural frequencies of the system for the nominal value of bearing stiffness
- Determination of the natural frequencies of the system for increased bearing stiffness
- Analysis of system deformation for speed mode $n = 40000 \text{ [min}^{-1}\text{]}$ for nominal bearing stiffness value for defined unbalance G2.5 according to ISO 1940
- Analysis of system deformation for speed mode $n = 40000 \text{ [min}^{-1}\text{]}$ for nominal value of bearing stiffness for defined unbalance G2.5 according to ISO 1940 considering axial force on turbine wheel $F_{ax} = 18.8 \text{ [N]}$

A computational model based on the principles of continuum mechanics is developed to quickly evaluate the resonance intervals of the system. Simplified models of the system are used. The model is based on the wave equation for longitudinal oscillations and uses the method of separation of variables to derive a relation for the deformation of the continuum. This relation is expressed as the product of two functions, one that describes the spatial variation of the deformation and another that describes the temporal variation. The boundary conditions of the system are used to determine the constants A and B, which determine the amplitude and phase of the oscillations. The natural frequencies of the system can then be calculated by substituting the expression for the deformation into the boundary conditions and solving for the frequencies that result in a non-trivial solution. The model is further extended to include bending oscillations and circular oscillations, which are described by different wave equations that take into account the effects of displacement force, rotational inertia, and sectional moment squared. The natural frequencies of the system can be calculated by substituting the expressions for the

deformation into the equations of equilibrium and solving for the frequencies that result in a non-trivial solution.

Resulting first three natural frequencies of axial oscillations are 12950, 30975, 66937 Hz, much more than 666 Hz considered as the upper theoretical speed limit. Bending vibrations natural frequencies of the system are then in case of rigid housing 1452,13591,18885,37540, . . . , again much higher than 666 Hz. The situation is however different when bearing stiffness is considered. Bearing stiffness characteristic can be obtained as a function of the load force. For the considered case the bearing stiffness characteristic is in Figure 66. Sensitivity study of the effect of fit compliance on natural frequency of the system of the bending oscillations are then in

Table 16.

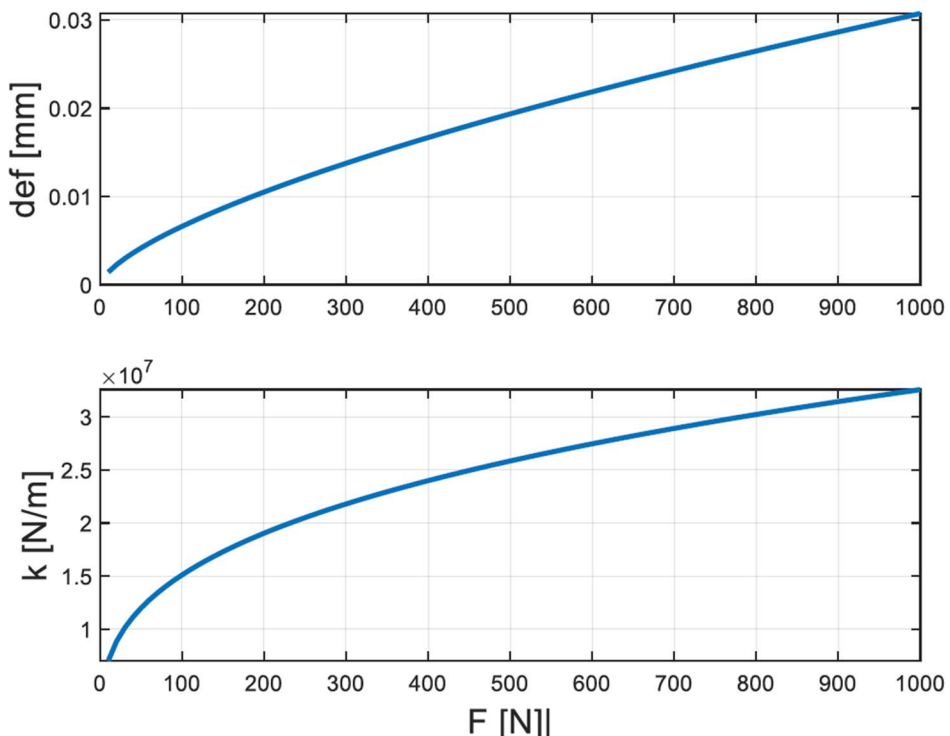


Figure 66. Bearing stiffness characteristics.

Table 16. Natural frequency of the system in bending oscillations.

$kA=kB$ [N/m]	F_1 [Hz]	F_2 [Hz]	F_3 [Hz]
1e7	883	13793	29488
2e7	1062	13418	29831
3e7	1162	12805	30153
5e7	1256	11097	30736

The equation describing the circular oscillations of the continuum can be solved assuming a simultaneous precession $\dot{\psi} = \dot{\varphi}$, $\ddot{\psi} = 0$, derive according to Figure 67. For a simplified calculation of the circular oscillations of the system, the force method can be used assuming a compliant but immovable shaft. The matrix of causal factors can be derived from the boundary conditions of the individual segments of the solved system. Natural frequency of the circular oscillations are then in Table 17. In the case of a variable cross-section material shaft loaded with discs, it is necessary to construct the wave equation of the circular vibrations of the compliant shaft from the equilibrium conditions of the differential segment of the shaft. Then it is necessary to define the wave equations in the individual segments of the system. Using the corresponding boundary conditions frequency equation can be derived from which the values of the natural frequencies of the system for the circular oscillations are derived and presented in

Table 18.

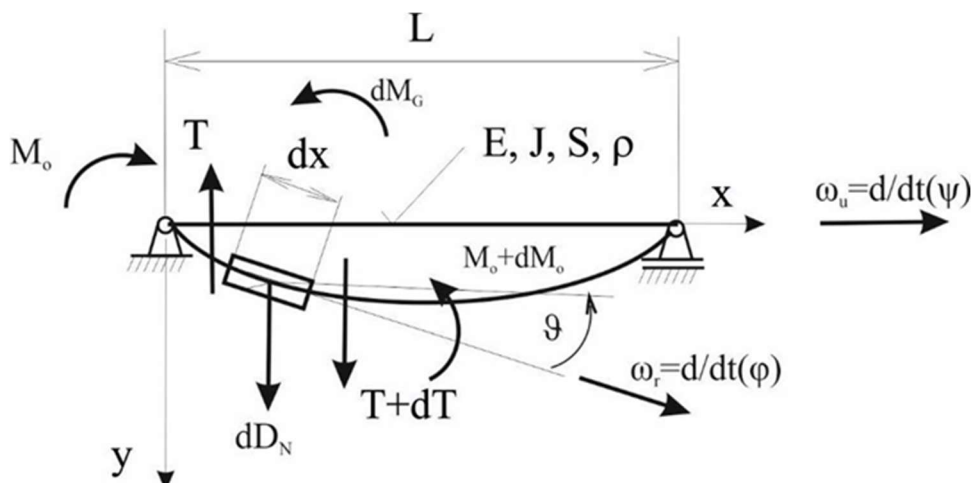


Figure 67. Circular oscillations.

Table 17. Natural frequency of the circular oscillations – intangible shaft.

$d_1=d_2$ [mm]	F_1 [Hz]	F_2 [Hz]	F_3 [Hz]
10	371	1391	2343
12	534	2003	4952
14	727	2727	6741
16	950	3562	8804

Table 18. Natural frequency of the circular oscillations – tangible shaft, bearing stiffness.

$kA=kB$ [N/m]	F_1 [Hz]	F_2 [Hz]

T A

Č R

1e7	237	937
2e7	285	1256
3e7	310	1482
5e7	337	1803
rigid	404	3643

A computational model based on finite element method (FEM) was constructed to analyze the system, which included radial and axial bearing stiffness. The model was evaluated for different values of bearing stiffness and the natural frequencies of the system were obtained. Natural frequency of the system are summarized in Table 19 and graphically in Figure 68.

Table 19. Natural frequency of the system according to Figure 68.

	1e7 [N/m]	2e7 [N/m]	3e7 [N/m]	5e7 [N/m]
F1 [Hz]	131 circ	183 circ	223 circ	283 circ
F2 [Hz]	325 bend	414 bend	467 bend	529 bend
F3 [Hz]	326 bend	415 bend	468 bend	530 bend
F4 [Hz]	878 bend	1134 bend	1223 bend	1277 bend
F5 [Hz]	887 bend	1141 bend	1224 bend	1278 bend
F6 [Hz]	1310 bend	1426 bend	1606 bend	1751 circ
F7 [Hz]	1316 bend	1428 bend	1618 bend	1953 bend
F8 [Hz]	1748. circ	1749 circ	1750 circ	1972 bend
F9 [Hz]	1836 circ	1938 circ	1970 circ	2014 circ
F10 [Hz]	2854.9 wheel	2854.9 wheel	2854.9 wheel	2854.9 wheel

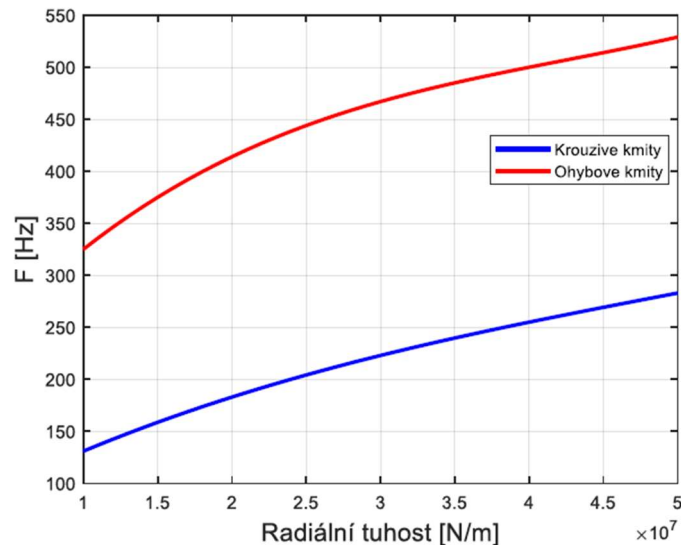


Figure 68. First natural frequency values for circular (blue) and bending (red) oscillations.

The FEM model was also used to evaluate the deformation of the rotor system under different degrees of unbalance (Table 20), which were considered in three planes: the plane of the center of gravity of the coupling magnets, the plane of the center of gravity of the system, and the plane of the center of gravity of the wheel. Furthermore, cases with and without axial force were considered. It was found that the deformation of the rotor system increases with the degree of unbalance and the highest deformation occurs in the plane of the center of gravity of the wheel. Reaction force has very small positive effect.

Table 20. Deformation values of the unbalanced system.

n [min ⁻¹] 40000	Unbalance in the plane of centre of gravity of the coupling magnets def [m]	Unbalance in the plane of the centre of gravity of the system	Unbalance in the plane of the centre of gravity of the orbit	Rx, Ry, Rz [N]
No axial forces	0.313e-4	0.307e-4	0.303e-4	0; 0.024; 10.0
with axial force	0.311e-4	0.306e-4	0.302e-4	18.8; 0.024; 10.0
Unbalanced system: 0.299e-4 [m]				

The analyses performed show that the considered geometrical configuration of the turboexpander of the ORC unit is tuned superresonantly, but with sufficient distance of the resonance peaks from the operating speed $n = 28000$ [min⁻¹]. The values of the maximum deflections for $n = 40000$ [min⁻¹] for nominal bearing stiffness values are about 31 [μm].

Regardless the above analysis, for the v1 axial impulse supersonic MM turbine, two unsuccessful attempts while commissioning have proven that the turbine cannot achieve speeds higher than 18000 rpm without excessive vibrations. The experiment's failure is caused by vibrations of the shaft free end with the inner rotor of the magnetic coupling and subsequently direct contact of this rotor part with the coupling canister, which normally separates the working fluid from the surrounding atmosphere. In the case of testing with compressed air and in a motor mode, only damage to the canister was caused. On the other hand, this defect would have had serious consequences under operating conditions with siloxane vapour.

Natural frequencies of the rotor-shaft assembly were investigated using a Campbell diagram in Figure 69 below. This diagram represents a crucial analysis tool for the stability assessment of an axial impulse single-stage supersonic turbine, designed for an Organic Rankine Cycle (ORC) power system. The diagram plots the turbine's natural frequencies against its rotational speed, offering insights into the vibrational behaviour under operational conditions.

The graph delineates various dashed lines, each corresponding to a discrete vibrational mode of the turbine—specifically, Modes 1 through 5. These modes are intrinsic to the dynamic characteristics of the turbine and are indicative of the potential resonant frequencies as the turbine operates across a spectrum of speeds.

A solid blue line, labelled "Start-up characteristics," illustrates the relationship between the rotational speed of the turbine and the excitation frequency during the start-up phase. This characteristic line intersects with the modal lines at several points, which are of particular interest as they represent the critical speeds at which the excitation frequency coincides with the natural frequency of a mode, potentially inducing resonance.

T A Č R

Of special note on the diagram is the marked "Critical speed (rpm) 13 901," identified by a red triangle. This critical speed is a point of resonance where the operational frequency intersects with one of the turbine's natural frequencies during the start-up phase. Resonance at this intersection is a phenomenon that warrants attention due to the potential for inducing significant vibrational stress on the turbine structure, which could lead to premature wear or failure. The Campbell diagram serves as a predictive tool, enabling the design team to engineer safeguards against resonance-induced damages in the turbine's operational life. It is an essential component of the technical documentation that underpins the safe and efficient operation of the turbine within the specified ORC power system.

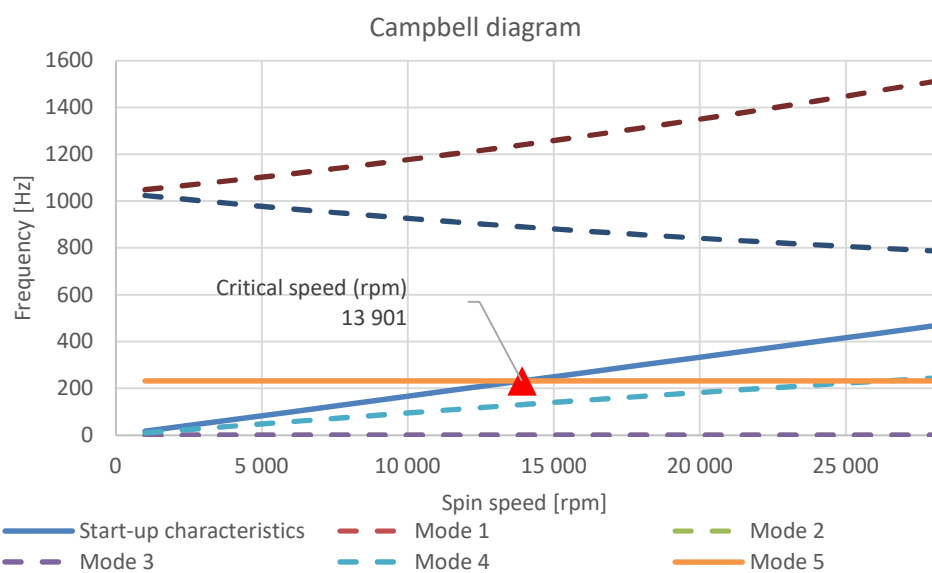


Figure 69. Campbell diagram of the axial turbine, identifying the potentially critical speed for resonance operation, v1 MM turbine.

The modal analysis with the FEM method showed that the turbine is exposed to resonance frequency at speeds around 14000 rpm. A collaboration was established with a company (Vibro stroje s.r.o.) dealing with rotor dynamics and vibration measurements to improve the original assembly. After testing and vibration on-site measurements, it was recommended not using the turbine at the designed 24 000 rpm and suggested the following arrangements to the new concept:

- 1) The rotor's centre of gravity should be located exactly between the bearings.
- 2) Use of thicker shaft as a compromise of speed loss (higher diameter means higher circumferential speeds in bearings).
- 3) Design a larger axial distance between the bearings to eliminate shaft displacement caused by tolerances in the bearings.
- 4) Improvement of the shaft-hub connection – use of tapered seats or press fit instead of the keyed joint
- 5) Optimize design for rotor-dynamic balancing and future collaboration.
- 6) Improve the stiffness of the assembly and the support.

All these points are taken into account in the new version (v2) of the turbine.

With regard to rotordynamics, it is ultimately the main reason why the v2 MM axial turbine is being redesigned, a comparison of centre of gravity and other basic dimensions is shown in Figure 70 below.

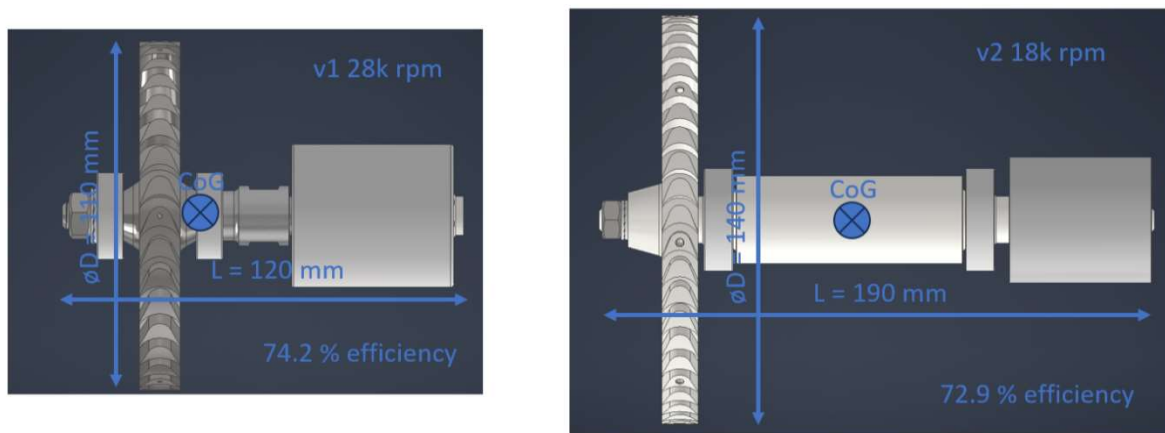


Figure 70. Comparison of the basic dimensions for the v1 and v2 shaft assembly (CoG = centre of gravity).

Regarding the dynamic balancing of the as-manufactured and assembled turbine wheels, Figure 71 documents the extent of material subtraction from the balancing process.



Figure 71. Rotors of the axial MM turbine after dynamic balancing.

3.5.2 Elektra turbine

For the mechanical integrity of the turbine, rotordynamics, maximum displacement and stresses have been investigated also for Elektra turbine. Figure 72 shows the displacement and stresses of the turbine at 3000 rpm (design rotational speed) and 200 °C. The temperature was chosen, as the Impeller could heat up to about 200°C. Maximum displacement was at 0.0224 mm and maximum stress at 13.72 MPa. As for the space between the rotor and the housing of the turbine and the mechanical integrity of the wheel, no difficulties are expected by these results. As for the modal analysis in Figure 73., none of the modes is near the rotational speed of the turbine in its design point and all of them lie in higher rotational speeds, thus ensuring safe turbine operation.

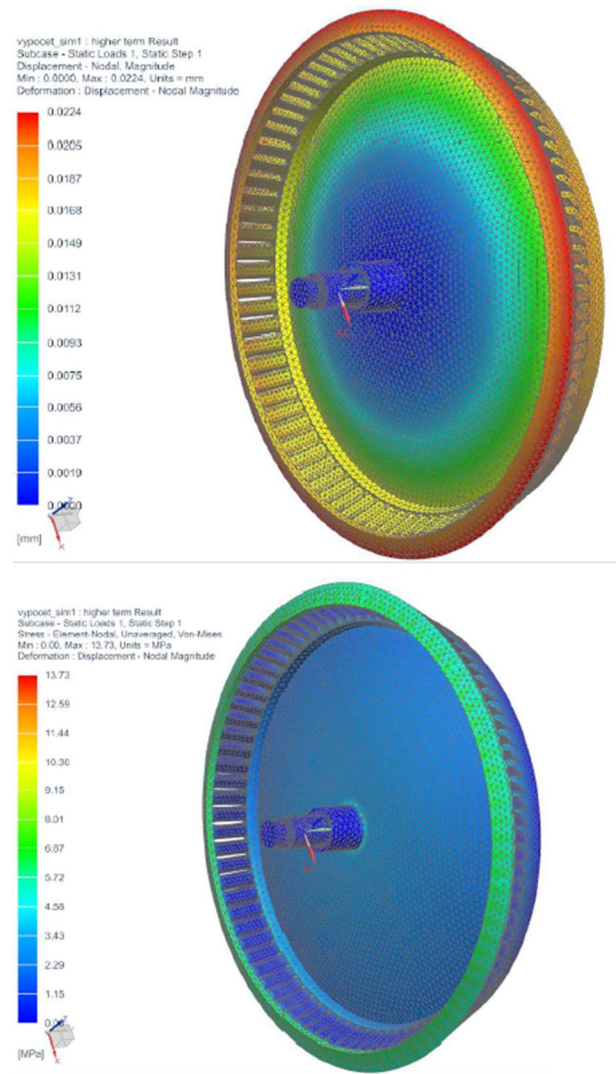


Figure 72. Displacement and stresses for the Elektra turbine at 3000 rpm and 200 °C.

Modal analysis
3000 rpm = 50 Hz

Results:

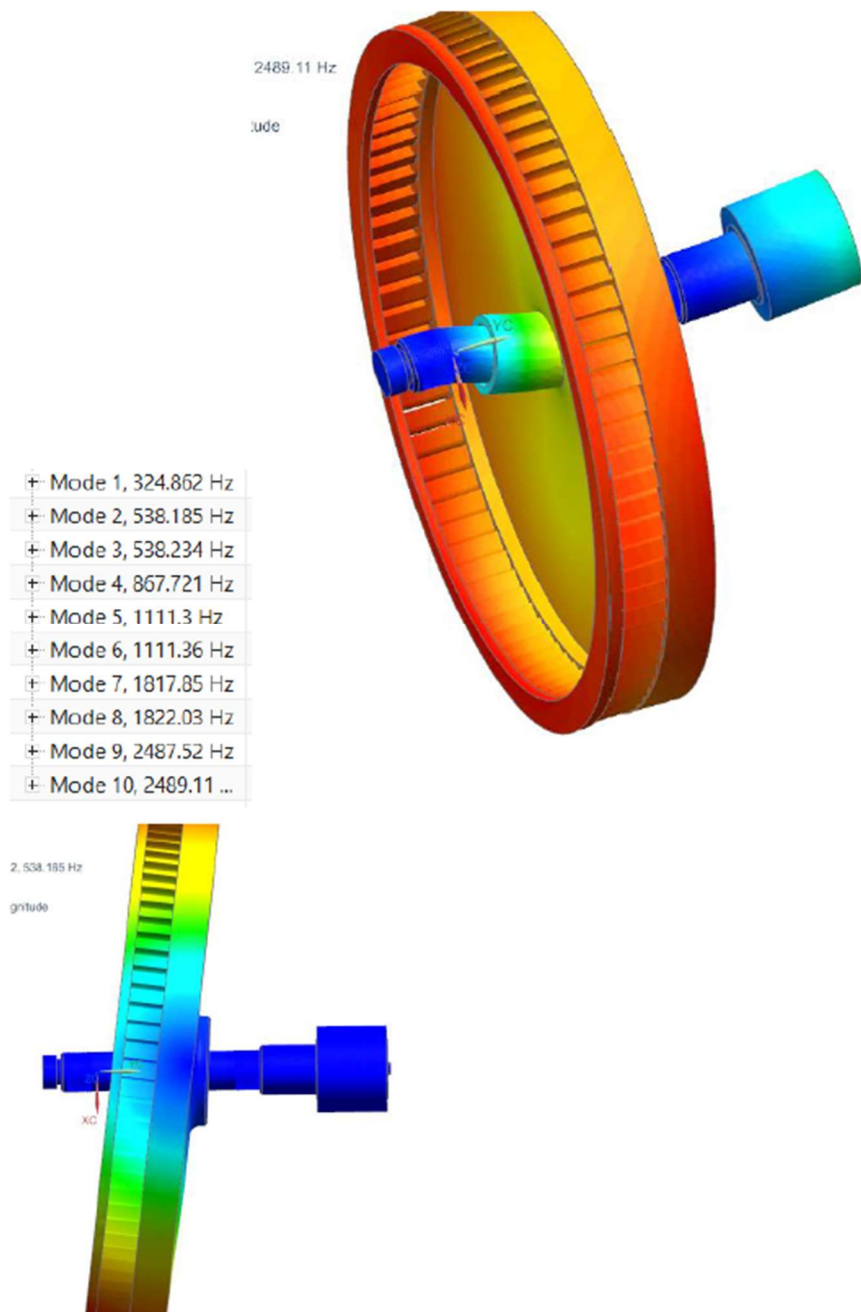


Figure 73. Modal analysis of the Elektra turbine.

3.6 Manufacturing details

First, 3D prints were made to assist also backwards to design, especially verifying possibility to assemble to entire systems and avoid design errors. First CAD models used to get preliminary manufacturing offers from commercial CNC manufacturers and 3D printing companies. At the same time was performed preliminary analysis of 3D printing possibilities, plastic 3D prints (Figure 74) are used primarily to build models on which one can see clearly the flow paths and use it to better visualize the nature of the flow for instance during the CFD modelling.



Figure 74. Example of 3D printed models of the flow components.

Final CAD models and manufacturing documentation was then again used to get offers from commercial CNC manufacturers, with whom there was furthermore intensive discussion and feedback to modify the design. Final manufactured components of the axial and Elektra turbine are in Figure 75 and Figure 76 below.



Figure 75. Manufactured components of the axial turbine.



Figure 76. Manufactured components of the Elektra turbine.

During the preliminary assembly procedures were identified several complications regarding assemble-ability, which resulted in design of auxiliary tools and specific procedures. An example is insertion of the stator blades wheel into the casing, pressed joint, where angle for bolts needs to be identical at three components. This is valuable feedback for future designs.

3.7 Power output

Managing the power output and control of the expander is an essential and integral part of most of the applications of any expanders. There are basically two main options:

- Asynchronous generator near 3000 rpm
- For high-speed generator

The first option is feasible for low-speed expanders as the RVE, which is specifically designed to work at 3000 rpm. As such it can be even directly coupled to the 3-phase grid. In order to actively control the speed, a (reversible) variable frequency drive (VFD) which can work from a common DC bus to which is connected a recuperation unit (active front end, AFE) can be employed, as seen in Figure 77 below for a whole ORC unit.

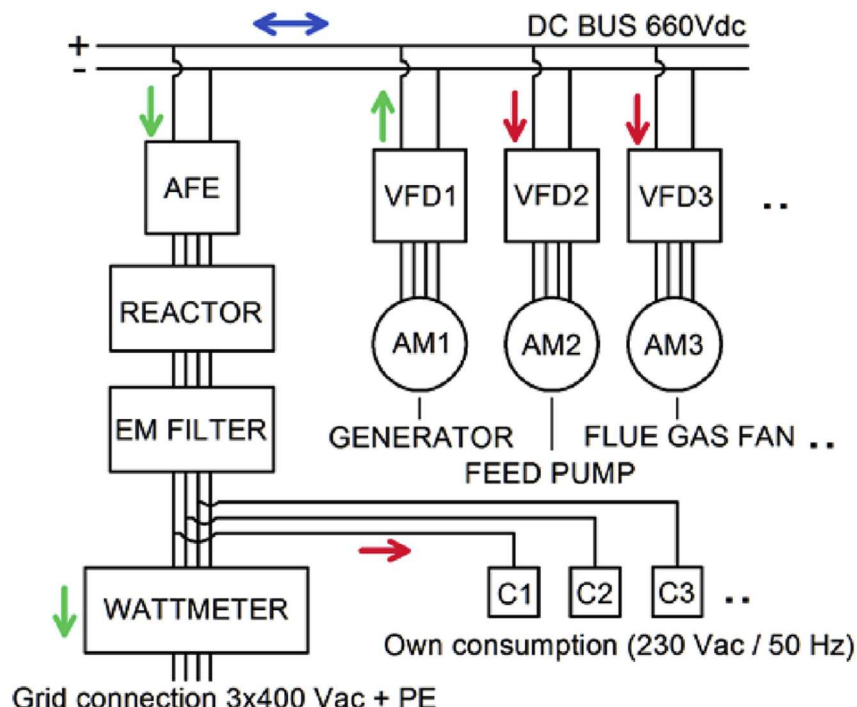


Figure 77. Electrical configuration with VFD and AFE.

Employing a 50 Hz speed asynchronous motor as a generator has been considered also for the turbine, which will operate at speeds around dozens thousand rpm. For that, analysis and conceptual design of a suitable single stage reduction gear between a small turbine blade wheel and a generator, with an expected ratio between 1:8 and 1:12 has been performed. A simple 2k+r planetary gearbox is offered as the optimum type of transmission, with which the desired gear ratio can be achieved, while being dimensionally compact and achieving high efficiency of over 97%. In the case of the 2k+r gearing, to achieve the highest possible gear ratio, the variant is chosen where the gearing is implemented by stopping the crown wheel (3), and for the reduction to slow, the input is on the central wheel (1) and the output is on the carrier (U) - see Figure 78 below.

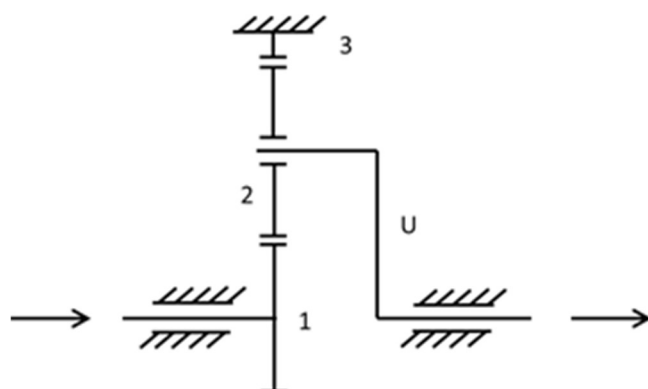


Figure 78. Schematic representation of a 2k+r planetary gearbox.

Manufacturers of planetary gears for industry were considered and contacted for reusing of mass-produced products. This included automotive planetary gears as spare parts or planetary reduction used in the electric starter of engines. Lastly among the geared solutions was briefly considered so-called Garrard friction gear (Figure 79 below). The special configuration of the individual shafts and the main gear eliminates the load on the bearings, thus reducing their friction and significantly improving the overall efficiency, which according to available information is around 98% (but this would have to be experimentally verified). The reduction gear consists of a driven small wheel 1 on the input shaft, a driven wheel 2 on the output shaft and an auxiliary wheel 3 to eliminate reactions. All these gears are located on one straight line and are pushed into the auxiliary crown gear 4. Missing verified references would however require a separate research and development in this aspect.

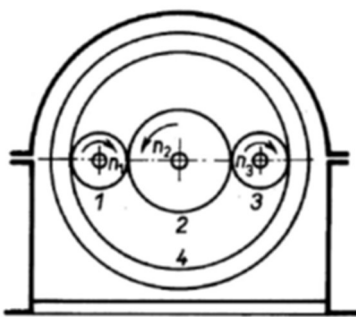


Figure 79. Schematic representation of a Garrard friction gear.

Resulting limited availability of solutions (commercial offers), requirement of custom high cost or development demanding systems (reuse of automotive wheels with custom casing or Garrard gear) or low efficiency (starter gears) pointed this branch of considered solutions as rather unfeasible. Note that for the geared solutions, the gear would most likely need to be also in the hermetic area with the working fluid and on the low-speed shaft would be present a magnetic coupling.

The high-speed generator consideration comes with also several electro-mechanical options. The first is use of the generator integrated on a single shaft with the turbine wheel, within the hermetic area of the working fluid. As such, again it requires rather extensive development and/or know-how. This solution is however across the industry considered as a standard and here will be taken as a baseline.

Regarding electrical output, the VFD+AFE configuration can be employed also for high-speed generator under the condition, that the reversible VFD and given generator can operate at given voltage and frequencies. Therefore, the solution installed in the EXPAND test rig considers specifically this configuration with frequency by default up to 400 Hz, on demand optionally up to 1000 Hz (24 000 – 60 000 rpm).

Alternative and possibly cheaper option has been considered with configuration according to Figure 80. Instead of a VFD a simple rectifier would be employed with controlled DC/DC conversion (buck-boost) to the DC bus with a small battery as a buffer. Electricity from this battery would be then supplied to the grid by market-existing inverters (for PV, wind microturbines). Even though the components generally exist, the only issue is currently seen in the control of the inverter as the PV inverters are typically having inbuilt control algorithms fitted for standardized domestic or PV plant applications and do not easily allow external control of required power output. Suitable option could be an inverter from battery

electricity storage systems, however they on the other hand are rarely offered as a standalone product with mass production. Second option in the Figure 80 with direct use of the PV inverter shows preliminarily unsuitable compatibility between the MPPT trackers designed for PV and actual dynamic characteristics of a turbine.

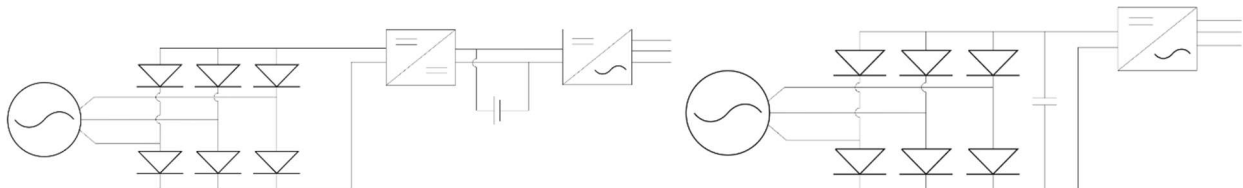


Figure 80. Electronic conceptual circuit diagram of the electrical connection with commercial PV (battery enabled) inverter and directly with PV inverter.

Lastly, for small scale flexible experiments is considered an option with electricity conversion to heat and its dissipation. A configuration is according to the Figure 81, with first rectification and then electricity conversion to heat in transistors switched in a linear region. Advantage of this approach is the possibility to configure the system to a wide range of parameters and precise measurement and control in the whole range (speed, voltage, currents). The team at CTU has a good experience with such system from previous activities, however a different approach is being prepared for even better modularity, reliability, and controllability. Previously all transistors were controlled by a same signal, newly each transistor would have a dedicated controlling processor, temperature measurement (for protection) and these separate units would be communicating together by data communication.

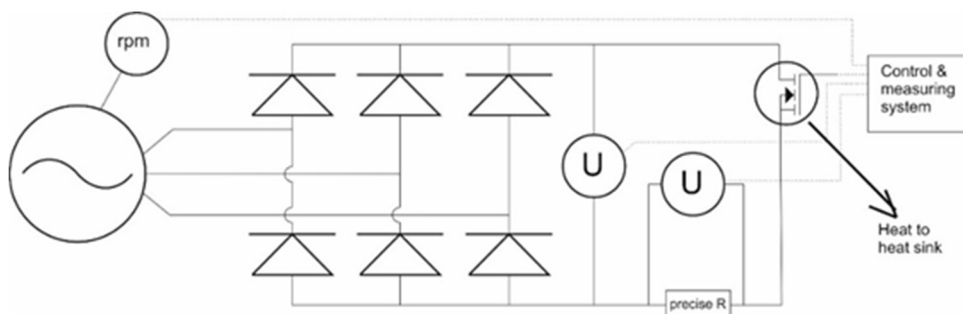


Figure 81. Electronic conceptual circuit diagram of the individual electronic units in the micro turboexpander power measurement system.

As a final choice regarding electrical output, the variable frequency drive (VFD) which can work from a common DC bus to which is connected a recuperation unit (active front end, AFE) configuration is selected as a final option from the electro-mechanical options for all considered options. As so the rotational speed can be controlled by the VFD. The rotational speed is controlled based on the results from the CFD off-design calculations and predicted maximum efficiency points for a measured pressure ratio. This is basically an option tested already at the CTU test rig as well as it is the configuration installed in the EXPAND test rig (VFD has frequency by default up to 400 Hz, on demand optionally up to 1000 Hz. Rotational speed then depends on the number of coils and magnets of the generator.)

3.8 Commissioning

3.8.1 Axial MM turbine

The initial commissioning phase of the developed turbines took place in the air testing system, primarily to provide a mechanical integrity check-up. A demonstrational picture of the test rig for isentropic efficiency measurements and compressed air in *PDLT*² OTH Amberg-Weiden is pictured in Figure 82.

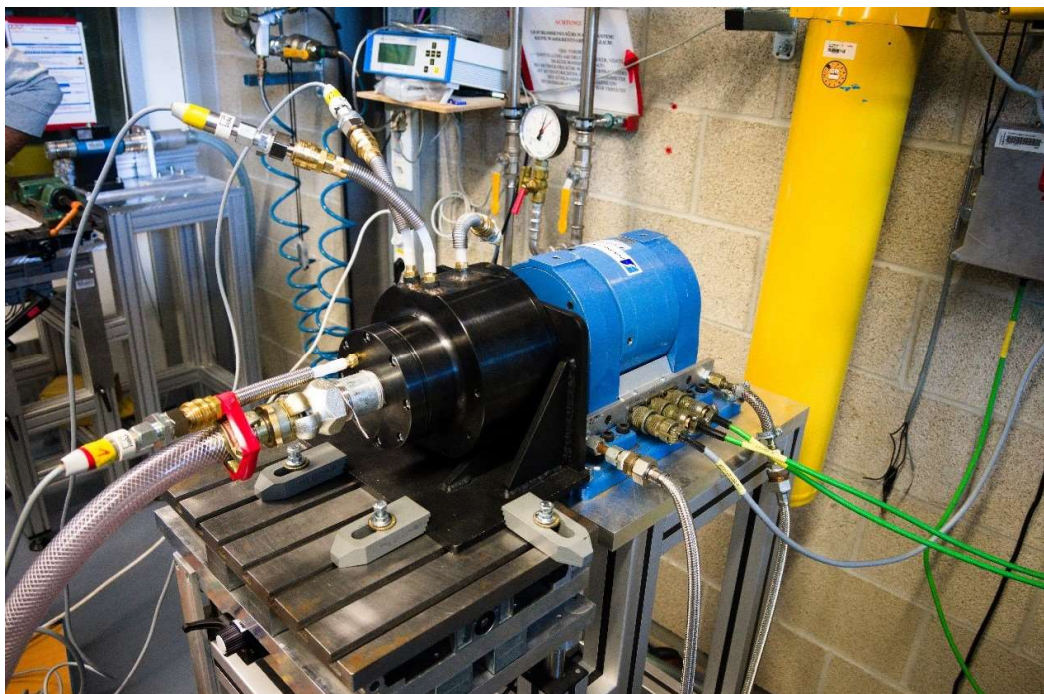


Figure 82. Experimental set-up in *PDLT* OTH Amberg-Weiden of the axial MM turbine to test the isentropic efficiency of the machine on various different pressure ratios and rotational speed with compressed air.

The measurements performed in *PDLT* OTH Amberg-Weiden with compressed air were carried out in a wide range of rotational speeds and pressure ratios to get an extensive range of data points and efficiency curves. The results of these measurements cannot be directly comparable to the ORC working fluid measurements, as the inlet and outlet conditions of the fluid flow are significantly different. Especially the pressure ratio in the supersonic nozzles and the overall enthalpy drop in the turbine stage is far apart from the design case in the ORC. Still these measurements bring significant value to confirm mechanical integrity, stability of the designed turbine in high rotational speeds and also to verify the choking mass flow rate of the nozzles – the precision of the manufacturing of the machine.

Of course, when commissioning the first of a kind high speed machine, not everything goes as planned. There were several trial and errors due to excess vibration of the shaft assembly, which resulted in damage of the borosilicate (Borohardcan®) glass canister which seals the hermetic environment inside

² Prüfstand für Druckluftantriebe und -technik (Test facility for compressed air drives an technology)

the ORC turbine to the atmosphere, see Figure 83. However, these issues were identified and addressed already during the air tests, but the improvements to prevent such problems were intricate and the design is constantly iterated for maximum safety of operation.

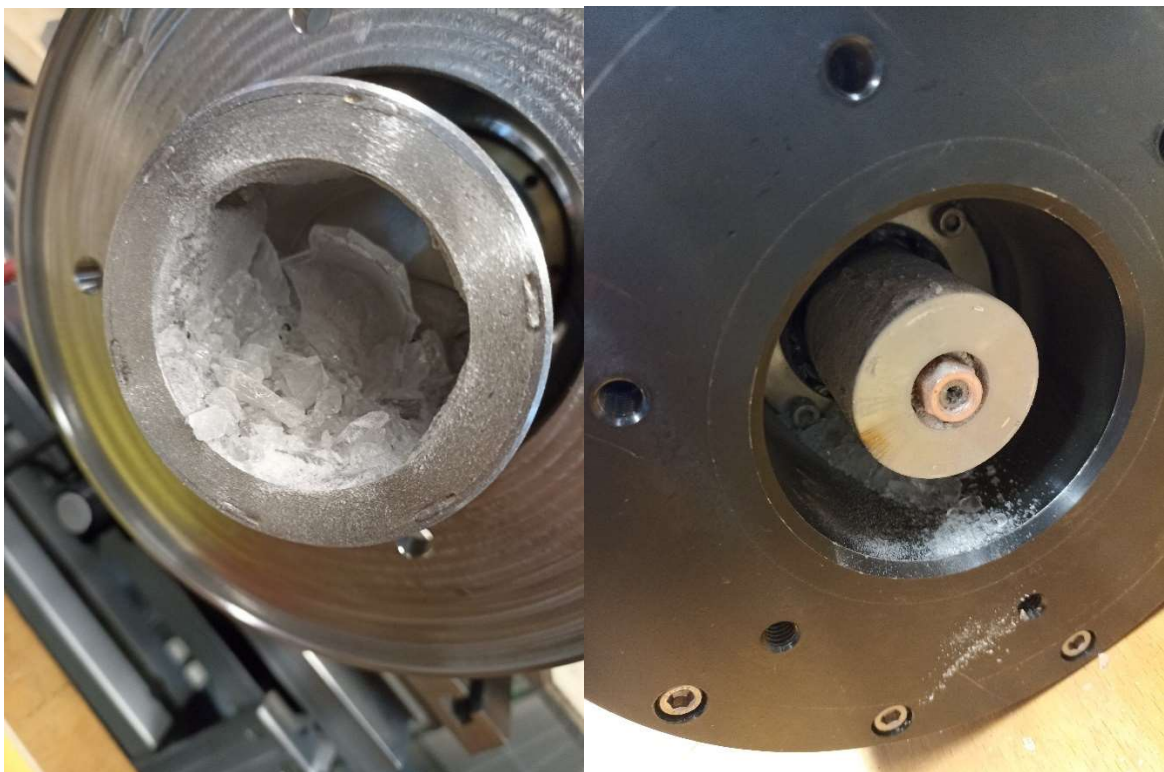


Figure 83. Commissioning issues of the v1 assembly with vibrations resonating the shaft assembly causing extreme shaft runout and collision of the magnetic coupling rotor with a sealing cylinder.

As the shaft assembly is designed to be inserted axially as a whole into the rotor, the bearings need to be pressed onto the shaft first, as is the turbine rotor. The bearing pressing turned out to be a tedious process and several shafts were initially damaged before the tolerances were tight enough but enabled safe assembly in the workshop.

Finally commissioning the axial supersonic turbine into the ORC test rig brought a list of challenges on its own. First of all, the piping connection from the heat exchangers to the turbine inlet and from the turbine outlet to the condenser needed to be redesigned so that the turbine can fit. Another aspect was exchanging the generator from previously used asynchronous 50 Hz standard one to a high-speed generator that can accommodate the high rotational speed of the turbine. This was connected with several changes to the electrical cabinet of the ORC unit as well. The frame of the ORC unit was fitted with additional dampening to reduce the vibrations transmitted from the turbine to the other ORC components. A final assembly inside the ORC system is documented in Figure 84.



Figure 84. A close-up image of the axial supersonic turbine assembly mounted to the 50 kWth ORC test facility.

3.8.2 Axial isobutane turbine

The EXPAND test rig, displayed in Figure 85, completed a successful Factory Acceptance Test 25 August 2021. A partially successful Site Acceptance Test (SAT) was done in May 2022 following installation at NTNU and was followed up by set of a new SAT tests. During these tests, a low-pressure compressor shaft was damaged, see Figure 86, and bearings of the compressors needed replacement. After this testing, all turbomachinery (three compressors and one turbine) are currently being refurbished. In addition, all two-way and three-way valves needed refurbishment, new insulated power cables were installed due to signal noise and further improvements of the rig were made. This major refurbishment and upgrade to the rig has caused delays of further testing until late 2024 in project sustainability phase. A one-stage impulse turbine has been manufactured by a given specification for the initial test phase. A one-stage low-pressure reaction turbine has been designed and the parts manufactured and will be tested after the impulse turbine. Further, a high-pressure impulse turbine is currently under design.



Figure 85. Expander test facility at NTNU, Varmeteknisk lab with NTNU PhD candidate. The isobutane turbine is circled in red.



Figure 86. Damaged compressor shaft and related compressor wheel.

3.8.3 Elektra turbine

While assembling the turbine, some points for optimization of the overall design went clear. The handling of both large plates for the housing of the turbine was very difficult. The removal

of both plates was also not very easy due to the large fitting surfaces. For the next Version of the Turbine, "pusher-threads" will be added, so that we are able to push both plates apart. Furthermore, a base is manufactured on which one side of the turbine can be mounted to easily integrate the second part into. Figure 87 documents the installation in the MM ORC test rig. Operation of the Elektra at typical CHP plant's operation conditions was without any complaint. The turbine turned quite smoothly. The operation of the existing CHP system with the alternative expander turned out as "business as usual". As a feature of the MM test rig utilizing by standard an RVE expander and the having installed gear feed pump, the MM cycle must operate with some 5 % mass fraction of oil. This oil partly condensed and collected in the turbine (see Figure 88). It surely somehow braked the bucket wheel and significantly reduced efficiency. However, no damage due to oil droplets could be determined. The condensed oil was also collected in the tubes of the pressure sensors and soiled them. The disassembly after the measurements also showed some severe bending of the aluminium wall between the groove of the installed O-Ring and the wall of the outer deflection channel of the turbine. Nevertheless, no strong leakage could be determined at this position in the turbine while measuring. This deformation appeared, due to a too small groove for the used O-Ring. The next Version of the Turbine will have an improved O-Ring/groove configuration for the sealing of the turbine.

The project team (Figure 89) was quite satisfied with the commissioning of the Elektra in the ORC test rig at UCCEB. Tests result are shown within the results section.



Figure 87. Elektra turbine in operation in the CTU UCCEB 120 kWth ORC test rig.

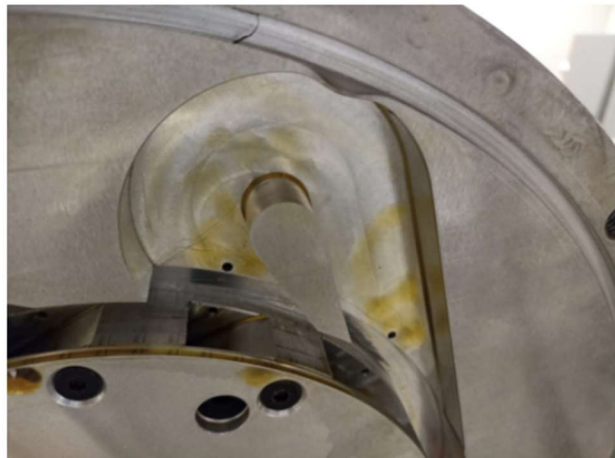
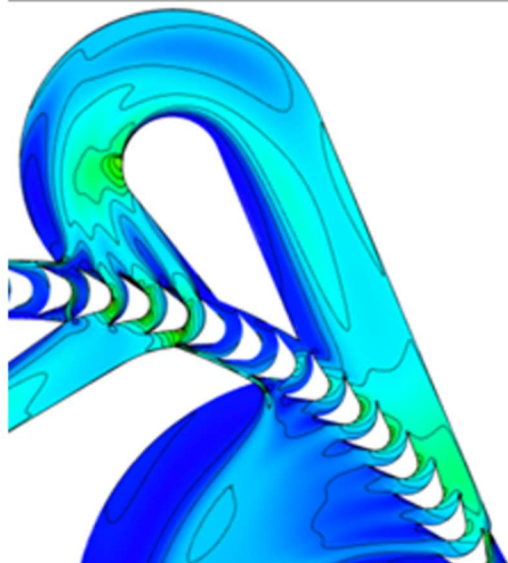


Figure 88. Elektra turbine – comparison of the CFD flow separation and oil marks that indicate a good match in the simulation; + damage of the deflection channel wall by O-ring expansion.



Figure 89. Part of the Czech-German-Norwegian project team after successful measurements of the Elektra turbine at CTU UCEEB.

3.8.4 Air RVE

The redesigned functional sample of the dry oilless rotary vane expander was commissioned in a test rig with pressurized air to measure the torque at different rotational speeds and pressure ratios as well as the volumetric flow rate of the air passing through the machine. The commissioning stage of the measurement was as always not without slight problems. Coupling the vane expander with the electromagnetic brake had to be done as well as alignment of the RVE and brake shafts. Initial trials at low rotational speeds indicated that the vane do not seal the working chambers properly but that was eliminated at higher rotational speeds. This effect was caused by the centrifugal force acting on the vane being too low and thus the vane tip did not seal the chamber between rotor and stator for lower rpm. This effect as surprising during the experiments was already predicted by the design model of the expander.

A demonstrational picture of the functional sample connected to the electromagnetic brake to measure the rotational speed and torque with various inlet pressure conditions is shown in Figure 90. below.

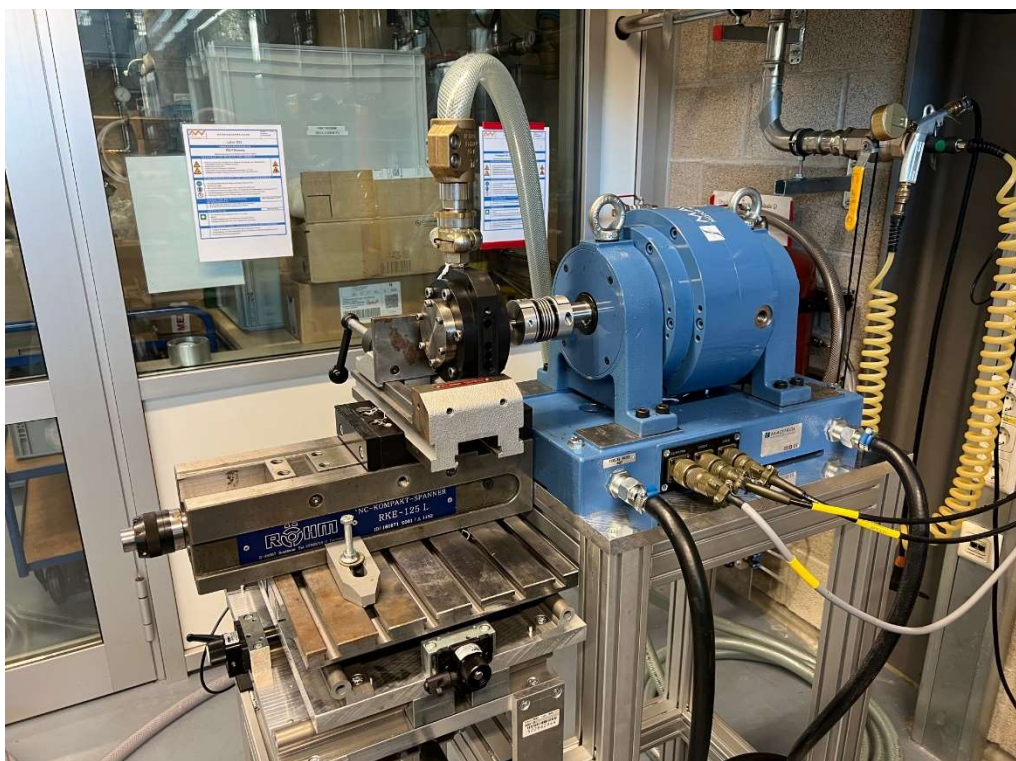


Figure 90. Experimental set-up of the RVE to test the isentropic efficiency of the machine on various different pressure ratios and rotational speed with compressed air.

4 WP4 – Experimental works

First are presented results from air systems. These include the rotary vane expander made to primarily explore impact of dry operation, emulating oilless conditions that would be present with isobutane and many refrigerants application. Air tests also include smaller 3D printed testing turboexpanders and a nozzle rig. Following are the test results of Elektra and axial MM turbine. For them, air tests were also performed first as an essential step during commissioning, after which, data with nominal working fluids validate their performance.

4.1 Air tests with 3D printed plastic turboexpnaders

Previous trial air expanders with components manufactured by various 3D printing methods and from different plastic materials and from stainless steel were revisited. Results of previous along with new tests were analysed and summarised into a manuscript for the HPC conference [15]. The flow components were investigated on a purpose-built pressurized air test rig. The highest obtained isentropic efficiency was around 40% with nylon components from the SLS method, but surprisingly also FDM method had shown outstanding performance. The SLA method, leaving a rather glassy surface and having the best resolution, ended up in our cold air trials poorly, and its brittleness had appeared to be a serious issue for practical applications. Example of results is in Figure 91.

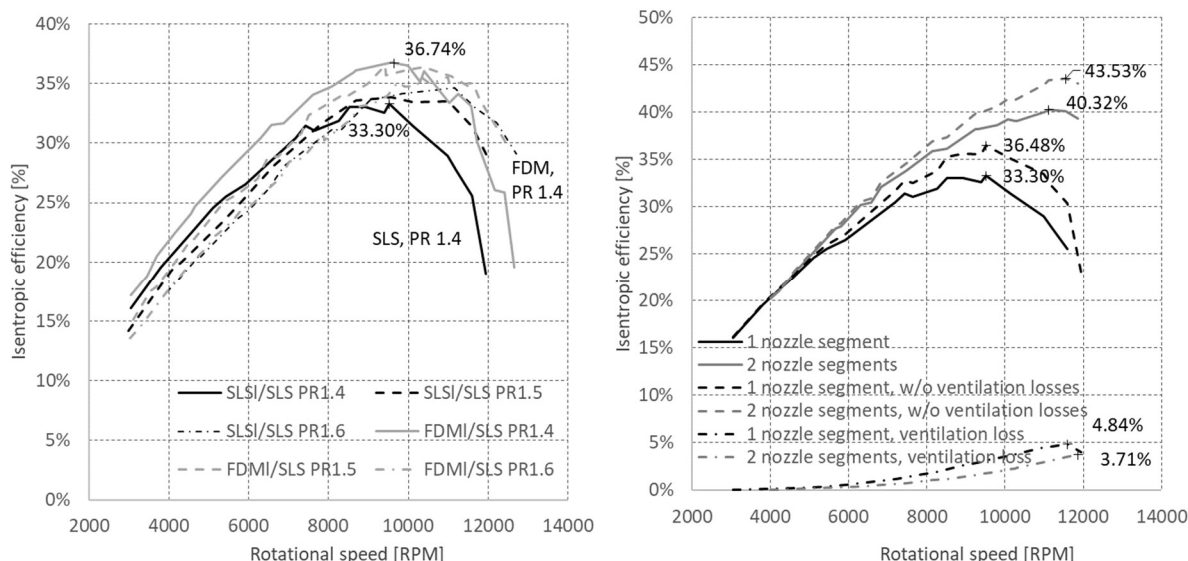


Figure 91. (left) Comparison of FDM and SLS (long chord) stator wheels and the effect of 3-D printing methods on the isentropic efficiency; both with SLS rotor; measured at three different PRs; (right) Effect of the partial admission on the ventilation loss correlation and turbine performance; both stator and rotor - selective laser sintered (SLS, long chord stator)

4.2 Nozzle testing air rig

A specific small air experiment was prepared in order to test and compare the efficiency of the nozzles. The main intention comes to evaluation of real effects of surface quality in 3D printed flow components and effect of their post-processing. Visualisation of the rig is in the Figure 92 below.

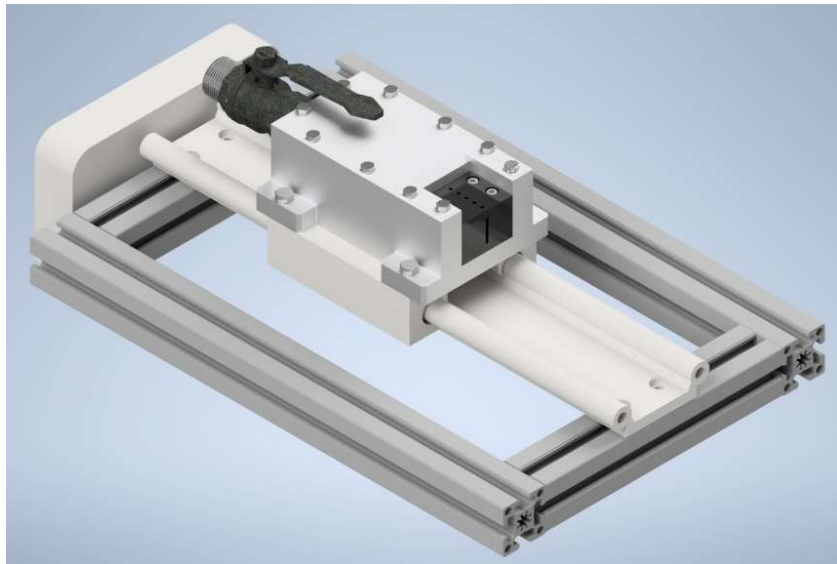


Figure 92. Visualisation of the air rig to test additive manufactured nozzle elements and effects of postprocessing, respectively of the surface roughness.

Photo of the rig is in the figure 36 below. First design has shown with accuracy , so originally used laboratory scale was changed to an Insize 30 N force gauge with $\pm 0.1\%$ accuracy for tension and pressure. For the purpose of measurement, only the tension measurement option was used. The track was modified so that the force gauge could be placed horizontally with the direction of movement of the housing to measure values perpendicular to the movement. Due to the airflow behind the nozzle, it was necessary to install the measuring device on the underside of the track (Figure 93 below)

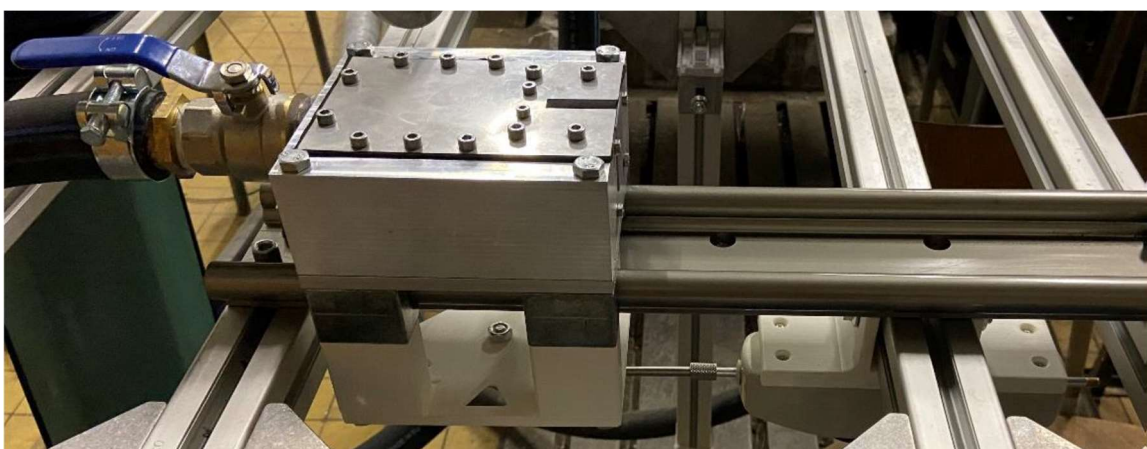


Figure 93. Air rig for measurements of additively manufactured turbine nozzle segments.

T A

Č R

Five measurements of each nozzle segment were done in a measuring device through which pressurized air with values $Qv' = 80 \text{ [m}^3/\text{h]}$ and $p2' = 1 \text{ [MPa]}$ was expanded. This device then induced a pull on the force gauge, from which the resulting applied force was read. These values are then averaged for each nozzle and summarized in Table 21 below.

Table 21. Summary of 3D printed nozzle segment measurement – effect of surface roughness on resulting isentropic efficiency of the expansion; columns (CZ) left to right: additive manufacturing method, material, average thrust of the nozzle [N], average thrust of the nozzle [kg], air exit velocity [m/s], nozzle isentropic efficiency [%].

Technologie aditivní výroby	Komerční název materiálu	Průměrný vypozený tah trysky F' [N]	Průměrný vypozený tah trysky F' [Kg]	Rychlosť za tryskou c2' [m/s]	Účinnosť trysky [%]
FDM/FFF	ASA	22,16	2,26	430,5	81,0
	ASA (Smoothing)	22,38	2,28	434,8	81,8
	PETG	19,32	1,97	375,2	70,6
	PLA	15,46	1,58	300,3	56,5
MJF	PA 12	20,42	2,08	396,7	74,6
SLA	Rigid4000	23,98	2,44	465,8	87,6
	Grey	20,60	2,10	400,2	75,3
SLS	PA 12	20,07	2,05	389,9	73,3

To correlate the surface roughness of the 3D printed nozzle segments with efficiency, surface roughness of each nozzle had to be measured. For this purpose, a confocal microscope was used to determine the surface roughness Ra. A screenshot of the measured nozzle segment surface roughness in 3D is shown in Figure 94 below.

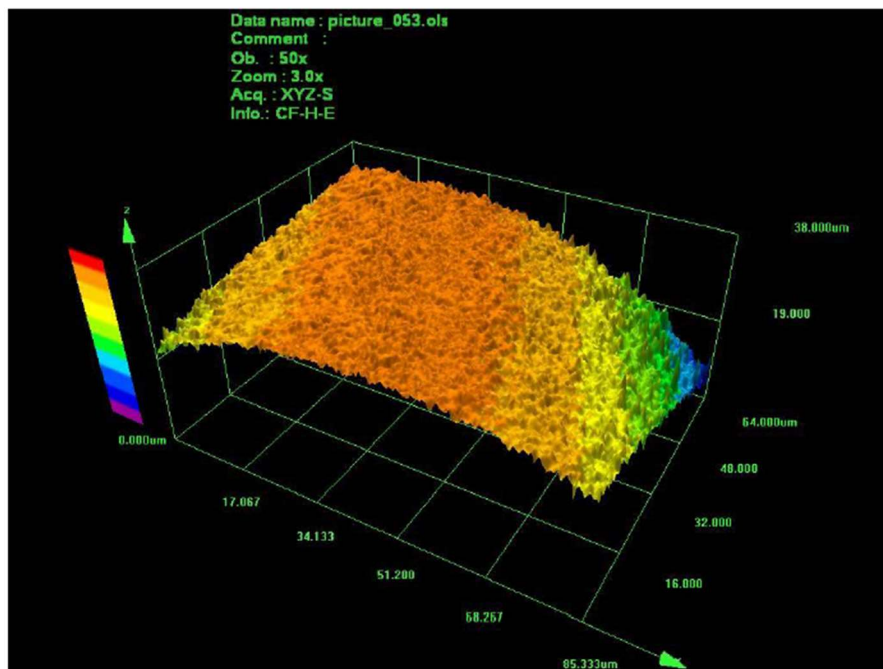


Figure 94. 3D printed nozzle (ASA material) segment surface roughness measured using 3D optical measurement device.

The graph in Figure 95 compares the efficiency and surface roughness of each nozzle, which were measured using a confocal microscope and a force gauge. Consistent with our assumptions, higher surface roughness is associated with higher nozzle efficiency. The measurement results show that the Rigid 4000 material produced by additive SLA technology shows the most promising results. The graph describes the efficiency η [%] (y-axis) versus surface roughness R_a [μm] (x-axis) for each nozzle and is interleaved with a linear regression, which is expressed by equation below.

$$y = -3,5059x + 90,892$$

Where $y = \eta$ [%] and $x = R_a$ [μm]. The condition for the validity of this regression formula is that the Mach number and Reynolds number are $Ma = 2.15$ [-] and $Re = 763,393$ [-], which were calculated from theoretical calculations at the nozzle outlet.

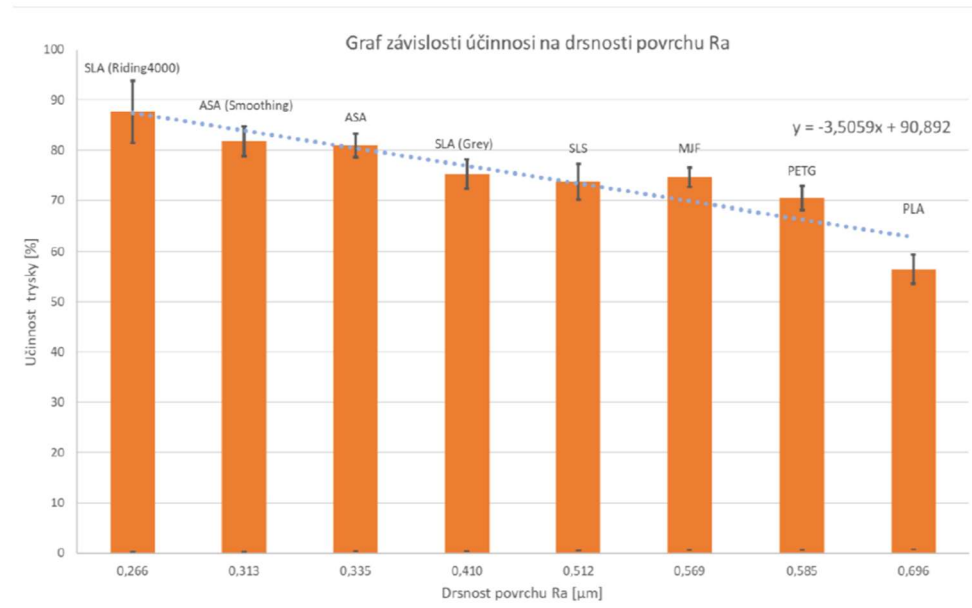


Figure 95. Correlated efficiency of the 3D printed nozzles to the measured surface roughness Ra.

4.3 Oil-free RVE tests

4.3.1 Performance tests

The functional sample of the oilless (dry) RVE was tested for performance and reliability on the test rig with compressed air which schematics follows on Figure 96. The image presents a schematic of a compressed air energy system featuring a rotary vane expander (RVE). Air enters through a compressor, is stored in a pressure vessel on higher pressure, conditioned in an air service unit, and regulated by a pressure valve. A manual ball valve controls the flow to the RVE, which outputs mechanical energy (rpm, torque). The system is designed for energy extraction from compressed air, to test various flow conditions (pressure ratios, rotational speeds) of the machine operation. Furthermore, this facility is capable to measure all the necessary flow properties of the working fluid such as pressure, temperature, volumetric flow rate.

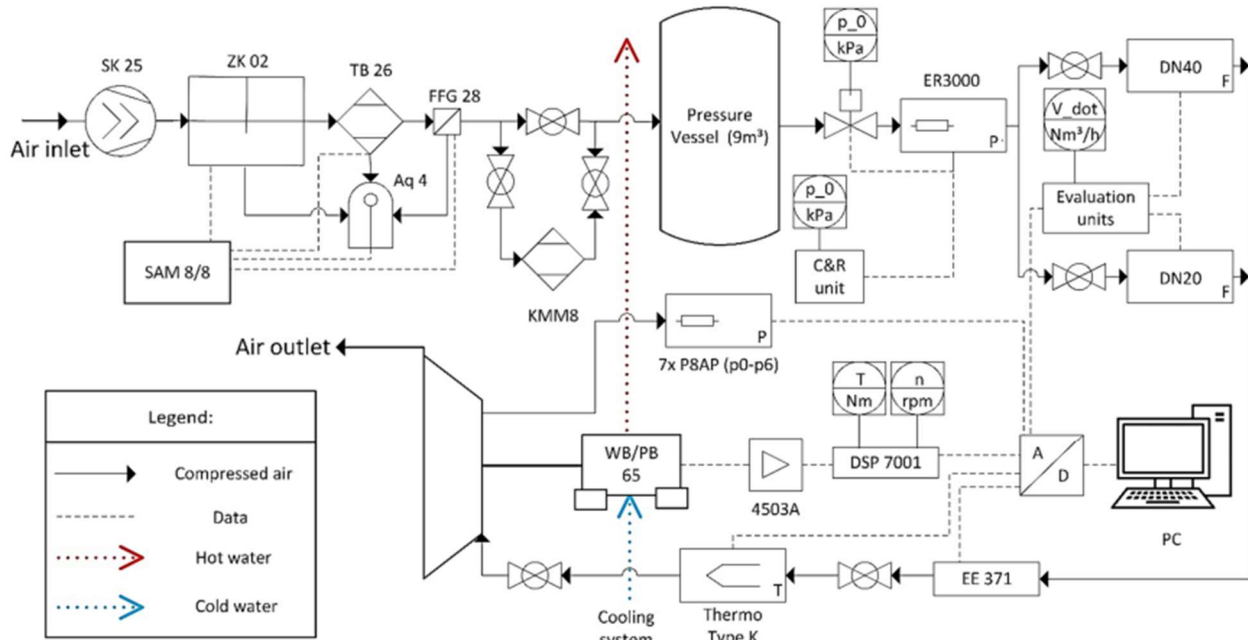


Figure 96. Schematic Diagram of a Rotary Vane Expander Test rig facility.

The Figure 97 shows a set of four performance subplots from an experimental measurement of a rotary vane expander using compressed air and an electromagnetic brake as displayed in Figure 90 above. Each plot represents a different performance metric as a function of rotational speed in revolutions per minute (rpm).

1. **Torque (Nm)**: the top left plot shows torque in Newton-meters. The data points, differentiated by the inlet pressure of 6 bar (triangles), 8 bar (squares), and 10 bar (circles), indicate that torque generally decreases with an increase in rotational speed.
2. **Power (W)**: the top right plot represents power in Watts. Similar to torque, power shows a trend where it increases with rotational speed. This is consistent across all pressures, with the 10 bar pressure condition achieving the highest power output. This is the most linear function of rotational speed with little effect of inlet pressure.
3. **Volumetric Efficiency (%)**: the bottom left plot shows volumetric efficiency in percentage. The efficiency increases with rotational speed. Higher pressures appear to yield better volumetric efficiency.
4. **Isentropic Efficiency (%)**: The bottom right plot presents the isentropic efficiency. This efficiency metric shows an increase with rotational speed and is similar to the volumetric efficiency trend.

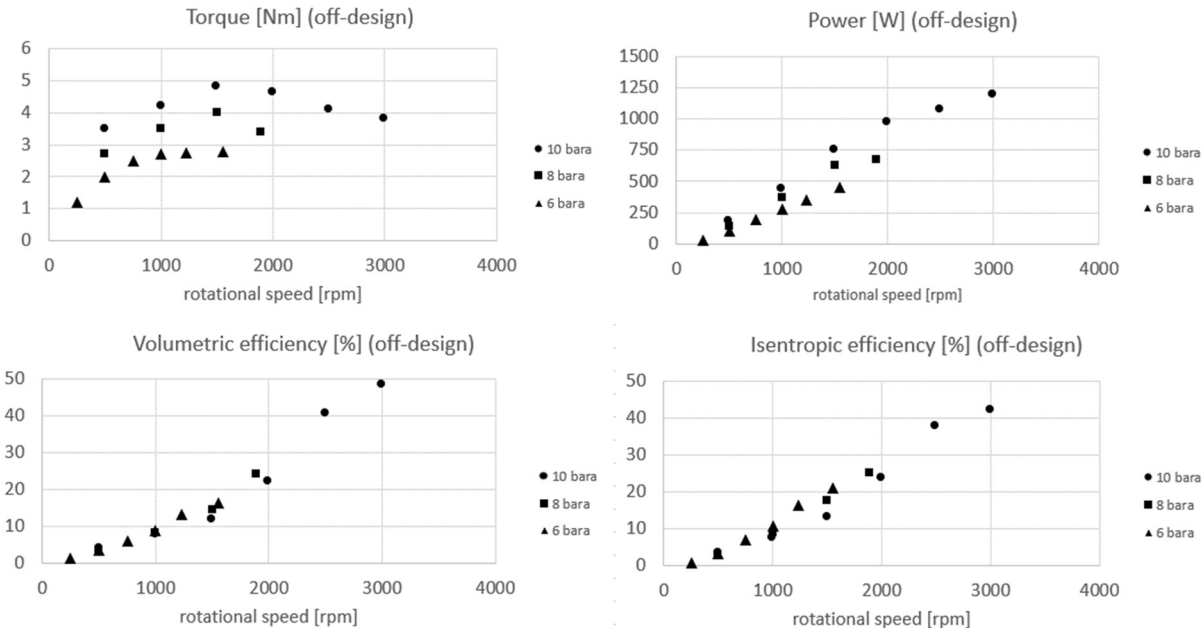


Figure 97. Experimental performance characteristics of the RVE at varying pressure.

Contradictory to expectations, the RVE's isentropic efficiency was not as sensitive to changes in inlet pressure, as expected, but was strongly dependent on rotational speed. This confirms the thesis, that at low rpm the chamber sealing of the vanes is not sufficient and a large tip leakage occurs due to low centrifugal forces acting on the vane at low rpm. Sealing of the vane is sufficient for rotational speeds over 2000 rpm.

Figure 98 then highlights the performance at nominal pressure ratio and confirms replicability of the measured results near nominal speed. Note that additional measurements at lower speed were not preferred due to risk of mechanical failure when operated at these conditions for prolonged periods as a result of insufficient centrifugal force, vanes first not being extended to the chamber surface followed by their impact in each revolution.

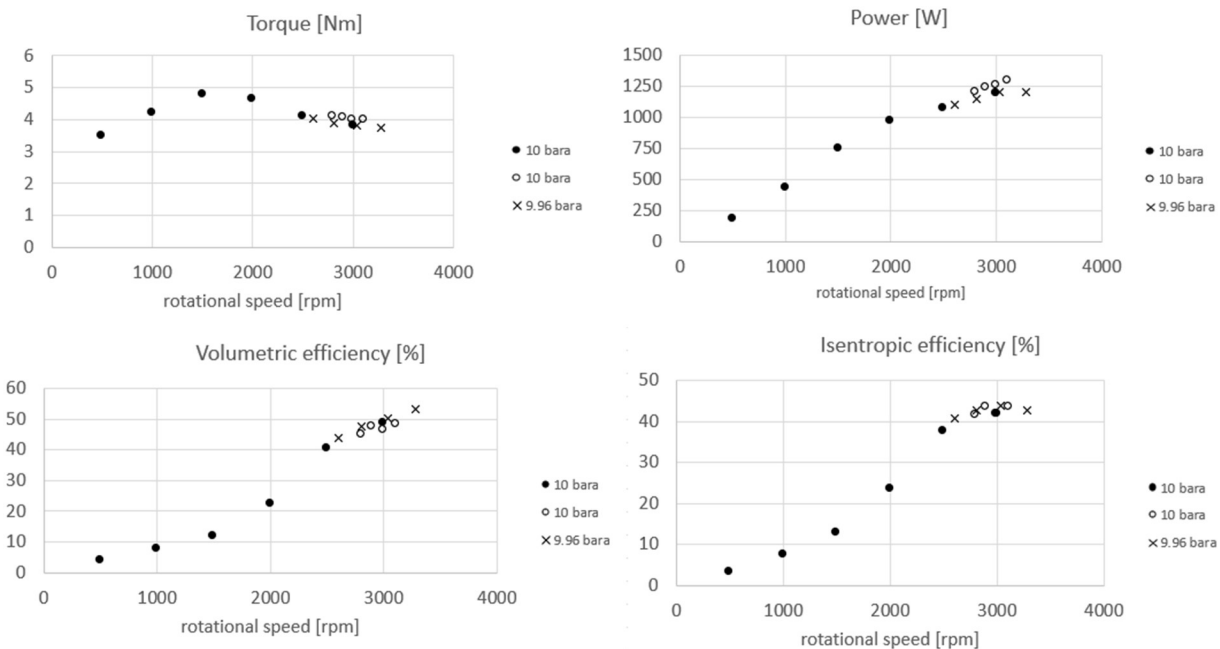


Figure 98. Experimental performance characteristics of the RVE at nominal pressure.

The measurements confirmed and the design efficiency of the RVE and the prediction of the leakage area loss model of the RVE. Volumetric efficiency of the machine at design pressure ratio achieved roughly 50% and isentropic efficiency of 44%, producing over 1300W of mechanical power.

4.3.2 RVE vanes durability tests

A testing stand for long term durability tests of vanes was assembled using the RVE functional sample with asynchronous motor (normally used as generator), programmable frequency converter and a pipe to dampen the noise as seen in Figure 99. This set-up then by running the motor emulates the long term expander operation.



Figure 99. Experimental stand for long term vane durability testing.

This experimental analysis yields after nearly 100 hours of operation some mixed results. Positive aspect is that the vanes did not fail but minor signs of wear were already visible and the friction between. A further investigation is recommended for follow-up activities. Currently recommended solution for oil-free operation is in regular supply system of a very small amount of a dry lubricant such as MoS₂. Note that this dry lubricant has been tried in the initial phase of the test and the data on friction resistance (power consumption) do indicate a transfer point between stable operation as long as the lubricant is present and slightly increased resistance once the lubricant wears off.

4.4 MM test rigs refurbishing

After the fire incident at one CTU MM rig during long term operation experiments, major refurbishments were needed, though it is also taken as an opportunity for multiple improvements of the rig aspects. For illustration, Figure 100 illustrates the state of the ORC system after the incident and during refurbishments.



Figure 100. MM testrig after the incident and during refurbishments.

In the refurbished system, a new concept of the flue gas heat exchangers was adopted, as documented in Figure 101. Previous costly approach with helical pipe welded between each wound was changed to helical wounded pipe wounded onto a larger cylinder, thus providing more cost effective solution and also further limits the risk of hot spots.



Figure 101. New concept of the MM testrig heat exchangers.

The refurbishments were finished and the testrig was again operational and long-term tests with the RVE were continued. Long-term tests show that this is a reliable machine for the long term if the

problems of blade wear, rotating surfaces and stator bore surface can be solved. The vanes are undoubtedly the most stressed part of the expander. In the original blade expanders developed at UCEEB CTU, experiments were carried out with graphite blades or graphite composites (different types of graphite reinforced with carbon fibre and doped with other elements to reduce friction). Such blades were light and had a relatively low coefficient of friction. However, they also had negative properties, including lower wear resistance (weight loss was low, but would lead to failure in the long run), lower resistance to impact fracture and too low a density. As has been shown experimentally and mathematically, the low density of the material, i.e. the weight of the blades, resulted in insufficient centrifugal force acting on the blades, causing the working chambers not to close and thus significantly reducing the thermodynamic efficiency of the machine. The blade material was therefore replaced with high-strength steel, while at the same time intensive work was carried out on the surface treatment to ensure that the blades would last over the long term. At the same time, the replacement of the carbon composite with steel resulted in a significant increase in the thermodynamic efficiency of the blade expander. We are currently working on the blades in terms of the appropriate type of DLC coating, the materials of the blades, rotating surfaces and stator, the method of machining the inner stator bore and its final properties (e.g. roughness, coating, etc.). At present we have achieved about 1000 hours of operation with acceptable wear, but testing will continue with further modifications. Example of the current wear of the expander is in Figure 102.

There may be other problems with the bearings, but we have not encountered any problems so far in the test period. The bearings are also extremely stressed, operating at temperatures of around 190°C and the forces on them are enormous. They reach up to 7.8 kN peak (or 3.9 kN per bearing).



Figure 102. Wear of the RVE after long-term trials, wear of the rotation faces (left), of the vanes from original width 24 mm (right) and stator (bottom).

4.5 Elektra turbine tests

4.5.1 Air tests

A purpose-built test rig (Figure 103) with compressed air for mechanical integrity check and measurement of the expansion characteristics of the Elektra turbine was designed, built and tested. This device helped to ensure safe operation when the Elektra turbine was fitted to the ORC machine.

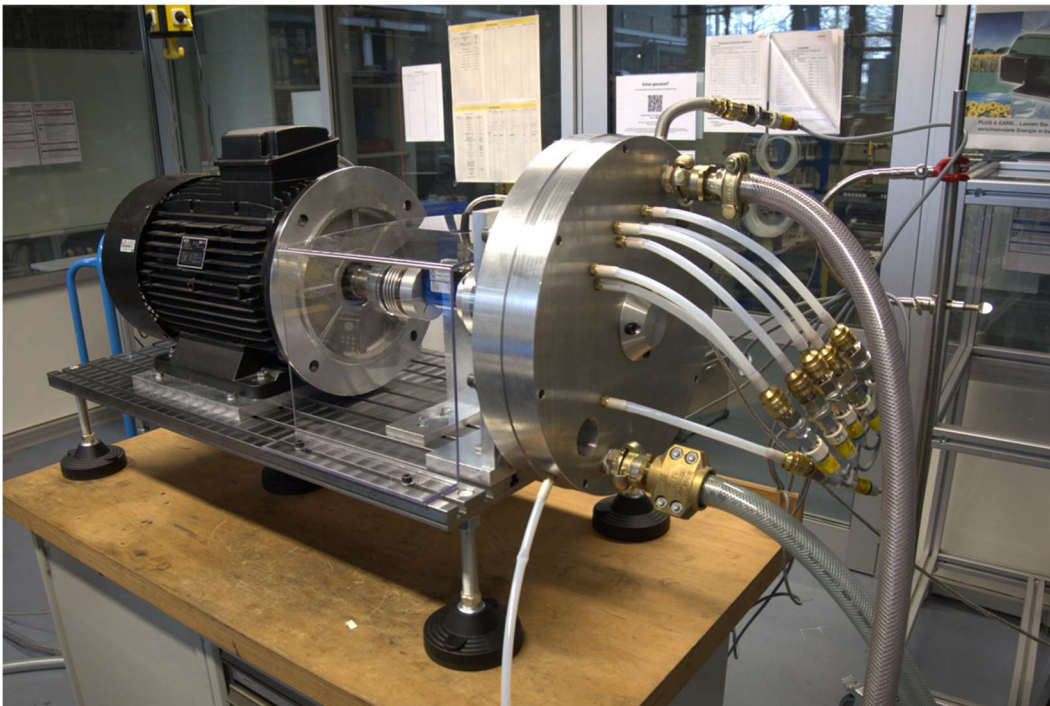


Figure 103. A custom built test rig to measure mechanical design and expansion efficiency of the velocity compounded Elektra turbine.

The test rig allowed us also to measure the manufacturing precision as the turbine met the design mass flow rate at the given pressure ratio within a marginal error caused by the precision of the measurement devices as can be seen in Figure 103. Finally, the isentropic efficiency of the expansion turbine was measured with pressurized air for a range of rotational speed and pressure ratios. Please note that for 7 bar, the measuring range of the shaft torquemeter did not allow us to measure at lower rotational speed (thus higher torque). Figure 104 displays the mass flow rate passing the turbine as a function of inlet pressure i.e. the swallowing capacity of the turbine. The results of the 1DTDT, the CFD analysis and finally the measurements are shown. It is obvious that all three curves coincide almost perfectly. The choking convergent-divergent nozzles show the expected linear dependency of the mass flow rate to the inlet pressure.

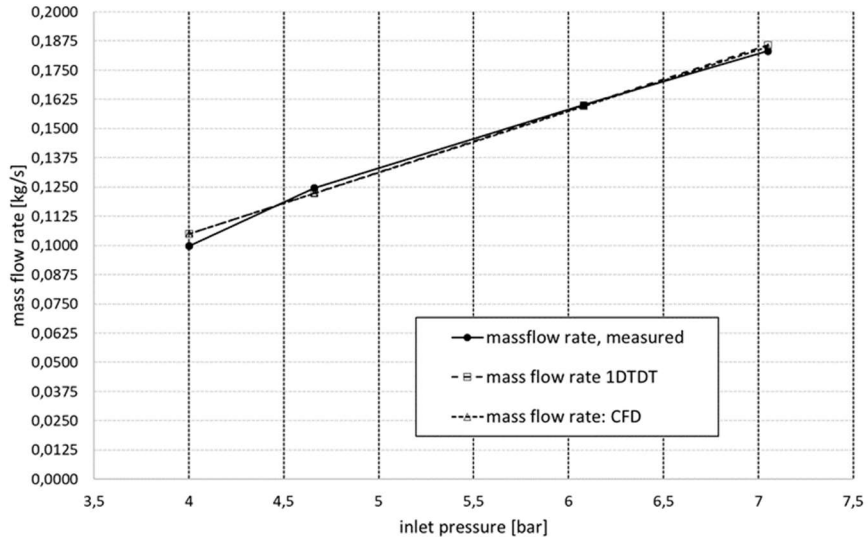


Figure 104. Mass flow rate of the pressurized air as a function of turbine inlet pressure based on 1DTDT, 3D CFD and measurements (choked flow condition in the nozzles).

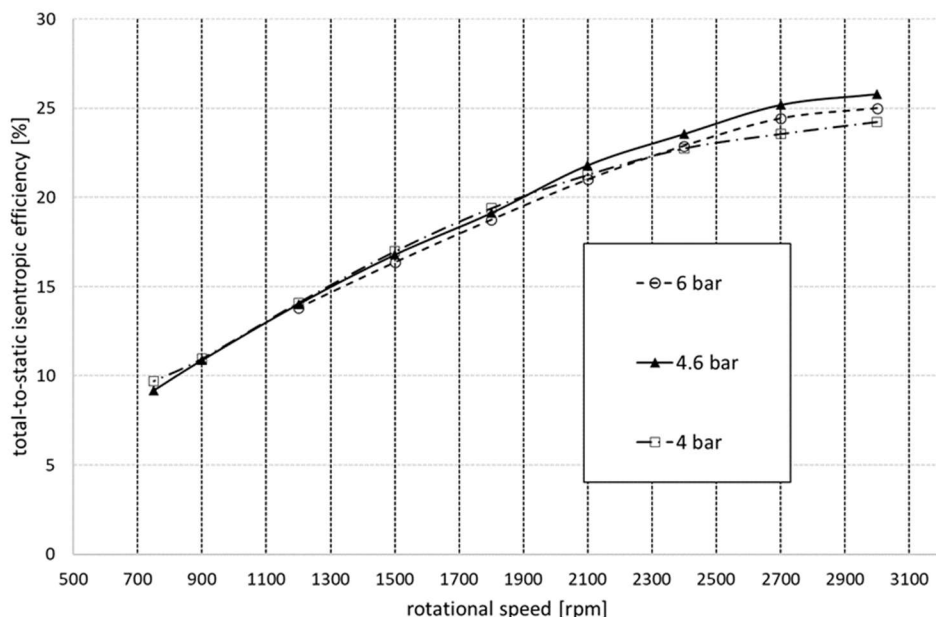


Figure 105. Experimentally determined total-to-static isentropic efficiency of the turbine as a function of rotational speed and turbine inlet pressure (outlet pressure kept constant at 1 bar).

The turbine does not show a noticeable dependency on the inlet pressure (i.e. with constant outlet pressure) the pressure ratio of the turbine as can be seen in Figure 105. The curves for 6, 4.6 and 4 bar are almost identical for the whole rpm range. The independence can be explained by the design boundary conditions of the turbine. The boundary conditions of the compressed air measurements are far away from the boundary conditions of the ORC design. This is why the supersonic nozzle of the

turbine does not function as designed at any of the inlet pressures. Still, the highest efficiency is reached at around 3000 rpm - the design speed - and the curve shows a stagnating or even declining trend after that point. Unfortunately, measurement with higher rpms could not be carried out due to the limitation of the frequency converter used in connection with the generator of the assembly.

further measurements of the Elektra Turbine with pressurized air have been carried out to investigate, if it is reasonable to compare off-design, off-medium measurements with off-design, off-medium CFD calculations for turbine performance analyzation and optimization. Table 22 shows the comparison of the boundary conditions of the design point of the turbine and the off design/medium boundary conditions for the CFD calculations and the measurements.

Table 22. Comparison of the boundary conditions of the design point and the off design/medium CFD/Measurements of the Elektra Turbine.

	Design Point	Off design/medium CFD/measurements	Unit
Medium	Hexamethyldisiloxane (MM)	Air	-
Inlet pressure (absolute total)	6.5	3 - 6	bar
Inlet temperature (total)	463	293	K
Outlet pressure (static)	0.55	1 (atmospheric)	bar
Rotational speed	3000	1000-3000	rpm

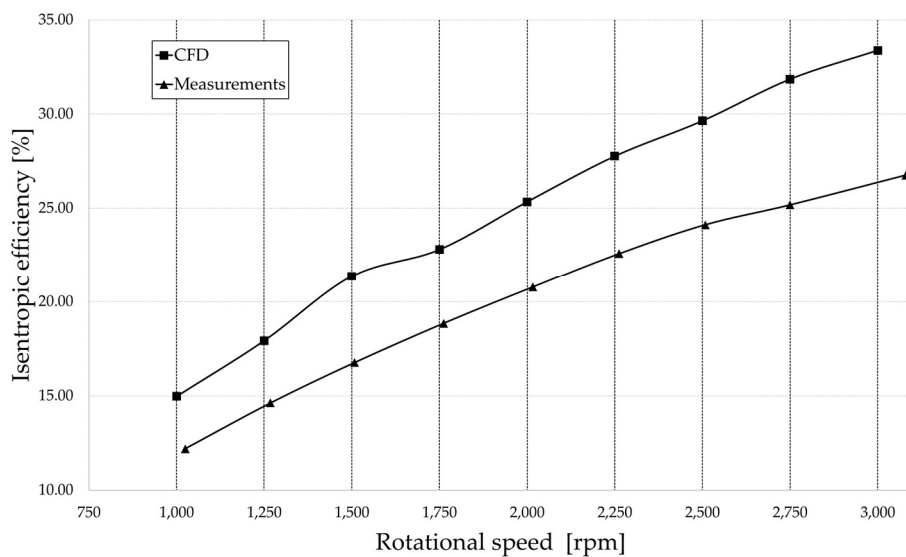


Figure 106. Comparison of the performance map of the Elektra turbine from CFD calculations and measurements for 6 bar inlet pressure and air as working fluid.

Figure 106 shows the comparison of the performance map of the Elektra turbine measurements and CFD Calculations for pressurized air. It becomes immediately clear, that there is a deviation of the

isentropic efficiency from around 3 %-points at 1,000 rpm to around 5 %-points at 3,000 rpm, which the CFD calculation is above the measurements. The deviations slightly increase from lower to higher rotational speeds. These deviations can be explained by the rather simple CFD-model of the Turbine (no axial gaps, less leakages) and the missing bearing friction.

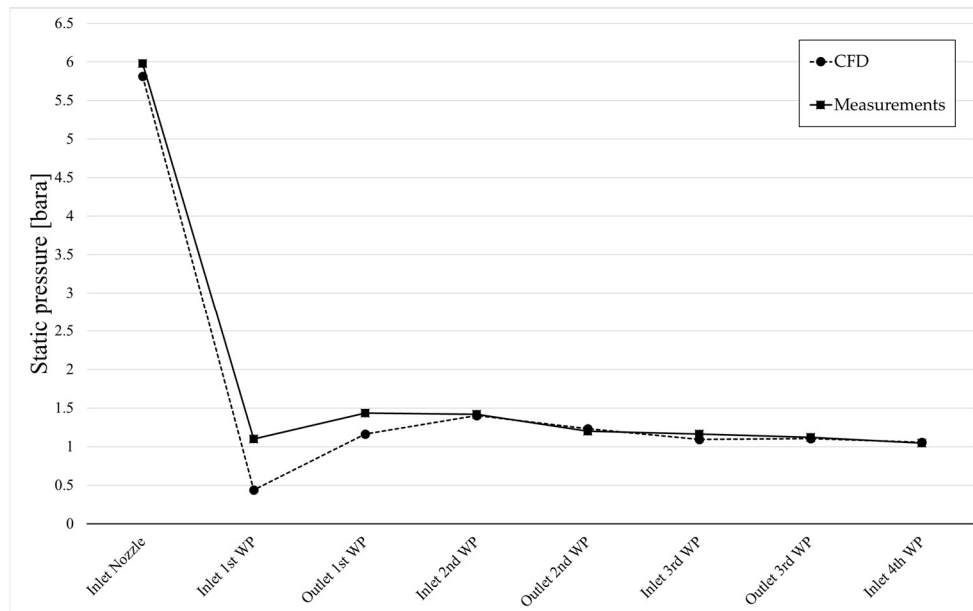


Figure 107. Comparison of the streamwise static pressure distribution over the Elektra turbine from CFD calculations and measurements for 6 bar inlet pressure (WP = wheel pass).

Figure 107 shows the comparison of the streamwise static pressure distribution of the measurements and the CFD Calculations of the Elektra Turbine with pressurized air. The results show that the pressure distribution over the turbine almost overlap over a wide range (Inlet 2nd WP to Inlet 4th WP) and only deviate from each other by approx. 0.5 bar at the Inlet 1st WP – which is also the outlet of the nozzle. This deviation could be explained by the strong shockwaves, that are in the region of the nozzle outlet/wheelpass inlet. The pressure measured in this area strongly depends on the actual position of the pressure probe. If the positioning of the probe is slightly displaced, the pressure measured in this position could be strongly different. The CFD value in comparison shows a surface averaged pressure in this area and therefore, the deviation can be larger.

This comparison ensured that the off-design, off-medium measurements and CFD simulations can be compared well with each other. The CFD simulations show the basic course of the efficiency curve and reproduce the pressure curve in the turbine well. Based on these results, it can be assumed that further optimization of the turbine is possible using this approach.

4.5.2 MM ORC Elektra tests

Another functional sample of a turboexpander measured in the MM test rig at CTU UCEEB was the velocity compounded radial Elektra turbine promising decent isentropic efficiency at low rotational speed, low maintenance and low cost of manufacturing and easy assembly with reliable operation. After the turbine was designed, manufactured and assembled, as discussed in the previous chapters, it was fitted to the ORC test rig and several measurements were performed to get longer time performance of the turbine as well as steady states for given pressure ratios. A picture of the experimental setup of the turbine located inside the biomass-fired CHP ORC unit is shown below as Figure 108.



Figure 108. Experimental setup – biomass-fired 120 kWth CHP ORC unit equipped with ELEKTRA turbine.

The measured power at different operating pressures is presented in Figure 109. The efficiency chart in Figure 110 represents the assessment of the total-to-static isentropic efficiency from the preliminary Elektra tests in the MM-ORC unit and compares it with the data obtained earlier with pressurized air (section 4.1). The electrical power output of the generator divided by the formerly measured generator efficiency was used to determine turbine shaft power. The isentropic enthalpy drop was determined using measured total inlet pressure, total inlet temperature and static outlet pressure applying Refprop database [16]. The mass flow rate through the turbine was derived applying the theoretical swallowing capacity of the convergent-divergent turbine nozzles which had been tested and confirmed earlier with air (see Figure 104).

The two distinct lines for MM operation account for whether the wetness losses due to the lubricating oil droplets (the ORC working fluid contains lubrication oil dissolved within the MM) are accounted for into the efficiency evaluation of the Elektra turbine or not. The maximum measured total-to-static isentropic efficiency was at lowest measured pressure ratio (MM) roughly equal to 6 and it was recorded as 45.5 % when the wetness losses by oil droplets were corrected according to the Baumann rule: 1 p.p. efficiency for 1p.p liquid [17].

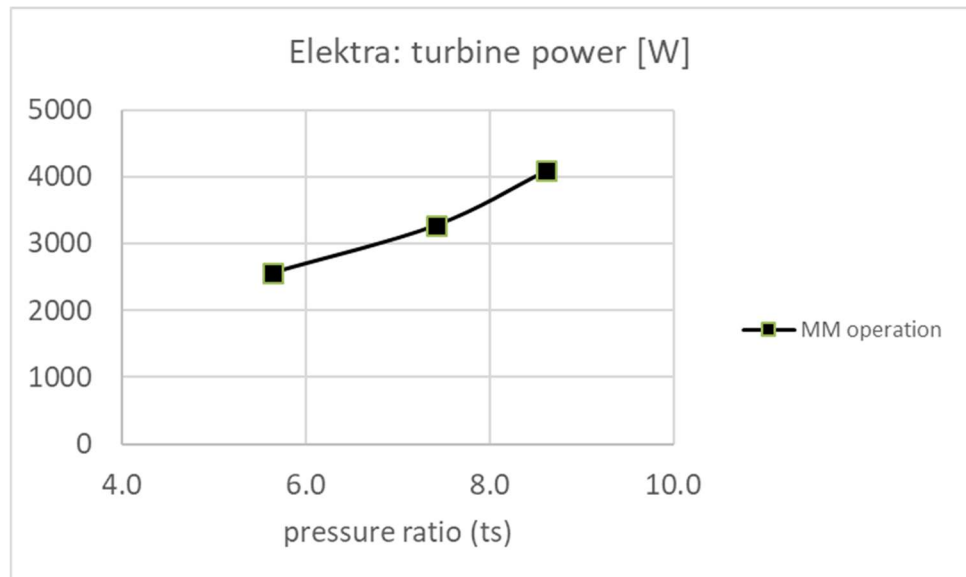


Figure 109. Results (Power Output) of the preliminary measurements of the functional sample of the Elektra turbine in the MM ORC test rig.

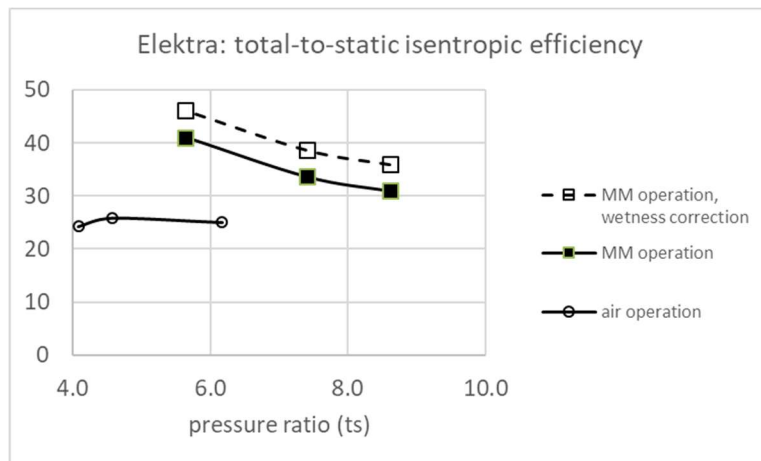


Figure 110. Results of the preliminary measurements of the functional sample of the Elektra turbine in the MM ORC test rig compared to the compressed air operation measurements.

4.6 Axial MM turbine tests

4.6.1 Air axial turbine tests

Figure 111 illustrates the efficiency curves of an axial turbine as determined by compressed air tests in *PDLT* (see Figure 82 for reference of the test rig), plotted against the turbine's rotational speed. The curves represent four different inlet pressures, each denoted by a unique colour and line style. As rotational speed increases, the efficiency of the turbine initially rises, indicating a positive correlation between speed and performance up to a certain threshold. The efficiency peaks at varying levels for each inlet pressure before either plateauing or declining. This suggests an optimal operational speed range for the turbine where efficiency is maximized.

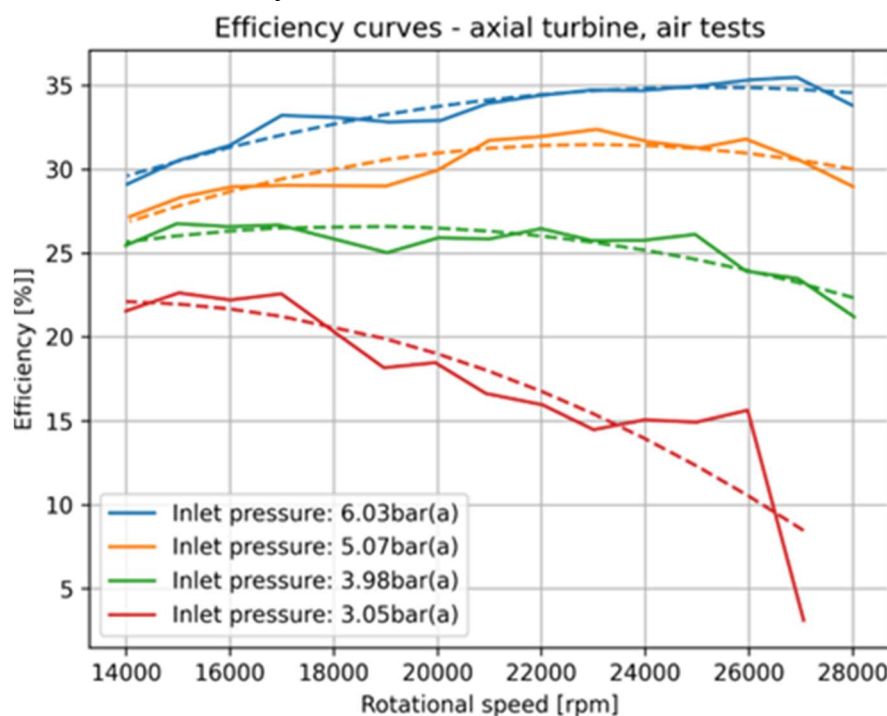


Figure 111. Isentropic efficiency as a function of rotational speed for various pressure ratios measured with compressed air.

4.6.2 MM ORC axial turbine tests

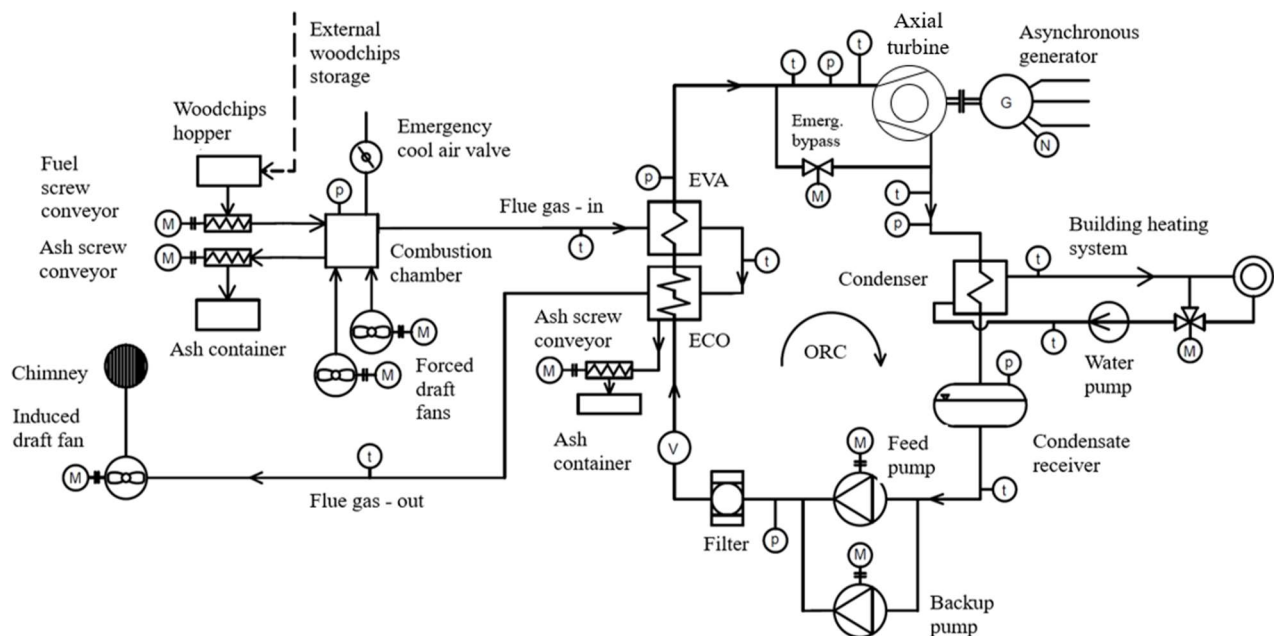


Figure 112. Schematics of the placement of the supersonic axial turbine within the ORC cycle.

The test rig shown in Figure 112 above, previously equipped with a rotary vane expander was redesigned and modified to be able to fit a high-speed axial impulse supersonic turbine. New piping from the outlet of the turbine to the plate heat exchanger condenser was manufactured and more pressure probes measurements were added to the control and DAQ system of the unit. The previously used asynchronous generator was disassembled and exchanged for a high-speed generator fitting the turbine assembly, which also induced several changes in the electrical junction box – a high speed frequency converter was added, and the control system of the unit was updated. The metal frame that supports the axial turbine was improved by additional dampening to reduce the transfer of high frequency vibrations to the rest of the ORC test rig. A picture of the turbine installed to the ORC test rig follows in Figure 113 below.



Figure 113. A distance view onto the 50 kWth ORC test rig fitted with the axial supersonic turbine.

An experimental campaign was conducted in the MM test rig to measure the performance of the axial supersonic turbine (v1). The measurements were performed at the nominal pressure ratio of 12 with the inlet pressure of 650kPa and superheated siloxane vapor temperature at 190°C. Turbine outlet pressure was at 55kPa controlled by the 3-way valve in the heating system hydronic loop, cooling the condenser. Based on the known state properties of the vapour in the inlet to the turbine (pressure, temperature), known electrical losses of the power components between the high speed asynchronous generator and the electricity meter, turbine shaft mechanical power output can be derived. From the ideal isentropic expansion between the inlet state and the outlet pressure isobar and the turbine shaft mechanical power, so-called isentropic efficiency of the turbine can be calculated.

As the rotational speed of the turbine assembly can be controlled using a frequency converter which controls the rpm of the generator, the rpm of the turbine was varied from stationary to the design rotational speed of 28k rpm. However, when ramping up the v1 turbine, vibration noise occurred repeatedly when reaching 15 000 rpm (see Figure 114). Inherently the turbine assembly was designed

as unstable and was not well rotordynamically balanced. This issue is closer described in chapter dedicated to rotordynamics.

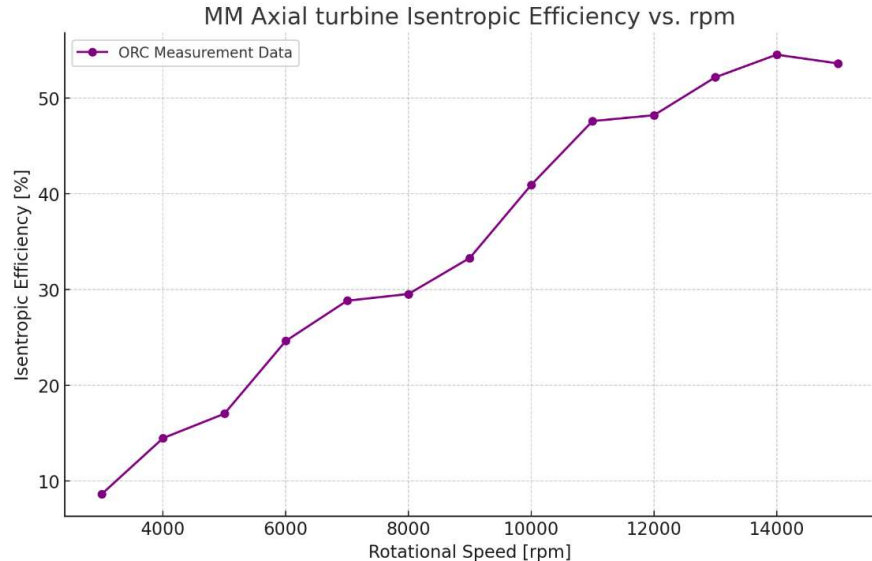


Figure 114 Isentropic efficiency as a function of rpm for the v1 MM Axial turbine - experimental data from the CTU MM test rig

As this problem persisted, experimental measurements in higher rotational speed region closer to the design point were not carried out due to safety reasons. Therefore, a second version of the turbine assembly (discussed in a separate subsection) was designed with more focus on the rotordynamics aspects, bearing reliability and lower design rotational speed. Results from the first experimental campaign with the updated version of the turbine are available below in Figure 115.

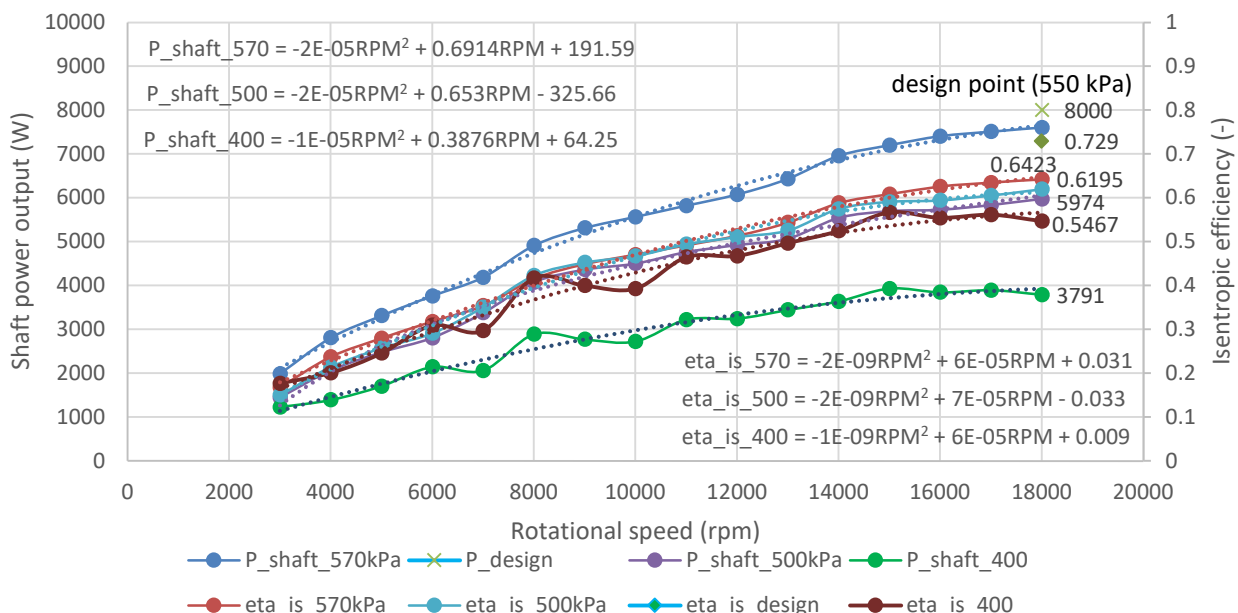


Figure 115 Experimental results of the MM Axial impulse turbine measured at CTU ORC test rig, second version assembly

The Mark II assembly of the axial impulse MM turbine for the CTU ORC test rig boundary conditions performed well in the experimental campaign and the testing was successful. Vibration issues were overcome by the bearing housing subassembly redesign and a new design approach that resulted in lower rotational speed at the cost of larger rotor wheel diameter was proven a good solution. At the design rotational speed of 18k rpm, the turbine underperformed and lacked behind in terms of isentropic efficiency, by 11 % when compared to the design model (8000 W design shaft power output and 72.9 % isentropic efficiency). The authors propose that partially this effect was caused by liquid oil droplets in the working fluid, since the MM is mixed with oil that lubricates the pumps. As a next step, the research team will undertake a new experimental campaign without oil and with surface coated gear pumps in the sustainability phase of the project to prove this point. Another effect might be caused by the excessive tip leakage between the casing and the stator nozzles, where manufacturability and easy assembly was compromised over superior aerodynamic performance. This affect was however not included in the design model and might also cause the discrepancy between the two. A great achievement is the turbines low sensitivity to off-design pressure ratios which could be accounted for the supersonic nozzle design by the method of characteristics. This is especially important for expander machines that will operate in applications with fluctuating heat sources such as waste heat recovery.

Ongoing activities in the sustianability phase of the project will explore higher range of pressure ratios and more off-design operational performance (wet expansion, varying condensing pressure). Results of these trials together with further experimental results of the Elektra turbine will be submitted into a high ranked journal for publication in Q4 2024.

4.6.3 MM turbine data analysis tool

A Python script for automatic experimental data evaluation from the CTU MM test rig was developed and published in the GitHub open access repository. It reads the raw CSV data exported from the PLC of the ORC unit, parses them using the time string in *pandas* library, and using time ranges for steady states, it evaluates the time-averaged steady state measured data (moving window average algorithm). Example of automatically evaluated experimental dataset (data from a trial run to verify functionality of the Python data analysis tool) can be found below in Figure 116.

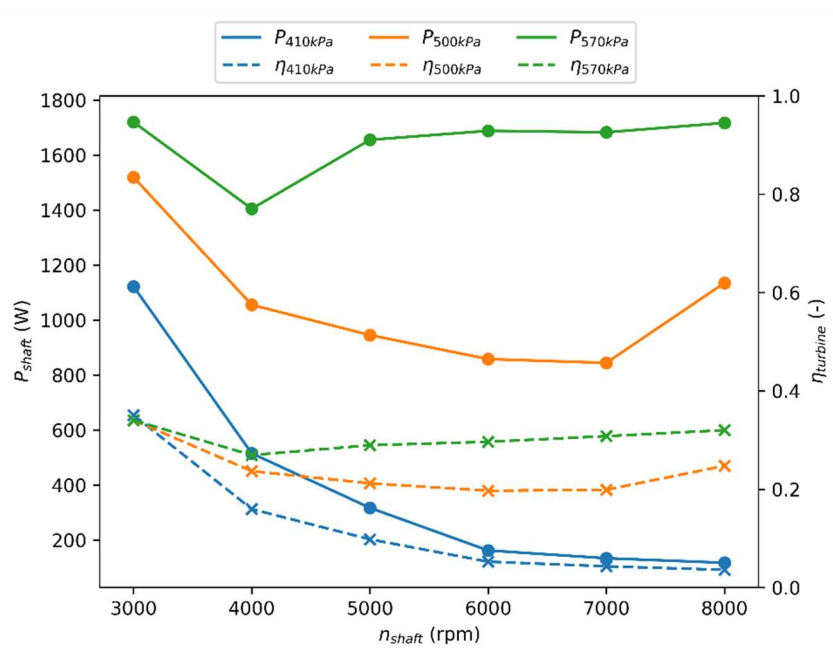


Figure 116. An illustrative example of an automatically evaluated experimental dataset for the MM turbine, power and efficiency at different rotational speeds and turbine inlet pressures.

4.7 Expand rig and axial isobutane turbine tests

The EXPAND test rig completed a successful Factory Acceptance Test 25 August 2021. A partially successful Site Acceptance Test (SAT) was done in May 2022 following installation at NTNU and was followed up by a new SAT in October/November, 2022. During this test, a low-pressure compressor was damaged and carried metal particles through the rig and damaged another compressor. After this, all turbomachinery (three compressors and one turbine) are being refurbished causing delay of further testing. A one-stage impulse turbine has been manufactured and used for the initial test phase. A one-stage low-pressure reaction turbine has been designed and the parts manufactured and will be tested after impulse turbine and refurbishing of the test rig, similarly for a high-pressure turbine.

The test run results presented in Figure 118, were completed as part of one of the SAT when the EXPAND rig was operated. The measured points of the tests are indicated in the P&ID diagram in Figure 117.

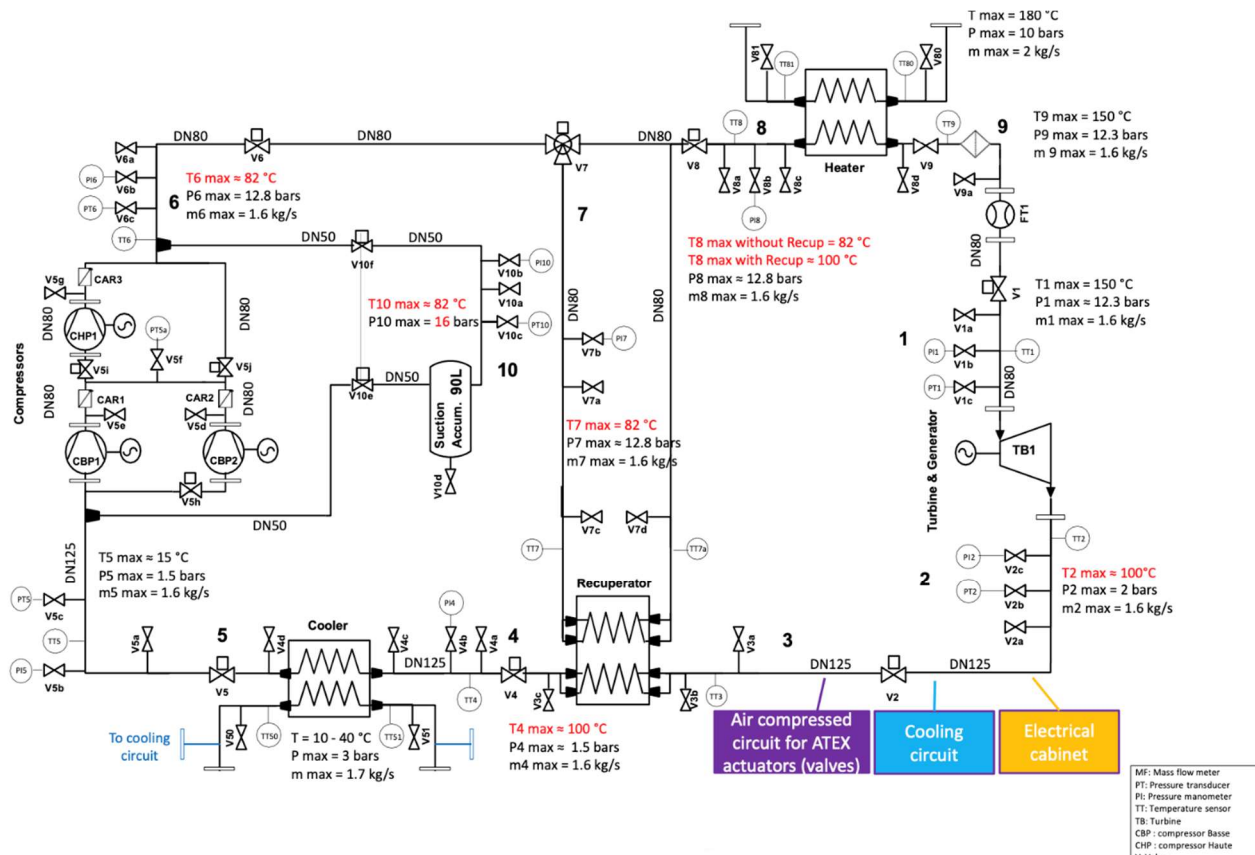


Figure 117. Simplified P&ID of the EXPAND test rig. Maximum temperatures, pressures and mass flow rates are indicated in the plot. In red, the values with activated recuperator or re-compression mode. Valves are labelled, and transmitters are indicated. The turbine is labelled TB1.

Figure 118 showcases that the turbine is operating and reaches an isentropic efficiency of around 60% (+/-10%), which is promising since the aim is to further increase the inlet pressure (from 3 bar to 4 bar), the rotational speed (from 6,000-10,000 rpm to 17,000 rpm), and the mass flow rate (from 1 kg/s to 1.6 kg/s) in future test runs with expectation higher isentropic efficiencies.

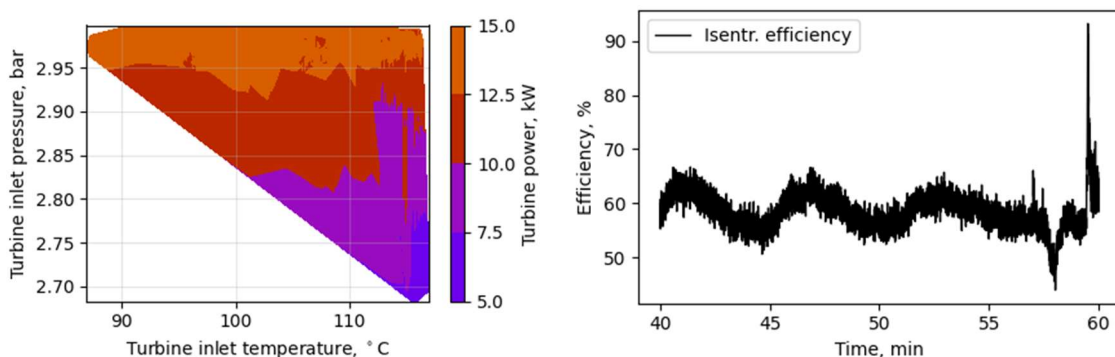


Figure 118. Results from one of the test runs. To the left, the turbine power output as a function of turbine inlet pressure and turbine inlet temperature. To the right, the resulting isentropic efficiency.

T A Č R

Due to technical problems during the testing of the axial turbine for isobutane, the test rig needed a major refurbishment causing a long delay and led to a need for a project change for the originally planned testing of an isobutane RVE.

5 WP5 – Assessment and feasibility mapping

The first result belonging to the feasibility mapping is the cycle design point optimization from WP1, repeated below in Figure 119. With a tailor-made design of the expander, it was shown how the design nominal point of the expander and whole cycle can affect the operational efficiency and thus cumulative power production. In this specific case a potential for 10 % increase in accumulated power production was demonstrated.

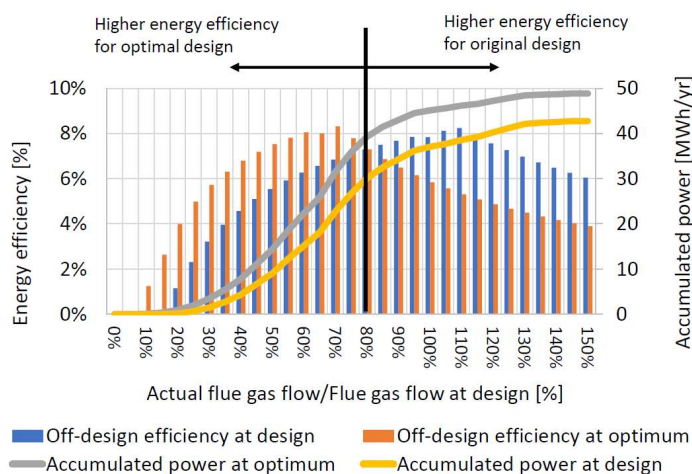


Figure 119. Energy efficiency and accumulated power output for the original and optimized designs based on the reference case study.

As a next phase, feasibility of expanders was looked at in detail using the developed models and experience from our experimental development. These results are shown in Figure 120 and can be taken as indicative results based on the models informed by engineering limits taken from our experimental experience. The efficiency values are indicative and detailed design may shift them by several (typically no more than 2) percentage points, in case of optimization works also into higher efficiency.

Note that for presented expanders there are several groups of boundary conditions and thus corresponding thermodynamic cycles. All MM expander results correspond to the CTU 120 kWth system design. Isobutane turbines are designed around low PR case of 400/160 kPa of the Expand isobutane test rig. RVE for isobutane at these conditions is, however, not feasible, as it would be prohibitively large and operation at higher pressures and slightly higher pressure ratio (1210/350 kPa) is used. Extensive experience from the RVE experimental design suggest unfeasible operation at expander length above 300 mm (largest RVE we built has 245 mm). Together with a L/D parameter maximal value at 2.5, i.e. stator diameter 120 mm, the results for RVE cannot be extended all the way to the 50 kW and entirely different approach to mechanical design would need to be developed for higher power outputs. RVE and Elektra turbine are considered always operating at 3000 rpm.

The RVE results show that there is a cap of efficiency, clearly depending on the pressure ratio (or even more expansion ratio) with higher values and lower pressure ratios, as well as size. Better pressure ratio and densities for the isobutane parameters result in significantly higher peak efficiency and larger

maximal power output. Advantageous for the isobutane RVE efficiency are also relatively smaller leakages per unit of produced power.

However, high-speed turbines, unless we want to exceed extreme speeds, the efficiency drops significantly at small power output systems. The Elektra turbine comes out of our analysis as a possible techno-economic competitor of RVE at power output above about 10 kW. Despite mostly slightly lower efficiency, it enables dry operation and limits a servicing need, which the RVEs have after no more than 10 000 hours.

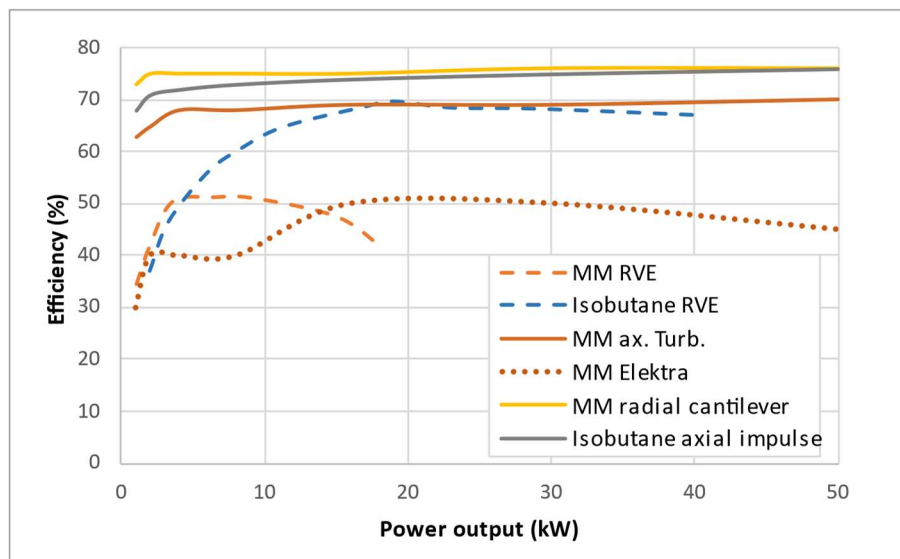


Figure 120. Efficiency mapping for considered expander types (assuming impulse turbines).

Nominal design speed needs to be also considered when selecting the expanders. Figure 121 shows, that while the RVE and Elektra are considered always at constant 3 000 rpm, the other turbines are not only operating at high speed, but a suitable speed differs largely based on the power output.

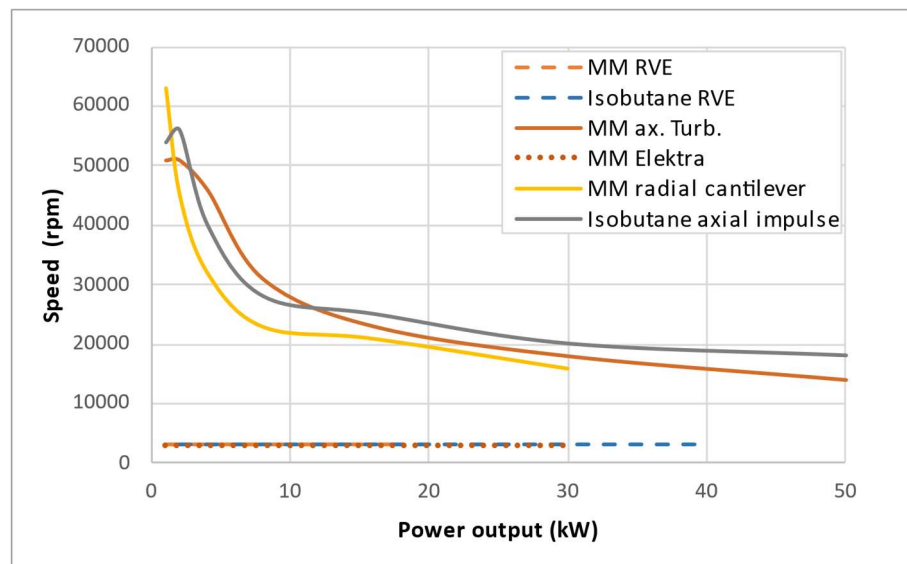


Figure 121. Expander mapping regarding speed for considered expander types.

Highly important are however feasibility maps from the experimental data. An overview of performance at nominal (or maximal if nominal parameters were not achieved) regarding the PR, power output and efficiency is in Figure 122. Note for the further results the low PR and highest power output of the isobutane turbine. This makes the high PR axial turbines performance way more challenging when these two turbines are compared against each other. The axial turbines achieve the highest efficiency, while for the Elektra turbine should be mentioned that this is the first reported ORC trial of this type of turbine and there is a space for improvement, while previous results suggested that it might have the most competitive performance at higher power outputs than used here.

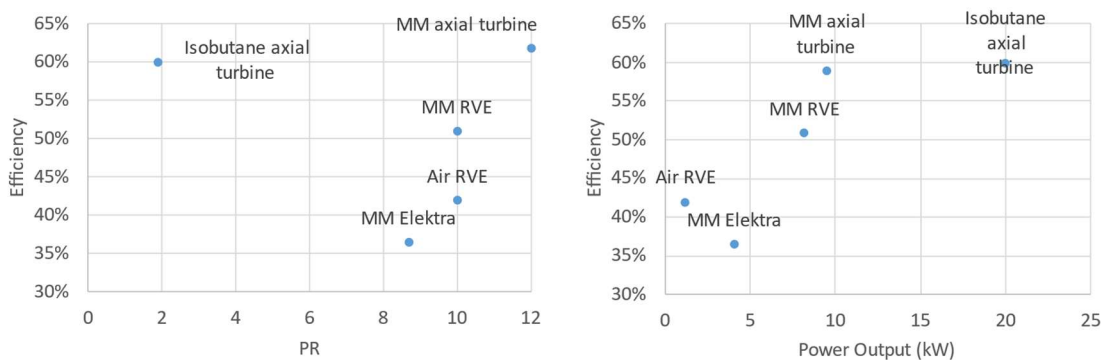


Figure 122. Performance maps of the experimentally explored expanders regarding the PR, power output and efficiency.

Clear disadvantage of the axial turbines is the necessary high speed, documented then in Figure 123. This is particularly represented in achieved performance, where both axial turbines reached only below-nominal speeds. This was 10 000 rpm for the isobutane turbine (nominal 17 – 20 000 rpm) while the MM turbine during the ORC operation did was for safety reasons due to vibrations operated below 20 000 rpm (nominal 28 000 rpm). This prompted a modified design of a 18 000 rpm axial isobutane turbine operating also at higher mass flowrate at slightly lower PR, as shown on the first graph. The document version on the repository will be updated once the experimental performance is obtained.

T A Č R

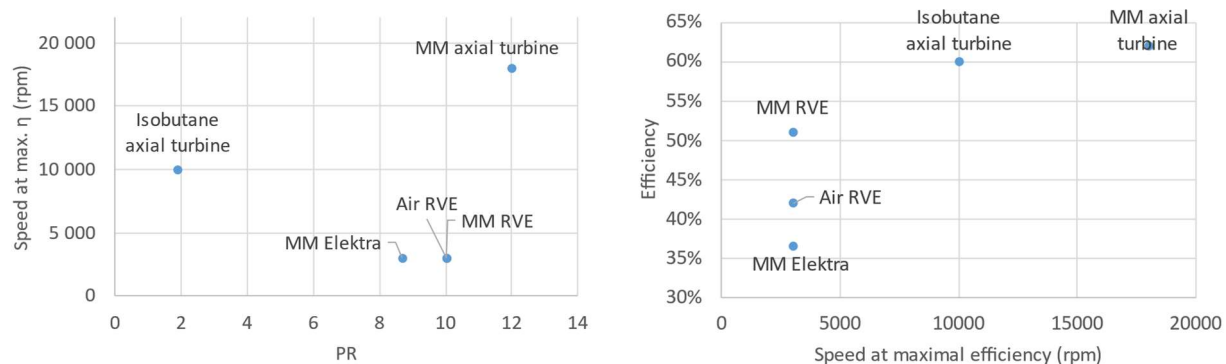


Figure 123. Performance maps of the experimentally explored expanders regarding the PR, nominal speed and efficiency.

In order to complement the technical parameter of speed, Figure 124 shows the rotor diameters of the turbines (eventually stator bore diameter for RVE) for the explored expanders. As expected, diameter must increase, rotational speed decrease with power rating. Furthermore, efficiency increases also with power rating. This effect is most probably underestimated, because the modelling tool does not take into account:

- Reynolds number dependency of friction losses
- Gaps and the corresponding (tip) leakage losses
- Trailing edge thickness and trailing edge losses

All these issues are getting worse if reducing power rating (= smaller turbine). In particular, if partial admission is necessary (1 kW, 2 kW).

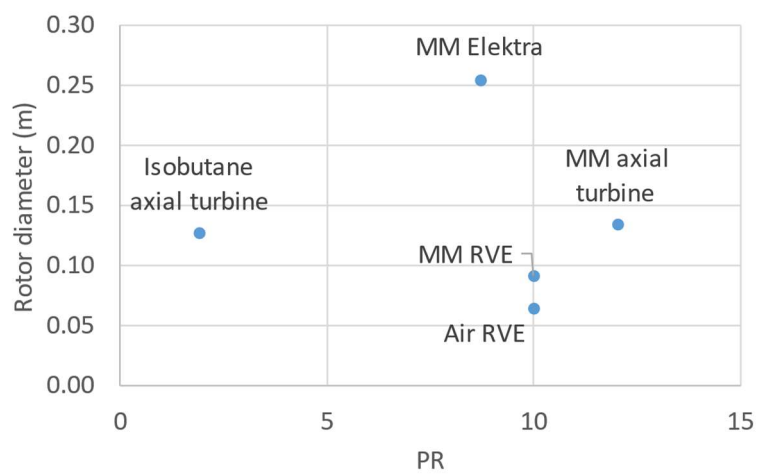


Figure 124. Parameter map of the experimentally explored expanders regarding the PR and rotor (or stator bore for RVE diameter).

As a final result of the mapping are the economic parameters, specifically cost per kW of power output plotted against the efficiency in Figure 125. There are several specific points to take into account. The air RVE has a high cost due to being only 1 kW unit. Yet, isobutane axial turbine with external manufacturing has still higher unit cost even though having the highest power output, reason why the

in-house procured manufacturing and in-house assembly has much lower cost. Lastly, the MM Elektra turbine is somewhat costly as a result of currently limited efficiency and thus low power output.

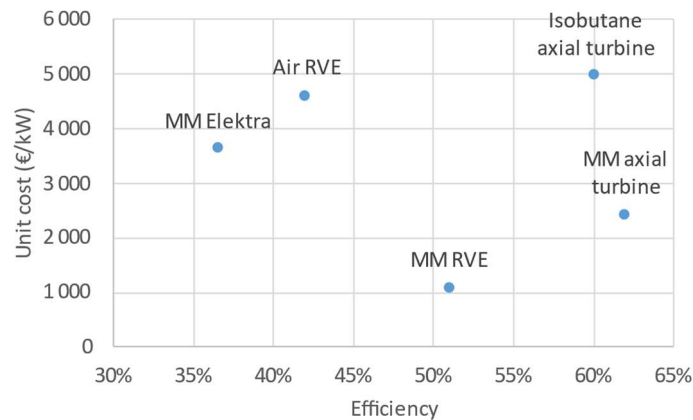


Figure 125. Performance maps of the experimentally explored expanders regarding the PR, nominal speed and efficiency.

For the experimental data for the analysis, please refer to the repository:

<https://github.com/janspale/DEXPAND/blob/main/README.md>

6 Conclusions

Over the course of the project, significant activities were undertaken each year to develop, test, and optimize turboexpanders for Organic Rankine Cycle (ORC) systems, focusing particularly on micro and small-scale applications. This comprehensive conclusion encapsulates the achievements and learnings from each year, aligning with the project's objectives.

The development and optimization of expander models were key achievements, including the creation of a universal off-design optimization tool for ORC cycles enhanced by the Rankine Lab software. This tool was pivotal in assessing the best performance parameters for varying conditions and was tested on a biomass-fired micro-cogeneration system, showing a 10% increase in accumulated power production compared to the base case.

Several expander types, including the novel Elektra turbine and new approach to axial turbines, underwent experimental validation and testing. These tests were conducted on different rigs, such as the MM micro ORC laboratory stands and the EXPAND test rig, providing crucial data for optimizing turbine performance and design. A significant milestone was the transition from the rotary vane expander to the velocity compounded turboexpander, demonstrating higher novelty and exploring less-charted territories.

Manufacturing and design adjustments were also integral to the project. Various designs, including components manufactured using advanced methods like 3D printing, were tested, highlighting the benefits and limitations of different manufacturing techniques. Insights gained from these tests led to significant improvements in design for manufacturability and subsequent system reliability.

The project included detailed feasibility mapping of different expanders, analysing performance, cost, and operational efficiency. This comprehensive mapping provided valuable insights for future applications and developments in small-scale ORC systems. International collaboration and knowledge sharing played a crucial role in the project's success. The partnership between CTU, SINTEF, and NTNU enabled a broader scope of testing and development, leveraging the unique capabilities and facilities of each partner.

The findings and tools developed during the project are made publicly available through open-access publications and repositories, or will be made available in near future with upcoming publications, ensuring that the knowledge gained can benefit the wider scientific and industrial communities. Despite encountering several technical challenges and the need for project adaptations, the project successfully met its outlined objectives. The blend of theoretical modelling, practical experimentation, and collaborative research has culminated in significant advancements in ORC technology.

Future efforts will focus on progressing experimental results, publishing findings, and exploring further optimizations and applications for different working fluids and operating conditions. The project's achievements have paved the way for future innovations and applications in sustainable energy technologies, making notable strides towards more efficient and flexible small-scale ORC systems.

References

- [1] S. L. Dixon and C. Hall, *Fluid mechanics and thermodynamics of turbomachinery*. Butterworth-Heinemann, 2013.
- [2] M. Astolfi and E. Macchi, "Efficiency Correlations for Axial Flow Turbines Working With Non-Conventional Fluids," *Asme Orc 2015*, pp. 1–12, 2015.
- [3] P. Colonna, A. Guardone, and N. R. Nannan, "Siloxanes: A new class of candidate Bethe-Zel'dovich-Thompson fluids," *Phys. Fluids*, vol. 19, no. 8, 2007, doi: 10.1063/1.2759533.
- [4] P. Colonna, N. R. Nannan, A. Guardone, and E. W. Lemmon, "Multiparameter equations of state for selected siloxanes," *Fluid Phase Equilib.*, vol. 244, no. 2, pp. 193–211, 2006, doi: 10.1016/j.fluid.2006.04.015.
- [5] G. Cammi, C. C. Conti, A. Spinelli, and A. Guardone, "Experimental characterization of nozzle flow expansions of siloxane MM for ORC turbines applications," *Energy*, vol. 218, p. 119249, 2021, doi: 10.1016/j.energy.2020.119249.
- [6] A. P. Weiß *et al.*, "Customized ORC micro turbo-expanders - From 1D design to modular construction kit and prospects of additive manufacturing," *Energy*, vol. 209, p. 118407, Jul. 2020, doi: 10.1016/j.energy.2020.118407.
- [7] R. Agromayor and L. O. Nord, "Preliminary Design and Optimization of Axial Turbines Accounting for Diffuser Performance," *Int. J. Turbomachinery, Propuls. Power*, vol. 4, no. 3, p. 32, Sep. 2019, doi: 10.3390/ijtpp4030032.
- [8] J. Hauer, "Analytische Studie zur optimierten Turbinenauslegung," Hochschule Amberg – Weiden, 2011.
- [9] M. Pini *et al.*, "SU2: The Open-Source Software for Non-ideal Compressible Flows," *J. Phys. Conf. Ser.*, vol. 821, no. 1, pp. 1–10, 2017, doi: 10.1088/1742-6596/821/1/012013.
- [10] M. J. Zucrow and Hoffman Joe, "Gas Dynamics Vol. II." p. 491, 1977.
- [11] M. Zocca, A. Uusitalo, T. Turunen-saaresti, and A. Guardone, "METHOD OF CHARACTERISTICS-BASED DESIGN AND NUMERICAL SIMULATION OF A MICRO-ORC SUPERSONIC TURBINE NOZZLE RING," no. 2017, pp. 5–11, 2019.
- [12] N. Anand, P. Colonna, and M. Pini, "Design guidelines for supersonic stators operating with fluids made of complex molecules," *Energy*, vol. 203, p. 117698, 2020, doi: 10.1016/j.energy.2020.117698.
- [13] E. F. C. SOMERSCALES, "The Vertical Curtis Steam Turbine," *Trans. Newcom. Soc.*, vol. 62, no. 1, pp. 157–158, Jan. 1990, doi: 10.1179/TNS.1990.008.
- [14] V. Vodicka, "Rotary vane expander optimization for low-power cycles," 2019. [Online]. Available: <https://dspace.cvut.cz/handle/10467/86998>
- [15] J. Spale, V. Novotny, J. Novotny, A. P. Weiß, and M. Kolovratnik, "Experimental Development of Additively Manufactured Turboexpanders towards an Application in the ORC," 2022.
- [16] E. Lemmon, M. Huber, and M. O. McLinden, "NIST Standard Reference Database 23: Reference Fluid Thermodynamic and Transport Properties-REFPROP." National Institute of Standards and Technology, Gaithersburg, 2010.
- [17] K. Baumann, "Some recent developments in large steam turbine practice," *J. Inst. Electr. Eng., Technologická agentura České republiky*

T A
Č R

vol. 59, no. 302, pp. 565–623, Jun. 1921, doi: 10.1049/JIEE-1.1921.0040.